Methods for quantitative characterization of three-dimensional grain boundary networks in polycrystalline materials

Krzysztof Głowiński

Doctoral dissertation

Cracow 2015

Aleksander Krupkowski
Institute of Metallurgy and Materials Science
Polish Academy of Sciences

Abstract

It is well known that grain boundaries have an impact on properties of polycrystalline materials. The most basic aspect of boundary analysis is boundary geometry. Geometry of a boundary is described by five so-called macroscopic boundary parameters, i.e., by relative orientation between abutting grains and inclination of the boundary plane. Recent progress in development of experimental techniques for three-dimensional orientation mapping (e.g., electron backscatter diffraction combined with precise serial sectioning) has made it possible to determine all five geometric parameters for significant numbers of boundaries. The resulting data sets are sufficiently large for carrying out statistical studies of boundaries. It turns out that boundary characterization with all five boundary parameters taken into account is far more complex compared to that limited solely to grain misorientations. This dissertation is devoted to development of effective tools for geometric characterization of individual boundaries and quantitative analyses of entire boundary networks.

Several types of geometrically characteristic grain boundaries are distinguished. Based on all five parameters, boundaries can be classified, e.g., as tilt, twist, symmetric, or 180°-tilt. Two questions related to this classification are addressed: 1. Does a boundary having given parameters belong – within an assumed tolerance – to any of these groups? 2. What are the area-fractions of characteristic boundaries in a boundary network? To answer them, applicability of various approaches to recognizing the boundary types are considered. E.g., it is shown that the widespread idea of decomposition of a boundary into its tilt and twist components is not suitable for analysis of experimental (error-affected) data. Other solutions are either inefficient or provide incomplete information. Therefore, new reliable and fast-to-calculate parameters describing geometry of boundaries are defined. Then, using these parameters, the frequencies of occurrence of characteristic boundaries are estimated for the first time for real materials (ferritic steel and nickel-based superalloy IN100).

A basic characteristic of a boundary network in a given polycrystal is a distribution of boundaries with respect to their macroscopic parameters. To avoid artifacts caused by the currently used computation method, it is proposed to utilize the kernel density estimation technique and to determine boundary distributions based on distance functions defined in the five-dimensional space of boundary parameters. Based on diverse example distributions obtained for several metals with both face-centered and body-centered structures (pure Ni, the Ni-based alloy, and ferrite), it is shown that with new computational approach, the resulting distributions are clearly more accurate. A scheme of interpretation of the distributions is also proposed. It includes evaluation of their statistical reliability and identification of their symmetries. Besides that, charts allowing for verification whether extrema in such distributions correspond to boundaries of characteristic geometry are obtained using two complementary methods (analytical and numerical). Kernel density estimation is also adapted to computation of boundary-plane distributions independent of misorientations. Such distributions are studied in both crystallite and laboratory reference frames. The distribution functions given in the crystallite frame are used for investigation of populations of boundary planes in pure Ni and alloy IN100. The distribution functions in the laboratory frame have not been considered before; the functions of this kind are computed for the above-mentioned metals as well as for yttria.

In parallel to developing the aforementioned methods themselves, a package of computer programs including implementations of the new approaches has been created. Its features are briefly described.

Streszczenie

Rozwój metod ilościowego opisu trójwymiarowych siatek granic ziaren w materiałach polikrystalicznych

Obecność granic ziaren ma wpływ na szereg właściwości materiałów polikrystalicznych. Najbardziej podstawowym aspektem analizy granic ziaren jest ich geometria. Geometria granicy opisana jest za pomocą pięciu tzw. makroskopowych parametrów granicy, najczęściej jest to różnica orientacji pomiędzy sąsiadującymi ziarnami i nachylenie płaszczyzny granicy. Rozwój technik eksperymentalnych przeznaczonych do trójwymiarowego obrazowania mikrostruktur pozwala na pomiar wszystkich pięciu parametrów dla dużych zestawów granic. Znaczne rozmiary uzyskiwanych zbiorów danych umożliwiają przeprowadzenie pewnych analiz statystycznych. Okazuje się jednak, że analizy biorące pod uwagę pięć parametrów granic są zdecydowanie bardziej skomplikowane niż te uwzględniające tylko różnice orientacji pomiędzy ziarnami. Niniejsza rozprawa doktorska poświęcona jest rozwijaniu wydajnych i wiarygodnych metod do geometrycznego opisu zarówno pojedynczych granic ziaren, jak siatek złożonych z wielu granic.

Wyróżnia się kilka typów granic o charakterystycznej geometrii. W oparciu o pięć makroskopowych parametrów granice mogą być klasyfikowane jako skręcone, nachylone, symetryczne, bądź quasi-symetryczne. Rozważane są dwa zagadnienia powiązane z tą klasyfikacją: 1. Czy granica o danych parametrach należy – ustaliwszy pewną tolerancję – do którejś z tych grup? 2. Jaki jest udział granic charakterystycznych w danej siatce granic? Aby odpowiedzieć na te pytania, zbadano użyteczność różnych metod do rozpoznawania typu granicy. Wykazano, że szeroko znany rozkład granicy na składowe skręconą i nachyloną nie jest odpowiedni do analizy danych eksperymentalnych tj. obarczonych błędem. Pozostałe znane dotychczas rozwiązania są albo mało wydajne albo nie dostarczają pełnej informacji. Dlatego zdefiniowane zostały

nowe efektywne parametry opisujące geometrię granic. Następnie, przy wykorzystaniu tych parametrów, po raz pierwszy oszacowano częstości występowania granic charakterystycznych w materiałach rzeczywistych (w stali ferrytycznej i nadstopie IN100 na bazie niklu).

Podstawową charakterystyką siatki granic ziaren w danym materiale jest rozkład (tj. częstość występowania) granic w dziedzinie makroskopowych parametrów. Aby uniknąć artefaktów pojawiających się w rozkładach wyznaczonych przy użyciu dotychczas stosowanej metody, zaproponowano wykorzystanie jądrowego estymatora gęstości i obliczanie rozkładów w oparciu o funkcje odległości zdefiniowane w pięciowymiarowej przestrzeni granic. W oparciu o przykładowe rozkłady uzyskane dla metali o strukturach regularnych ściennie i przestrzennie centrowanych (czysty nikiel, stop na bazie Ni, ferryt) pokazano, że nowa metoda obliczeniowa prowadzi do uzyskania bardziej precyzyjnych rozkładów granic. Zasugerowany został także schemat interpretacji takich rozkładów. Składają się na niego ocena statystycznej wiarygodności rozkładów oraz identyfikacja ich symetrii. Ponadto, korzystając z dwóch uzupełniających się metod: analitycznej i numerycznej, otrzymane zostały diagramy pozwalające na weryfikację czy ekstrema w rozkładach odpowiadają granicom o charakterystycznej geometrii. Nowa metoda obliczeniowa zaadaptowana została także do wyznaczania rozkładów płaszczyzn granic niezależnie od ich różnicy orientacji. Takie rozkłady rozważane są w układzie odniesienia krystalitu oraz w układzie laboratoryjnym. Funkcje rozkładu dane w układzie krystalitu zastosowano do analizy płaszczyzn granic w czystym niklu i nadstopie IN100. Funkcje wyrażone w układzie laboratoryjnym nie były wcześniej rozważane. Funkcje tego rodzaju otrzymano dla wspomnianych powyżej metali, jak również dla tlenku itru.

Równolegle do opracowania nowych metod, stworzony został program komputerowy zawierający implementacje wszystkich nowych algorytmów. Jego możliwości także zostały opisane w niniejszej pracy.

Statement of originality

To the best of the author's knowledge the following solutions and results have not been considered before and are original work performed by the author under the guidance of his advisor:

- Decomposition of a boundary into its tilt and twist components as a means of identification of near-tilt, near-twist, and mixed boundaries is shown to be unsuitable for analysis of experimental data.
- New reliable and easy-to-calculate parameters describing closeness of geometry of a given boundary to tilt, twist, symmetric, and 180°-tilt configurations are defined.
- The frequencies of occurrence of tilt, twist, symmetric, and 180°-tilt boundaries are computed for real materials.
- Charts indicating the locations of symmetric and 180°-tilt boundaries in the boundary space are obtained.
- An alternative method for computing grain-boundary and boundary-plane distributions utilizing the kernel density estimation technique is developed.
- Distributions of boundary planes are also analyzed in the laboratory reference frame.
- Statistical errors of the obtained grain-boundary distributions are evaluated quantitatively.
- Dedicated software for geometric boundary characterization is developed.

Portions of this dissertation have been published in a series of journal papers: Glowinski (2013, 2014); Glowinski and Morawiec (2012, 2014a,b, 2015); Morawiec and Glowinski (2013).

Contents

Symbols and abbreviations

2D, 3D, 5D	Two-, three-, and five-dimensional.
BCC	Body-centered cubic.
CDF	Cumulative distribution function.
CSL	Coincidence-site lattice.
EBSD	Electron backscatter diffraction.
FCC	Face-centerd cubic.
KDE	Kernel density estimation.
MDF	Misorientation density function.
MRD	Multiples of a random distribution.
PDF	Probability density function.
α	Tilt/twist component parameter.
α_L, α_N, α_S, α_I	Parameters substituting the distances to the nearest tilt, twist, symmetric, and 180°-tilt boundaries (in this order).
δ_m, δ_p, δ	Distances between two boundaries in the misorientation and boundary-plane subspaces, and in the complete boundary space (in this order).
δ_L, δ_N, δ_S, δ_I	Distances to the nearest tilt, twist, symmetric, and 180°-tilt boundaries (in this order).
λ	Angle of the tilt component of a disorientation.
λ_F	Minimal tilt angle (from Fortes decomposition).
ν	Angle of the twist component of a disorientation.
ν_F	Minimal twist angle (from Fortes decomposition).
ω	Misorientation angle.
$\mathbf{m}_1$, $\mathbf{m}_2$	Unit vectors normal to the boundary plane given in the coordinate frames attached to the first and second crystallites, respectively.
$\mathbf{u}$	Misorientation axis (unit vector).
$\mathbf{B}$	4×4 interface matrix representing a boundary.
C_1, C_2	Matrices of symmetry operations applied to the first and second grains.
$\mathbf{C}_1$, $\mathbf{C}_2$	4×4 matrices representing symmetry transformations.
M	Misorientation matrix.
$\omega/[hkl]$	Misorientation by the angle ω about the $[hkl]$ axis.
$(hkl)\|(h'k'l')$	Boundary plane with indices (hkl) in the first crystallite, and $(h'k'l')$ in the second one.
$\Sigma n/(hkl)$	A boundary with the Σn misorientation and (hkl) plane (in the first grain).

Chapter 1

Introduction

Grain boundaries and their importance

Engineering materials frequently occur in the form of polycrystalline solids. Polycrystals are built of many crystal grains having different crystallographic orientations. Such agglomerates of grains contain complex three-dimensional networks of interfaces separating neighboring crystallites. In the case of single-phase materials, these interfaces are referred to as *grain boundaries*[1]. The boundaries are sometimes regarded as defects of crystal lattice. Since these boundaries occur in abundance in polycrystals, they play a key role in governing mechanical and functional properties of the materials. Over the past few decades, a number of phenomena and materials properties were reported to be affected by the presence of grain boundary networks; the list includes: recrystallization (Winning and Raabe, 2008), grain growth (Rabkin, 2005), diffusion (Balluffi, 1982; Chen and Schuh, 2006; Peterson, 1983; Swiatnicki et al., 1986), solute segregation (Bouchet and Priester, 1987; Hofmann and Lejček, 1996; Lejček et al., 1997; Swiatnicki et al., 1995), phase transitions (Desai et al., 2009), precipitation (Ainsley et al., 1979), creep (Lehockey and Palumbo, 1997; Thaveeprungsriporn and Was, 1997), corrosion (Lin et al., 1995; Palumbo and Aust, 1990), mechanical strength (Wyrzykowski and Grabski, 1986), cracking (Kobayashi et al., 2014), electrical conductivity (Guo, 1995; Lamzatouar et al., 2005; Wang et al., 1999; Yamamoto et al., 2005), and superconductivity (Graser et al., 2010; Gurevich and Pashitskii, 1998; Hilgenkamp and Mannhart, 2002; Laval et al., 1994). Although much effort has been put into studies of grain boundaries, the relationships between boundary structures and materials

[1] If phases of adjacent crystallites are distinct, the interfaces are called *interphase boundaries*. That kind of interfaces is, however, out of the scope of this dissertation.

properties are still not fully understood.

Toward grain boundary engineering

Since the influence of grain boundaries on a wide range of properties of polycrystals is evident, Watanabe (1984) came up with the idea of controlling and designing boundary networks in order to achieve desired materials properties (see also Shvindlerman and Gottstein, 2005; Watanabe, 2011). In spite of large gaps in understanding of the structure-property relationships, several attempts to put the 'grain boundary engineering' into practice have been made. For instance, an increase of the content of some 'special' boundaries in the microstructure of materials was considered as a way of enhancing their mechanical properties (Bechtle et al., 2009; Furuhara and Maki, 2005; Kobayashi et al., 2010; Watanabe and Tsurekawa, 1999, 2004), weldability (Kokawa, 2005; Kokawa et al., 2007; Lehockey et al., 1998b), corrosion resistance (Cheung et al., 1994; Krupp et al., 2005; Lehockey et al., 1999, 1998a), and radiation resistance (Han et al., 2013). Various processing techniques were also suggested as a means of conducting the interface engineering, e.g., thermo-mechanical processing (Kumar et al., 2000; Schwartz, 1998), severe plastic deformation (Furukawa et al., 2005), manipulation of solute concentrations (Palumbo and Aust, 1995), application of a magnetic field (Watanabe et al., 1990, 2006), as well as combinations of these techniques (Tsurekawa et al., 2005; Zhang et al., 2005).

Macroscopic boundary parameters

The most fundamental route to analysis of grain boundaries is based on their geometry. Although geometric attributes themselves are insufficient for a complete boundary characterization, they are a prerequisite for more extensive boundary studies, e.g., those including structure of atomic bondings or chemical composition at the boundaries. A full description of boundary geometry encompasses both so-called *macroscopic* (Goux, 1974) and *microscopic boundary parameters* (Sutton and Balluffi, 2007). For centro-symmetric materials[2], the macroscopic degrees of freedom are: a relative orientation (*misorientation*) between abutting grains which is described by three independent parameters, and inclination of the boundary plane which is specified by two parameters.

[2]Description of boundaries in materials without the inversion center is more complicated; however, non-centro-symmetric materials are not the subject of this study.

The microscopic boundary parameters describe the translations between lattices of neighboring crystallites. It is frequently assumed that structures of interfaces relax in a way that minimizes interface energy; see, e.g., Olmsted et al., 2009; Ratanaphan et al., 2015. This implies that microscopic displacements of the crystallites are dependent on macroscopic parameters. Moreover, experimental access to microscopic features of interfaces is difficult and limited to a small scale. Development of experimental techniques for three-dimensional microstructure imaging allowed for determining all five macroscopic parameters for statistically significant numbers of boundaries. The quantitative analyses focused on the macroscopic geometry offer a compromise between advancing in understanding of the boundary structure-materials property relationships and feasibility of such analyses.

Three-dimensional orientation maps

Macroscopic boundary parameters of large numbers of boundaries can be extracted from three-dimensional orientation maps. Such 3D images are routinely acquired using electron backscatter diffraction (EBSD) technique (Schwartz et al., 2009) combined with precise serial sectioning; consecutive layers of a sample are removed via either micromilling using a focused ion beam (Groeber et al., 2006; Zaefferer et al., 2008) or mechanical polishing (Saylor et al., 2003a; Uchic et al., 2012a,b) or femtosecond laser ablation (Echlin et al., 2012). Less spread is high-energy X-ray tomography, i.e., a non-destructive technique utilizing synchrotron radiation (Hefferan et al., 2009; Jensen and Poulsen, 2012; Lienert et al., 2011; Poulsen, 2012). Besides 3D-EBSD systems and synchrotron facilities, other techniques with a potential of collecting relatively big amounts of grain boundary data are being tested. These include, e.g., 3D grain-orientation mapping in a transmission electron microscope outfitted with tomographic sample holders (Liu et al., 2011) which was designed for obtaining 3D orientation maps of microstructures composed of nano-sized grains. There are also X-ray tomographs that use laboratory radiation sources instead of synchrotron beam lines (King et al., 2013). Furthermore, the 'atom probe crystallography' technique (Gault et al., 2012) allows for extracting crystallographic information from atom probe data sets, and therefore, provides macroscopic boundary parameters together with atom concentrations at boundaries.

Motivation for this work

Understanding the relationships between boundary structures and materials properties is central for 'intelligent' grain boundary engineering, and thus, for modern materials design. Until recently, most of the works concerning manipulation of boundary networks were focused on the content of boundaries with special misorientations while boundary planes were ignored. Future, however, lies in tailoring of all five macroscopic parameters simultaneously (Davies and Randle, 2001). Novel experimental techniques open new opportunities for extending our knowledge in this area: some statistical analyses of boundaries based on all macroscopic boundary parameters are now possible. For instance, it is interesting to trace the evolution of boundary networks during processing of materials (Kim et al., 2005; Randle et al., 2008). Since quantitative boundary characterization with five parameters taken into account turns out to be complex compared to that limited solely to grain orientations, reliable and efficient analytic tools are needed. Moreover, the sizes of experimentally obtained boundary data sets are large, and in order to process these data in an efficient and automated way, dedicated software is needed. Finally, despite considerable progress in development of experimental apparatus made over the last years, acquisition of large 3D data sets of good quality is still cumbersome. To take full advantage of the collected data, it is important to analyze them in a way that does not distort final conclusions.

Chapter 2

State of the field

This chapter consists of a survey of the methods for grain boundary characterization which have been proposed in earlier works. It begins with an introduction to mathematical formalism necessary for quantitative description of individual boundaries and networks composed of many boundaries. The further sections concern, i.a., boundaries of special geometries, approaches to verification whether a boundary is geometrically special, distributions of grain boundaries and their symmetries, theoretical models connecting boundary geometry with boundary energy, and existing software related to studies of boundaries. At the end of the chapter, issues related to these solutions are pointed out.

2.1 Mathematical foundations

2.1.1 Space of grain boundaries

Geometry of grain boundaries is described by five numbers. Such 5-tuples of macroscopic boundary parameters constitute the *grain boundary space*. With the restriction to centro-symmetric materials, the misorientation between abutting grains is represented by a proper rotation. There is a one-to-one correspondence between proper rotations and 3×3 special orthogonal matrices, and multiplication of these matrices corresponds to composition of rotations (see, e.g., Morawiec, 2004). Hence, misorientations can be recognized as elements of $SO(3)$, i.e., the group of special orthogonal matrices of the dimension 3×3. Local parameters of a boundary plane can be represented by a unit vector normal (at a given point) to that boundary. Endpoints of all such vectors constitute the sphere $\mathcal{S}^2$. Thus, the space of grain boundaries can be mapped onto a Cartesian product $(SO(3) \setminus \{\mathbf{I}\}) \times \mathcal{S}^2$; the identity matrix $\mathbf{I}$ corresponding

to the 'no-misorientation' case must be excluded if single-phase boundaries are considered[3].

2.1.2 Equivalent boundary representations

Five macroscopic parameters of a planar boundary can be conveniently wrapped in a 4×4 interface matrix (Morawiec, 1998)

$$\mathbf{B} = \begin{bmatrix} 0 & \mathbf{m}_2^T \\ \mathbf{m}_1 & M \end{bmatrix}, \tag{2.1}$$

where M is a matrix representing the misorientation between adjacent grains, and $\mathbf{m}_1$ ($\mathbf{m}_2$) is the outward unit vector normal to the boundary plane expressed in the Cartesian reference frame attached to the first (second) crystallite. Moreover, the condition $\mathbf{m}_2 = -M^T\mathbf{m}_1$ is satisfied. Because of crystal symmetry, a given physical boundary may have many equivalent representations. In other words, a given boundary may be represented by multiple points in the boundary space. To extract complete information about a given physical boundary, all its symmetrically equivalent representations must be analyzed. The equivalent representations can be easily obtained using interface matrices: the representation $\mathbf{B}$ given by Eq.(2.1) is equivalent to $\mathbf{B}^-$ and $\mathbf{C}_1\mathbf{B}\mathbf{C}_2^T$, where

$$\mathbf{B}^- = \begin{bmatrix} 0 & -\mathbf{m}_2^T \\ -\mathbf{m}_1 & M \end{bmatrix}, \quad \mathbf{C}_i = \begin{bmatrix} 1 & 0 \\ 0 & C_i \end{bmatrix}, \tag{2.2}$$

and C_i ($i = 1, 2$) are proper orthogonal matrices of symmetry operations of the crystal. Additionally, in the case of single-phase interfaces, if an interchange of grains is allowed, the representation $\mathbf{B}$ is equivalent to $\mathbf{B}^T$. That is our case as in statistical studies of polycrystalline microstructures, adjacent crystallites are indistinguishable, i.e., the boundary between 'right' and 'left' grains is the same as that between 'left' and 'right' grains[4].

Interface-plane scheme

Throughout this dissertation boundaries are described in terms of their misorientations and boundary normals. For completeness, it is worth mentioning that there exists an alternative parameterization of the boundary geometry

[3] An interface of zero-misorientation could exist only between crystallites of different phases.

[4] The situation is different in the case of investigations of bi-crystals where these two boundaries are treated as distinct.

by a 'twist angle' and two vectors normal to the boundary (one given in the first grain and one expressed in the second crystallite); see Wolf and Lutsko, 1989. However, in this 'interface-plane scheme', boundaries are not described uniquely (Morawiec, 2012a). Furthermore, within this scheme, analysis of crystallographically equivalent boundary representations is less intuitive compared to that based on M and $\mathbf{m}_1$.

2.1.3 Metrics in the boundary space

Distance functions defined in the boundary space facilitate comparing of geometries of two boundaries. With an appropriate metric, the boundaries are close if their geometries are similar, otherwise they are distant. As was mentioned above, the boundary space is a Cartesian product of misorientation and boundary-plane subspaces. Depending on the problem considered, the distances can be defined in the complete product space or separately in each subspace. The distance between two boundary representations $\mathbf{B}$ and $\mathbf{B}'$ (with misorientations M and M' and boundary normals $\mathbf{m}_1$ and $\mathbf{m}'_1$, respectively) is defined in the misorientation subspace as $\beta = \arccos\{[\mathrm{tr}(M'M^T) - 1]/2\}$ and in the boundary-plane subspace as $\eta = [(\zeta_1^2 + \zeta_2^2)/2]^{1/2}$, where $\zeta_i = \arccos(\mathbf{m}_i \cdot \mathbf{m}'_i)$. The distances between two physical boundaries are minimized over all representations equivalent to both $\mathbf{B}$ and $\mathbf{B}'$: $\delta_m = \min\beta$ and $\delta_p = \min\eta$. In the product space, the distance is given as $\delta = \min(\beta^2 + \eta^2)^{1/2}$. The distance can also be given by $\min(\|\mathbf{B} - \mathbf{B}'\|/2)$, where $\|.\|$ denotes the Frobenius norm. For small distances, this norm converges to δ. These distance functions were proposed by Morawiec (1998, 2009a) and they will be used throughout this work. Also, the model of uniformity resulting from these metrics will be used for generating random boundaries. A reader interested in alternative metrics is referred to papers of Cahn and Taylor (2006) and Olmsted (2009).

2.2 Boundaries of characteristic geometry

Exploration of the extensive 5D boundary space can be facilitated by devising adequate boundary classifications, and by indicating reference points in that space. By the nature of the space, the reference points are boundaries of special geometry. Based on misorientation parameters, grain boundaries can be divided into *small-* and *large-angle* boundaries and into *coincidence site lattice* (CSL) boundaries corresponding to subsequent Σ-values and non-CSL bound-

aries (Kronberg and Wilson, 1947). If the grain misorientation is described as a rotation by an angle ω about an axis $\mathbf{u}$, then by small- and large-angle boundaries we understand those with ω less and greater, respectively, than a transition angle which is typically assumed to be 15°. A boundary is referred to as a CSL boundary when lattices of adjacent crystallites have common sites; the Σ-value is an inverse of the fraction of the common sites[5]. What is of our particular interest, boundaries can also be classified based on all five macroscopic degrees of freedom. For instance, tilt, twist, symmetric, properly and improperly quasi-symmetric boundaries are distinguishable. A boundary is a *twist* boundary if its plane is perpendicular to the misorientation axis ($\mathbf{u}\cdot\mathbf{m}_1 = 1$), while a *tilt* boundary has the axis in its plane ($\mathbf{u}\cdot\mathbf{m}_1 = 0$). Since there is some confusion with the notions of symmetric and quasi-symmetric boundaries (Morawiec, 2012a), they need to be described in more detail. We adhere to the established definition of a *symmetric* boundary: its plane is a mirror between crystal structures separated by the boundary. A boundary is called *quasi-symmetric* if the Miller indices of its plane given in the first and the second crystallites belong to the same family. More precisely, a boundary is *properly* (*improperly*) *quasi-symmetric* if it has a representation given by Eq.(2.1) with the vectors $\mathbf{m}_1$ and $\mathbf{m}_2$ related via $\mathbf{m}_1 = -C_2\mathbf{m}_2$ ($\mathbf{m}_1 = +C_2\mathbf{m}_2$). There are a number of relationships between various boundary types. With the inversion symmetry, every symmetric boundary is a tilt boundary. A properly quasi-symmetric boundary is also a twist boundary, and vice versa, a twist boundary is properly quasi-symmetric. In the same sense, improperly quasi-symmetric boundaries are equivalent to 180°-tilt boundaries, and symmetric boundaries are equivalent to 180°-twist boundaries. Proofs of these statements were given by Morawiec (2012a).

Now, the question arises how to verify whether a given boundary can be classified as being of a characteristic type. To discriminate small-angle boundaries from large-angle boundaries, only one number, the disorientation angle, is needed. To qualify a given boundary to CSL – or more precisely, to near-CSL – boundaries corresponding to particular Σ-value, the distance in the misorientation space, δ_m, from the misorientation of that boundary to a certain CSL misorientation is calculated. If this distance is below an assumed threshold, the boundary is classified as a near-CSL boundary. Most commonly these thresholds are given by Brandon (1966) criterion or its variants (Déchamps et al.,

[5]The list of misorientations corresponding to CSL boundaries with $3 \leq \Sigma \leq 31$ and $\Sigma = 39a$ can be found in Appx. B.

1987; Ishida and Mclean, 1973; Palumbo et al., 1998) as ω_0/Σ^p; in the standard Brandon criterion, $\omega_0 = 15^\circ$ and $p = 1/2$. For recognizing near-tilt and near-twist characters of boundaries, several sets of parameters were introduced so far; they are described in what follows.

2.2.1 Decomposition into tilt and twist components

Any misorientation by the angle ω about the axis $\mathbf{u}$ can be decomposed into two sequential rotations: a twist by the angle ν about the axis $\mathbf{m}_1$ (perpendicular to the boundary) followed by a tilt by the angle λ about an axis $\mathbf{l}$ perpendicular to $\mathbf{m}_1$ (Fortes, 1973; Lange, 1967). Similarly to $\mathbf{m}_1$, $\mathbf{u}$ and $\mathbf{l}$ are unit vectors given in the reference frame of the first crystallite. After Fortes (1973), the *twist angle* ν and the *tilt angle* λ are given by the formulas:

$$\tan\frac{\nu}{2} = \left|\mathbf{u}\cdot\mathbf{m}_1 \tan\frac{\omega}{2}\right| \qquad \text{and} \qquad \cos\frac{\nu}{2}\cos\frac{\lambda}{2} = \cos\frac{\omega}{2}. \tag{2.3}$$

From these equations, it follows that for a pure-twist boundary ($\mathbf{u}\cdot\mathbf{m}_1 = 1$), $\nu = \omega$ and $\lambda = 0$, whereas for a pure-tilt boundary ($\mathbf{u}\cdot\mathbf{m}_1 = 0$), $\nu = 0$ and $\lambda = \omega$. If $\nu \neq 0$ and $\lambda \neq 0$, the boundary is referred to as *mixed*. Eqs.(2.3) are singular when $\omega = 180^\circ$. In that case, the solution is as follows: if $\mathbf{u}\cdot\mathbf{m}_1 \neq 0$, then $\nu = 180^\circ$ and $\cos\frac{\lambda}{2} = \mathbf{u}\cdot\mathbf{m}_1$; otherwise, if $\mathbf{u}\cdot\mathbf{m}_1 = 0$, then $\nu = 0$ (the boundary is a pure tilt) and $\lambda = 180^\circ$.

Provided that in the decomposition, the twist is followed by the tilt (not inversely), $\mathbf{l}$ is determined by the conditions:

$$\mathbf{l}\cdot\mathbf{u} = \tan\frac{\lambda}{2}\cot\frac{\omega}{2}, \tag{2.4}$$

$\mathbf{l}\cdot\mathbf{m}_1 = 0$, and $\mathbf{l}\cdot\mathbf{l} = 1$.

Because of crystal symmetry, the angles ν and λ are not unique for a given physical boundary. To get rid of this ambiguity, Lange (1967) inclined toward decomposing boundary representations with *dis*orientations, i.e., those with misorientations having the smallest misorientation angles[6]. For illustration, the twist angle ν and the tilt angle λ for the $\Sigma 7$ disorientation (for the case of cubic O_h crystal symmetry) and varying $\mathbf{m}_1$ are plotted in Figs. 2.1a and b, respectively.

Fortes (1973) considered crystal symmetries in more detail and suggested to calculate ν and λ for all equivalent boundary representations and to take

[6] At times, it is also required that the axis of disorientation lies in the standard stereographic triangle.

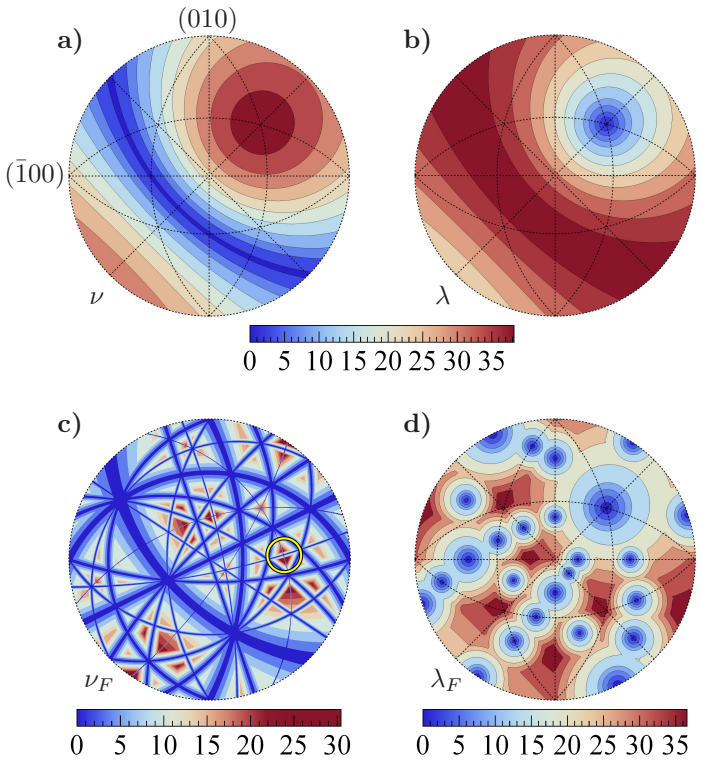

Figure 2.1: *(a)* and *(b)* represent disorientation-based twist (ν) and tilt (λ) angles, respectively, for the $\Sigma 7$ disorientation (for the cubic O_h crystal symmetry) as functions of boundary plane normals. The minimum twist (ν_F) and minimum tilt (λ_F) angles from Fortes decomposition are shown in *(c)* and *(d)*, respectively. Contours are given in degrees and plotted in stereographic projection.

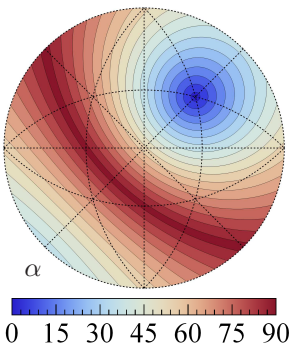

Figure 2.2: 'Tilt/twist component' parameter α as a function of boundary plane normals for the $\Sigma 7$ disorientation (for the cubic O_h symmetry) displayed in stereographic projection. The units are degrees.

minimum values $\nu_F = \min(\nu)$ and $\lambda_F = \min(\lambda)$ as a final result of the decomposition. He considered boundaries given by $\mathbf{BC}_2^T$. Morawiec and Glowinski (2013) showed that it is enough to consider such a set of boundary representations, because other representatives give congruent results. Fortes (1973) also noticed that the tilt and twist angles will be the same even if the order of tilt and twist component rotations is reversed, though the axis $\mathbf{l}$ will be different. Generally, ν_F and λ_F may correspond to different representations of the boundary. If the twist angle ν_F (tilt angle λ_F) is close to zero, we say that the boundary is a near-tilt (near-twist) boundary. The minimum twist and tilt angles are presented in Figs. 2.1c and d, respectively; again as functions of $\mathbf{m}_1$ for the $\Sigma 7$ misorientation. It can be seen that the figures obtained with all boundary representations taken into account are strikingly different compared to those obtained based on representations with the smallest-angle misorientations.

2.2.2 Tilt/twist component parameter

Another approach to quantification of twist and tilt contributions is linked directly to the equations defining tilt and twist boundaries (i.e., $\mathbf{m}_1 \cdot \mathbf{u} = 0$ and $\mathbf{m}_1 \cdot \mathbf{u} = 1$, respectively). Concretely, the contribution of the twist and tilt components is measured by the parameter $|\mathbf{m}_1 \cdot \mathbf{u}|$ (see Seidman, 1992). Equivalently, besides $|\mathbf{m}_1 \cdot \mathbf{u}|$, the angle α between directions of $\mathbf{m}_1$ and $\mathbf{u}$ is used (Rowenhorst and Voorhees, 2005). Amouyal et al. (2005) refer to the parameter $|\mathbf{m}_1 \cdot \mathbf{u}|$ as 'tilt/twist component parameter' (TTC), and this designation will be used here also to α. Seidman (1992), Krakauer and Seidman (1998), Amouyal et al. (2005), and Rowenhorst and Voorhees (2005) used vectors $\mathbf{u}$ and $\mathbf{m}_1$ corresponding to a disorientation. This leads to unique $|\mathbf{m}_1 \cdot \mathbf{u}|$ and α. TTC parameter for boundaries with the $\Sigma 7$ disorientation is presented in Fig. 2.2.

2.2.3 Distances to the nearest tilt and twist boundaries

The next approach was proposed by Morawiec (2009b). The deviation of a boundary from the nearest pure-twist and pure-tilt boundaries can be quantitatively described using a distance in the grain boundary space. A given boundary is classified as near-tilt (near-twist) if it is sufficiently close (in terms of a metric defined in the space) to a pure-tilt (pure-twist) boundary. As described by Morawiec (2009b), the distances to the nearest pure-tilt and pure-twist boundaries can be calculated via numerical minimization.

	O_h			D_{6h}		
Tolerance	Tilt	Twist	T+T	Tilt	Twist	T+T
1°	39.0%	0.4%	0.2%	21.2%	0.2%	0.1%
3°	84.0%	3.9%	3.5%	54.4%	2.0%	1.4%
5°	98.6%	10.6%	10.5%	77.0%	5.4%	4.8%

Table 2.1: Fractions of near-tilt and near-twist boundaries among random grain boundaries for the cubic O_h and hexagonal D_{6h} symmetries for various tolerance thresholds. 'T+T' stands for boundaries which are simultaneously near-tilt and near-twist. The percentages are cited after Morawiec (2009b, 2011).

This procedure has also been used for obtaining diagrams with locations of all pure-tilt and pure-twist boundaries for low-Σ misorientations in the case of the O_h symmetry (Morawiec, 2011). Example diagrams for the $\Sigma 7$ misorientation are reproduced in Fig. 2.3. The distances from a given boundary to the nearest pure-twist and the nearest pure-tilt boundaries are denoted by δ_N and δ_L, respectively. In particular, $\delta_N = 0°$ for pure twists, and $\delta_L = 0°$ for pure-tilt boundaries.

2.2.4 Fractions of tilt and twist boundaries

Being able to determine whether a boundary is of a characteristic type allows for estimation of the fractions of boundaries of that type in a studied microstructure. The frequencies of occurrence of near-tilt and near-twist boundaries among random grain boundaries for the cases of cubic O_h and hexagonal D_{6h} symmetries were given by Morawiec (2009b, 2010); they were calculated based on the distances δ_N and δ_L. The percentages were computed for the tolerance thresholds of 1, 2, 3, 4, and 5°; cf. Tab. 2.1. Probability distribution functions (PDFs) for the distances δ_N and δ_L may serve (similarly to Mackenzie (1958) plots showing the distributions of disorientation angles) as characteristics of a given boundary network. PDFs for δ_N and δ_L for the O_h symmetry will be reproduced in Fig. 5.4. The fractions of tilt and twist boundaries for arbitrary tolerance thresholds (Tab. 2.1) can be obtained by integrating the PDFs, or can be directly read from the corresponding cumulative distribution functions (CDFs) (Morawiec, 2009b, 2010).

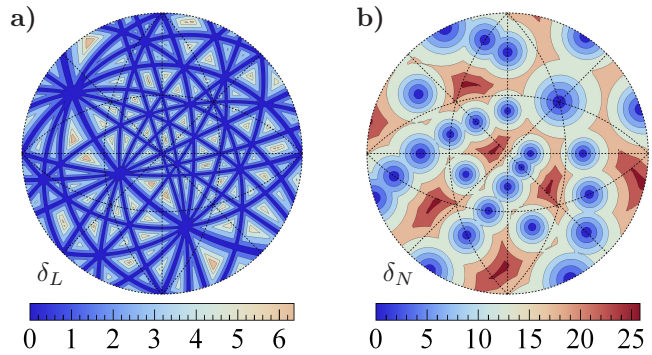

Figure 2.3: Distributions of the distances δ_L to the nearest tilt *(a)* and δ_N to the nearest twist *(b)* boundaries as functions of boundary planes for the Σ7 misorientation for the cubic O_h symmetry. Contours are given in degrees and plotted in stereographic projection.

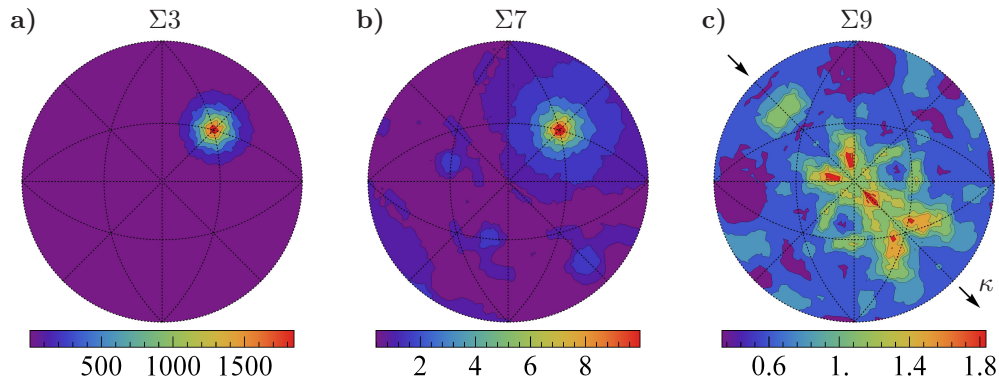

Figure 2.4: Sections through the distribution of grain boundaries for the Σ3 *(a)*, Σ7 *(b)*, and Σ9 *(c)* misorientations computed using the partition-based method with 10°-bins for data collected from Ni-base superalloy IN100. The sections are drawn in stereographic projection. Populations are given in multiples of random distributions. To be compared to Figs. 7 and 10 presented by Rohrer et al. (2010).

2.3 Grain boundary distributions

Distributions of populations of boundaries as functions of the five macroscopic parameters are the primary characteristics of 3D boundary networks. Such functions are usually presented in the form of 2D sections for fixed misorientations and varying boundary planes, and these sections are plotted in stereographic projections. The populations are conventionally expressed in multiples of random distributions (MRD). With these units, it is easy to indicate geometric configurations occurring more and less frequently compared to the isotropic case, i.e., those for which corresponding distribution values are, respectively, greater and less than unity.

2.3.1 Partition-based method

In all relevant reports published so far (e.g., Beladi and Rohrer, 2013b; Kim et al., 2008; Li et al., 2009; Rohrer et al., 2010; Saylor et al., 2003a), the grain boundary distributions have been computed using a method (Saylor et al., 2003a) based on partition of a certain domain in the boundary parameter space into equivolume bins and on counting boundaries falling into the bins. For brevity, technicalities of this method are described for the case of cubic O_h symmetry only; however, the method can be easily extended to other symmetries. For the purpose of the partition, grain misorientations and boundary plane normals are parameterized by Euler angles φ_1, Φ, φ_2 and spherical (polar and azimuth) angles ϑ and ψ, respectively. With cubic crystal symmetry, the used parameter domain is restricted by $0^\circ \leq \varphi_1, \Phi, \varphi_2, \vartheta \leq 90^\circ$ and $0^\circ \leq \psi \leq 360^\circ$[7]. The 'rectangular' box $\varphi_1 \times \cos\Phi \times \varphi_2 \times \cos\vartheta \times \psi$ is partitioned into equivolume rectangular bins of dimensions $\Delta\varphi_1 = \Delta\varphi_2 = 90^\circ/k$, $\Delta\psi = 90^\circ/k'$, $\Delta(\cos\Phi) = 1/k$ and $\Delta(\cos\vartheta) = 1/k'$, where k, k' are positive integers. Typically, "10°-bins" ($k = 9 = k'$) are used. In the process of boundary distribution determination, boundary networks are reconstructed in the form of meshes (see Chap. 4). To compute the distribution, areas of mesh segments are accumulated in the bins. With the domain used in the partition-based approach, a boundary (of multiplicity 1; see Sec. 2.3.5) is represented by 36 (different) symmetrically equivalent points.[8] Therefore, at the accumulation

[7] The domain is chosen so that it consists of complete (and does not contain fractional) fundamental zones. This domain may be different if non-cubic crystal symmetries are considered.

[8] This number varies depending on the used domain and considered crystal symmetry.

step, each segment contributes to multiple bins, and in the end, the value of the grain boundary distribution at a given point is obtained by averaging over the bins containing equivalent points.

As an illustration of this method, sections through the boundary distribution computed for nickel-base superalloy IN100 (i.e., for Small IN100 data set; see Appx. A) for the $\Sigma 3$, $\Sigma 7$, and $\Sigma 9$ misorientations are shown in Fig. 2.4. These sections are consistent with those obtained by Rohrer et al. (2010) for the same material; this is an important cross-check as Rohrer et al. (2010) used different software for reconstruction of boundaries than that which are used in this work (see Chap. 4).

2.3.2 Boundary-plane distributions

The five-parameter grain boundary distributions are frequently accompanied by simplified distributions showing the frequencies of occurrence of boundary planes averaged over all misorientations. In essence, these distributions are functions of only two macroscopic parameters. Analogously to the all-parameter distributions, boundary-plane distributions are given in MRDs and are displayed in stereographic projections. However, for this kind of distribution functions, it is enough to present the standard stereographic triangle instead of the whole hemisphere.

From the technical side, the first stages of procedure for obtaining distributions of boundary planes are the same as those in the case of the five-parameter distributions. A chosen domain of the boundary space is partitioned into $(4\,k'^2) \times (k^3)$ bins (assuming the standard domain for cubic symmetry); the first and second factors correspond to the numbers of bins in the boundary-plane and misorientation subspaces, respectively. Then, areas of mesh segments constituting reconstructed boundaries are initially accumulated in those bins. To calculate the misorientation-averaged boundary-plane distribution we need $4\,k'^2$ bins. The value in each of these bins is an average over the areas initially accumulated in the corresponding k^3 bins. The last step, i.e., averaging of the distribution value at a given plane over bins containing equivalent planes is conceptually the same as in the case of 5D distributions. The algorithm described here is commonly used, although boundary-plane distributions could also be obtained directly based only on parameters of boundary planes, and the averaging over misorientations would not be needed. An instance of a boundary-plane distribution obtained for yttria (Yttria data set) is presented in Fig. 2.5.

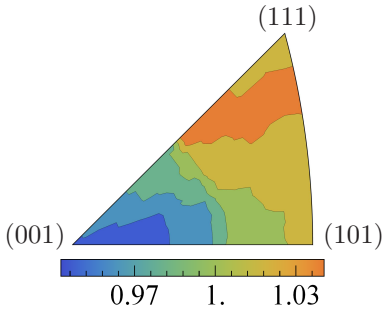

Figure 2.5: Distribution of boundary planes (averaged over misorientations) obtained for yttria using the partition-based method. Contours are given in multiples of the random distribution and are displayed in the standard stereographic triangle.

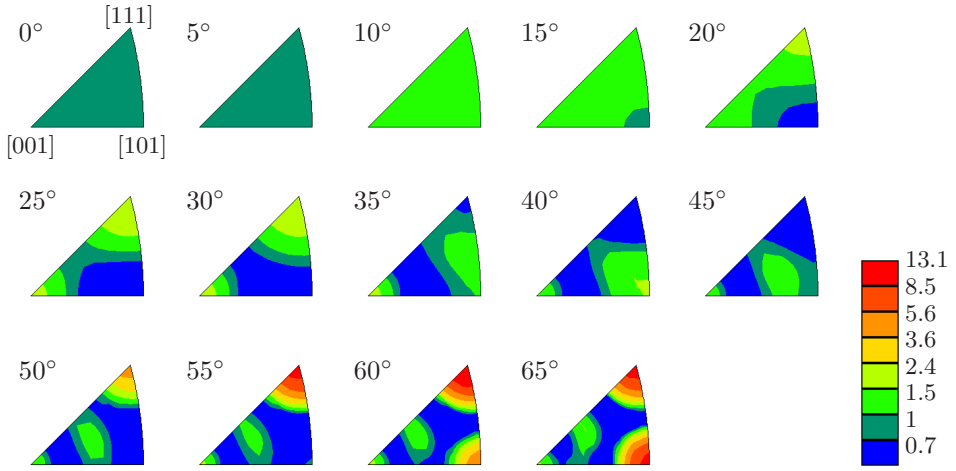

Figure 2.6: Misorientation distribution function computed for Ni-based superalloy IN100 using expansion into a series of generalized spherical harmonics implemented in *OIM Analysis* software. The distribution is given as functions of misorientation axes for fixed misorientation angles. The units are multiples of a random distribution.

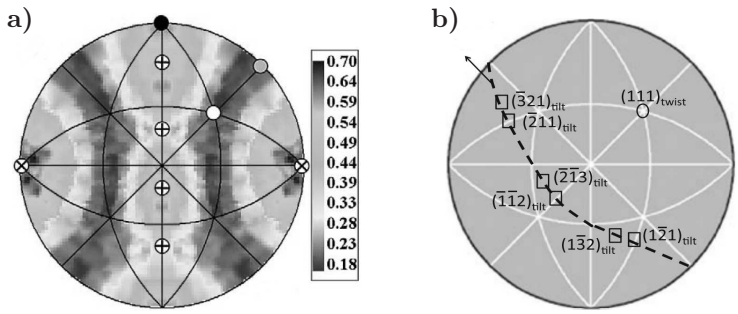

Figure 2.7: *(a)* The section for the 35°/[100] misorientation through the boundary distribution obtained for magnesia; reprinted from Saylor et al. (2003a), with permission from Elsevier. Contours (plotted in stereographic projection) are given in multiples of the random distribution. Locations of twist and symmetric boundaries are marked with ⊗ and ⊕, respectively. *(b)* Positions of the tilt boundaries (the dashed line) and the pure twist boundary (the circle) in the sections for misorientations about the [111] axis; reprinted from Beladi and Rohrer (2013a), with permission from Springer.

2.3.3 Misorientation distribution functions

A misorientation distribution function (MDF) is another type of a distribution in a subdomain of macroscopic boundary parameters (see, e.g., Bunge, 1982; Kallend et al., 1976; Pospiech et al., 1986). This function represents the frequencies of occurrence of boundaries with particular misorientations ignoring boundary inclinations. Since MDFs can be obtained, e.g., from routinely collected 2D EBSD maps, such distributions are frequently used for quantitative studies of microstructures; an example of MDF is plotted in Fig. 2.6.

2.3.4 Locations of characteristic boundaries

One of the most basic steps in interpretation of the obtained grain boundary distributions is to check whether maxima, as well as minima, of these distributions correspond to boundaries of characteristic geometric features. To check this, it is essential to know which points in the boundary space coincide with tilt, twist, symmetric, etc. boundaries. For instance, let us have a look at the distribution of boundaries obtained by Saylor et al. (2003a) for magnesia; in the section for the 35°/[100] misorientation (Fig. 2.7a), the poles (100) and $(\bar{1}00)$ were marked as locations of pure-twist boundaries. These positions of twists follow directly from the type-defining condition. However, Morawiec (2011) has shown that without considering crystal symmetry, many twist

boundaries are overlooked. Despite this, the simplistic approach is still used, e.g., by Beladi and Rohrer (2013a); see Fig. 2.7b. As was already mentioned, Morawiec (2011) presented distributions of the distances δ_L and δ_N to the nearest tilt and twist boundaries, respectively, for low-Σ misorientations (for cubic O_h crystal symmetry) similar to those in Fig. 2.3. These distributions indeed reveal many more pure-twist boundaries (i.e., points where $\delta_N = 0$). The same considerations apply to tilt boundaries; in Fig. 2.7b, there is only one zone of tilt boundaries, while in Fig. 2.3a one can see a web of intersecting tilt zones (i.e., zones with $\delta_L = 0$).

2.3.5 Symmetries of functions of macroscopic boundary parameters

The frequencies of occurrence of interfaces of specific misorientations and interface normals are an example of functions of five macroscopic boundary parameters. Since each geometric arrangement at the interface is described by many equivalent 5-tuples of the macroscopic parameters, any function f of the macroscopic parameters must take equal values at these equivalent points (Morawiec, 1998, 2009a), i.e., $f(\mathbf{B}) = f(\mathbf{B}')$, where $\mathbf{B}$ and $\mathbf{B}'$ are equivalent representations of the same physical boundary. In particular, some 2D sections for fixed misorientation M exhibit symmetries. Assuming that $\mathbf{B}$ is given by Eq.(2.1) and

$$\mathbf{B}' = \begin{bmatrix} 0 & (C_2\mathbf{m}_2)^T \\ C_1\mathbf{m}_1 & C_1MC_2^T \end{bmatrix}. \tag{2.5}$$

To have a symmetric section for M, we need $C_1MC_2^T = M$. The normal $\mathbf{m}_1'$ equivalent to $\mathbf{m}_1$ is given as $\mathbf{m}_1' = C_1\mathbf{m}_1$. If grain-exchange symmetry is allowed, $\mathbf{B}'$ can also be given as

$$\mathbf{C}_1\mathbf{B}^T\mathbf{C}_2^T = \begin{bmatrix} 0 & (C_2\mathbf{m}_1)^T \\ -C_1M^T\mathbf{m}_1 & C_1M^TC_2^T \end{bmatrix}. \tag{2.6}$$

To have a symmetric section for M in this case, we need $C_1M^TC_2^T = M$. The normal $\mathbf{m}_1'$ equivalent to $\mathbf{m}_1$ can be expressed as

$$\mathbf{m}_1' = -C_1M^T\mathbf{m}_1 = -MC_2\mathbf{m}_1. \tag{2.7}$$

All matrices C_1 and $-C_1M^T$, and their products, constitute a group. Such groups of symmetry elements of the sections through functions of macroscopic boundary parameters were specified for all misorientations by Patala and Schuh (2013) for all crystallographic point groups. However, they were given in a general form in which they cannot be directly linked to the distribution functions

in the conventional representation. More convenient diagrams containing symmetry elements of the sections for the CSL misorientations for the O_h crystal symmetry are collected in Appx. B.

Boundary multiplicity

For some exceptional boundaries, not only $M = M'$, but also $\mathbf{m}'_1 = \mathbf{m}_1$, i.e., after application of symmetry transformations to a representation $\mathbf{B}$, we obtain an equivalent representation $\mathbf{B}'$ which is actually the same as the starting representation ($\mathbf{B} = \mathbf{B}'$). It is said that a boundary has the *multiplicity* of q if there exist q identical representations among its representations obtained by application of symmetry transformations.

Asymmetric domains

In the presence of symmetries, an asymmetric domain (termed also a fundamental zone) is a closed subset of the entire space of physical objects whose interior contains all possible points such that each of these points represents a physically distinguishable object. In the case of boundary space, these points correspond to distinct boundaries. The asymmetric domain for the boundary space has a very complex 'shape' (Patala and Schuh, 2013). The notion of multiplicity has been also considered for misorientations, e.g., by Field (1995). Moreover, fundamental zones for misorientations in various parameterizations (Euler angles, Rodrigues parameters) were specified; see, e.g., He and Jonas (2007); Heinz and Neumann (1991); Morawiec (1997); Morawiec and Field (1996); Zhao and Adams (1988). It should be noted that the borders of these fundamental zones consists of points (misorientations) having multiplicities greater than 1.

2.4 Grain boundary energy

By energy of a grain boundary we understand its excess free energy. The form of the relationship between the boundary energy and macroscopic boundary parameters is not explored yet, though multiple attempts have been made. For instance, Read and Shockley (1950) proposed a formula describing the boundary energy as a function of the disorientation angle. This well-known formula is, however, applicable to small-angle boundaries only. For large-angle boundaries, numerous theories were proposed. Although the model of Read and Shockley (1950) takes into account only one geometric parameter and ignores

the other four, Wolf (1989) tried to extend this model to large-angle boundaries. Besides that, some attention was drawn by the idea of estimating the energy based on the density of broken atomic bonds (Wolf, 1990a). The broken-bond model is also the basis of the solutions proposed by Wynblatt and Takashima (2001) and by Luo and Qin (2015). Moreover, there are theories which link the boundary energy to the level of plane matching (Pumphrey, 1972), plane interlocking (Fecht and Gleiter, 1985), hard-sphere packing (Ashby et al., 1978), or to excess free volume (Wolf, 1990b). Finally, the connections between boundary energy and the proximity of a given boundary to high-multiplicity boundaries (Sutton and Balluffi, 1987) or boundaries having two-dimensionally periodic structures (Sutton, 1991) were also considered. As pointed out by Bulatov et al. (2014), the existing models fail: one can find counterexamples for which they give incorrect results. Moreover, in some cases, it is non-trivial to link the energies directly to macroscopic boundary parameters. Until now, the most reliable theoretical predictions of the energy of a boundary having certain geometry can be obtained via molecular-dynamics simulations. Besides the atomistic simulations, there is an approach to experimental determination of relative boundary energies from geometry of triple junctions extracted from 3D grain-orientation maps.

2.4.1 Relative energies from geometry of triple junctions

Analysis of dihedral angles at triple lines is a way of studying anisotropy of boundary energy with respect to grain misorientations (e.g., Chalmers, 1949; Dunn and Lionetti, 1949; Smith, 1948), as well as with respect to both misorientations and indices of boundary planes (e.g., Hodgson and Mykura, 1973; McLean, 1973; Mori et al., 1988; Otsuki, 1996). Morawiec (2000) proposed a method for determining relative boundary energies in equilibrated polycrystals as functions of all five macroscopic boundary parameters. He also extended the previous considerations by incorporating crystal symmetry. In the proposed approach, it is assumed that three boundaries intersecting at a triple junction are in equilibrium, i.e., their surface tensions are equilibrated; in other words, they satisfy the Herring (1951) condition. This condition can be expressed in the formalism of capillarity vectors (Cahn and Hoffman, 1974; Hoffman and Cahn, 1972) as:

$$\left(\boldsymbol{\xi}_1 + \boldsymbol{\xi}_2 + \boldsymbol{\xi}_3\right) \times \mathbf{k} = 0, \tag{2.8}$$

where $\boldsymbol{\xi}_1$, $\boldsymbol{\xi}_2$, and $\boldsymbol{\xi}_3$ are the capillarity vectors ascribed to the three intersecting boundaries whereas $\mathbf{k}$ is the unit vector along the triple line. Each vector $\boldsymbol{\xi}_i$ $(i = 1, 2, 3)$ can be decomposed into a sum of a vector, $\boldsymbol{\xi}_{i,\perp}$, perpendicular to the corresponding boundary and a vector, $\boldsymbol{\xi}_{i,\parallel}$, parallel to that boundary. The vector $\boldsymbol{\xi}_{i,\perp}$ is expressed as $\gamma(\mathbf{m}_{1,i})\mathbf{m}_{1,i}$, where $\gamma(\mathbf{m}_{1,i})$ is the energy of a boundary with a fixed misorientation dependent on $\mathbf{m}_{1,i}$ – the normal to that boundary. For each registered triple junction, there is a separate equilibrium condition given by Eq.(2.8). These conditions constitute a system of linear equations. Since for each of these conditions, the vectors $\mathbf{m}_{1,i}$ and $\mathbf{k}$ are known from a measurement, it remains to determine the capillarity vectors $\boldsymbol{\xi}_i$ in order to compute the values of $\gamma(\mathbf{m}_{1,i})$. The latter can be computed up to a constant factor; this explains why only relative energies can be obtained using this approach. In practice, for computational reasons, the boundary space is partitioned into discrete bins (as in the case of computing distributions of boundary populations), and one capillarity vector, $\boldsymbol{\xi}_j$, is ascribed to each of these bins (j is the index of a bin). Then, using an iterative procedure, a set of capillarity vectors which satisfy the system of equations as nearly as possible is found. Eventually, analogously to boundary populations, the value $\gamma\boldsymbol{\xi} \cdot \mathbf{m}_1$ of the energy distribution at a given boundary is averaged over all bins containing symmetrically equivalent representations of that boundary. This approach was first applied to estimation of energies of boundaries in magnesia (Saylor et al., 2003b), then boundary energy distributions accompanied distributions of boundary populations obtained for miscellaneous materials (e.g., Beladi and Rohrer, 2013b; Dillon and Rohrer, 2009; Li et al., 2009; Rohrer et al., 2010). As an example, energies of boundaries in pure nickel obtained by Li et al. (2009) are reprinted in Fig. 2.8. Generally, it has been observed that high populations of certain boundaries are correlated with their low energies (see also Rohrer, 2011a,b).

2.4.2 Molecular-dynamics simulations

As was mentioned above, grain boundary energy can also be calculated using simulations at the atomic scale. It is assumed that grain boundaries are planar and infinite; in practice, the latter means sufficiently large with periodic boundary conditions imposed. Two blocks of atoms at their initial positions modeling structures of neighboring grains separated by a boundary plane are generated. Atoms are arranged in a way that reflects certain macroscopic boundary parameters. Then, a relaxation process takes place until the atoms reach the

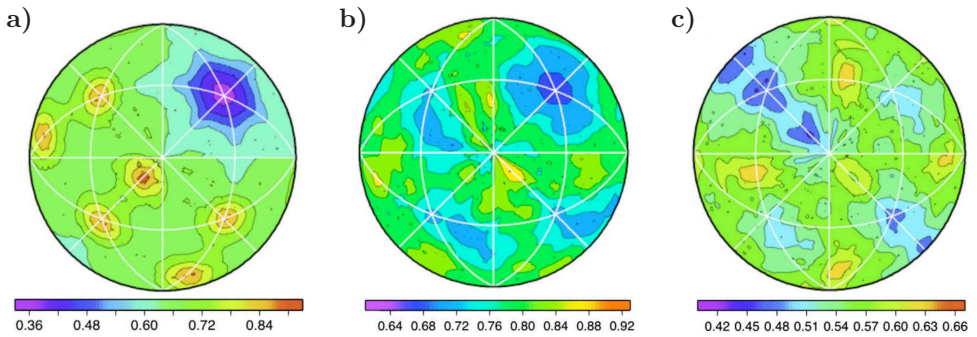

Figure 2.8: Relative energies of grain boundaries as functions of boundary planes for the *(a)* Σ3, *(b)* Σ7, and *(c)* Σ9 misorientations. These functions were computed based on geometries of triple junctions reconstructed from 3D-EBSD data acquired from pure Ni (reprinted from Li et al. (2009), with permission from Elsevier). To be compared to Fig. 2.4.

equilibrium state; they interact according to an assumed potential. Usually multiple initial configurations are considered, i.e., macroscopic boundary parameters are always the same, but microscopic shifts vary. Moreover, when two atoms of adjacent grains overlap in the initial state, one of them is removed, and various selections are considered. Boundary energies are computed after relaxation for each initial arrangement, and the minimum value is assumed to be the true boundary energy. The most extensive works concerning molecular-dynamics simulations of boundary energies in FCC metals contained results for 388 distinct macroscopic configurations (Holm et al., 2010; Olmsted et al., 2009) for four pure metals. It was also reported that, for FCC metals, the function relating the boundary energy to macroscopic parameters is in a sense universal, and energies between metals differ by a factor related to the Voigt average shear modulus (Holm et al., 2010; Olmsted et al., 2009; Udler and Seidman, 1996). Bulatov et al. (2014) used the results obtained by Olmsted et al. (2009) for construction of an interpolating function describing the geometry-energy relationship for boundaries in FCC metals. There are also two data bases containing boundary energies for a series of macroscopic arrangements for BCC metals: Kim et al. (2011) computed energies of 66339 boundaries in iron, while Ratanaphan et al. (2015) obtained 408 boundary energies for iron and molybdenum. According to Ratanaphan et al. (2015), "Fe and Mo have strongly correlated energies that scale with the ratio of the cohesive energies of the two metals". The above-mentioned data bases will be used in Sec. 8.2 for interpretation of experimental grain boundary distributions.

2.5 Computer programs related to boundary analysis

Due to the multitude of symmetrically equivalent representations of each physical boundary which need to be taken into consideration, it is difficult to imagine characterization of even individual boundaries 'by hand' without dedicated software, not to mention large boundary networks. There exist numerous software solutions for post-processing of orientation maps obtained via EBSD setups, e.g., *OIM Analysis* of EDAX-TSL, *HKL Channel5* of Oxford Instruments, *MTEX* (Bachmann et al., 2011), and *DREAM.3D* (Groeber and Jackson, 2014). These programs are capable of clean-up of raw data, alignment of subsequent layers (in the case of sectioned 3D maps), and – what is the most important from our point of view – detection of grain boundaries; *DREAM.3D* can also be used for reconstruction of boundary surfaces in the form of triangular meshes and for smoothing of the obtained surfaces. This was the tool of choice for reconstruction of 3D boundary networks analyzed in this work. Besides *DREAM.3D*, there are also other programs designed to extract surfaces of boundaries from voxelized data and to smooth or to simplify the obtained meshes (Dillard et al., 2007; Lee et al., 2014; Moore et al., 2009). Other programs compute distributions of boundary populations (Saylor et al., 2003a) and boundary energies (Saylor et al., 2003b) as functions of either five macroscopic parameters or boundary planes only. Misorientation distribution functions can be calculated using, e.g., *MTEX* and *OIM Analysis*. Programs intended to support boundary studies in the atomic scale like, e.g., *GBstudio* (Ogawa, 2006) and *GBgeom* (Karthikeyan and Saroja, 2013) are also worth mentioning.

2.6 Problem statement

As we see, a number of approaches to geometric characterization of both individual grain boundaries and complex boundary networks have evolved. Let us now indicate the issues arising when it comes to practical applications of these approaches.

2.6.1 Shortcomings of parameters describing boundary characters

The parameters which may be used for sorting boundaries into groups of near-tilt, near-twist, and mixed boundaries have been revised. However, the most obvious question 'Which of them should be used?' has not been clearly an-

swered yet. Furthermore, each of these parameters have certain drawbacks which are shortly described below.

Inadequacy of parameters based on disorientations

Because of ease it is tempting to use either the tilt/twist component parameter or the decomposition limited to disorientation-based boundary representations. As was mentioned earlier, this leads to a unique TTC (α) and to unique twist (ν) and tilt (λ) angles, respectively. The distributions of these three angles are simple and smooth. They vary continuously with misorientation and plane parameters (Figs. 2.1a and b, Fig. 2.2). These computationally convenient approaches have, however, a relevant negative aspect. Certain features of boundaries are not apparent when only the smallest-angle representations are considered; to expose these features, all symmetries need to be taken into account. The classic example of that is the coherent twin boundary in FCC metals. Geometry of the twin boundary is described by the (111) boundary plane and the $\Sigma 3$ misorientation which is a rotation by 60° about the [111] axis. The corresponding interface matrix is

$$\mathbf{B}_{\text{twin}} = \frac{1}{\sqrt{3}} \begin{bmatrix} 0 & -1 & -1 & -1 \\ 1 & \frac{2}{\sqrt{3}} & -\frac{1}{\sqrt{3}} & \frac{2}{\sqrt{3}} \\ 1 & \frac{2}{\sqrt{3}} & \frac{2}{\sqrt{3}} & -\frac{1}{\sqrt{3}} \\ 1 & -\frac{1}{\sqrt{3}} & \frac{2}{\sqrt{3}} & \frac{2}{\sqrt{3}} \end{bmatrix}. \tag{2.9}$$

In this representation, this boundary fits the definition of a pure-twist boundary. Also, the corresponding $\alpha = 0$, $\lambda = 0$, and $\nu > 0$ indicate its pure-twist character. It is well-known, however, that this boundary can also be seen as a pure-tilt boundary. This property can be detected only by considering the representations with larger misorientation angles, i.e., it is not detectable within the scheme limited to disorientations. We apply a symmetry transformation which is a 90° rotation about [001] represented by the matrix

$$C_2 = \begin{bmatrix} 0 & -1 & 0 \\ 1 & 0 & 0 \\ 0 & 0 & 1 \end{bmatrix} \tag{2.10}$$

to one of the grains of the twin. Thus, we obtain an equivalent representation of the twin boundary

$$\mathbf{B}_{\text{twin}}\mathbf{C}_2^T = \frac{1}{\sqrt{3}}\begin{bmatrix} 0 & 1 & -1 & -1 \\ 1 & \frac{1}{\sqrt{3}} & \frac{2}{\sqrt{3}} & \frac{2}{\sqrt{3}} \\ 1 & -\frac{2}{\sqrt{3}} & \frac{2}{\sqrt{3}} & -\frac{1}{\sqrt{3}} \\ 1 & -\frac{2}{\sqrt{3}} & -\frac{1}{\sqrt{3}} & \frac{2}{\sqrt{3}} \end{bmatrix}. \tag{2.11}$$

In $\mathbf{B}_{\text{twin}}\mathbf{C}_2^T$, the entries related to the misorientation correspond to a rotation by 70.53° about the $[01\bar{1}]$ axis. Hence, the tilt character of the twin boundary becomes apparent as this misorientation axis lies in the (111) plane. Similar considerations are applicable to other boundaries. For instance, almost all low-Σ twist boundaries have also tilt character (Morawiec, 2011).

A more general argument against using disorientations is that its definition relies on one of the five macroscopic boundary parameters (the misorientation angle), and in the case of large-angle boundaries, there is no reason for distinguishing this particular parameter as having more significance than the other four parameters.

From the above discourse, it can be already concluded that parameters whose definitions are restricted to boundary representations with disorientations (and ignore other equivalent representations) do not provide complete geometric specification of a boundary.

Time-consuming computation of the distances to the nearest tilts and twists

Detection of tilt and twist boundaries based on their distances to the nearest tilt (δ_L) and nearest twist (δ_N) boundaries – thanks to its rigorous mathematical roots – seems to be the most reliable method and it is convenient for analysis of error-affected data. Unfortunately, its usefulness is limited by its high computational costs. It requires running complex numerical optimization algorithms. As a consequence times needed for processing grain boundary data become very long.

Fortes decomposition

The smallest tilt (λ_F) and smallest twist (ν_F) angles proposed by Fortes – by their definitions – include analysis of symmetrically equivalent boundary representations. Moreover, they can be quickly calculated using simple formulas. The distances δ_L to the nearest pure tilt take the value of zero for the same

boundaries as the angles ν_F of twist components (Figs. 2.3a and 2.1a). Similarly, δ_N and λ_F vanish at the same locations in the boundary space (Figs 2.3b and 2.1b). Hence, δ_L and δ_N are suspected to be correlated to ν_F and λ_F, respectively. These correlations, however, have not been explored, and the question arises if it would be possible to substitute the distances to the nearest twist and nearest tilt boundaries by the minimum tilt and twist angles, respectively. Although the decomposition is mentioned in almost every 'introduction to grain boundaries' (Grabski, 1969; Randle, 1993; Sutton and Balluffi, 2007; Wolf and Yip, 1993), it has never been applied to analysis of experimental data.

Symmetric and 180°-tilt boundaries

Besides tilt and twist boundaries, other reference boundaries are distinguished, but (prior to Glowinski (2014)) no papers that would deal with the problem of recognizing symmetric and 180°-tilt boundaries or estimating the frequencies of occurrence of boundaries of these types have been published.

2.6.2 Artifacts originating from the partition-based method

Although the partition-based method has been successfully applied to computation of grain-boundary distributions for various materials, it has deficiencies leading to artifacts in the computed distributions, and complicating estimation of the reliability of the distributions.

It is easy to see that the partition results in elongated bins. For instance, the Φ-dimensions of 10°-bins with $\cos\Phi$ in the ranges $[0, \frac{1}{9}]$ and $[\frac{8}{9}, 1]$ are, respectively, 6.4° and 27.3°. The disparities in the bin dimensions are schematically illustrated in Fig. 2.9a. Large bin elongation should be avoided because boundaries at the opposing extremities of a long bin have significantly different geometries. Moreover, the bin sizes do not really correspond to experimental resolutions, which – in the case of EBSD-based data – are believed to be about 1° for misorientations and about 7.5° for boundary planes (Saylor et al., 2003a). With a sufficiently large data set, the volumes of the bins could be reduced by increasing k and k'. Such an increase, however, does not eliminate the bin elongation, and it results in even larger relative differences between angular dimensions of the shortest and the longest bins. For instance, with 3°-bins ($k = 30$), the bin dimensions, in terms of Φ and ψ, are 1.9° and 14.8°, respectively. Also, the last stage of the method, i.e., determining the distribution

value at a given boundary as an average over the bins containing equivalent representations of that boundary, turns out to be problematic. In the presence of elongated bins, the averaging smooths but also excessively flattens the resulting distributions. In consequence, weak maxima may become indistinguishable from the background.

To illustrate artifacts in boundary distributions obtained by the partition-based method, let us examine an artificial test function containing two individual boundary types: the symmetric $\Sigma 5$ (36.9°/[100] misorientation) boundaries with (012) planes and the (FCC twin) boundaries with $\Sigma 3$ ([111]/60°) misorientations and (111) planes. Two nearly point-like maxima are expected at the (012) and $(0\bar{2}1)$ poles in the $\Sigma 5$ section of the distribution, and a single peak at the (111) pole in the $\Sigma 3$ section. Values for all other boundary types should be zero. However, in the distribution obtained by the partition-based method, besides the expected peaks, also artifacts are observed. In the $\Sigma 5$ section calculated using 10°-bins the peaks are spread along the [010] direction (Fig. 2.9b). In the $\Sigma 3$ section, the peak at the (111) pole has full width at half-maximum of about 7° (Fig. 2.9c). Its "tail" is still visible at the neighborhood of the $(\bar{1}11)$ pole for the 57°/[110] misorientation, which is 13.5° away from the 70.5°/[110] misorientation – one of equivalent representatives of $\Sigma 3$ (Fig. 2.9d). The tail is also present in the closer 50°/[111] section (Fig. 2.9e); this section has been considered without accounting for the impact of the peak at the twin boundary (Randle et al., 2008; Rohrer et al., 2006). Clearly, large spread of peaks causes difficulties in interpretation of the distributions.

The method for computing boundary-plane distributions averaged over misorientations, which also uses bins, inherits all drawbacks of the partition-based approach. Therefore, resulting distributions may also be affected by the elongated bins.

2.6.3 Incomplete interpretation of boundary distributions

Besides the fact that grain-boundary distributions are computed using the partition-based method which has its imperfections, also the interpretation of the obtained distributions is often inexhaustive.

The five-dimensional space of macroscopic boundary parameters is vast. Therefore, to obtain reliable boundary distributions, the studied microstructure volumes must contain adequately large numbers of boundaries. Generally, the more boundaries in a sample, the less the error of a distribution. However, no prescription how to evaluate these errors in a quantitative way has been

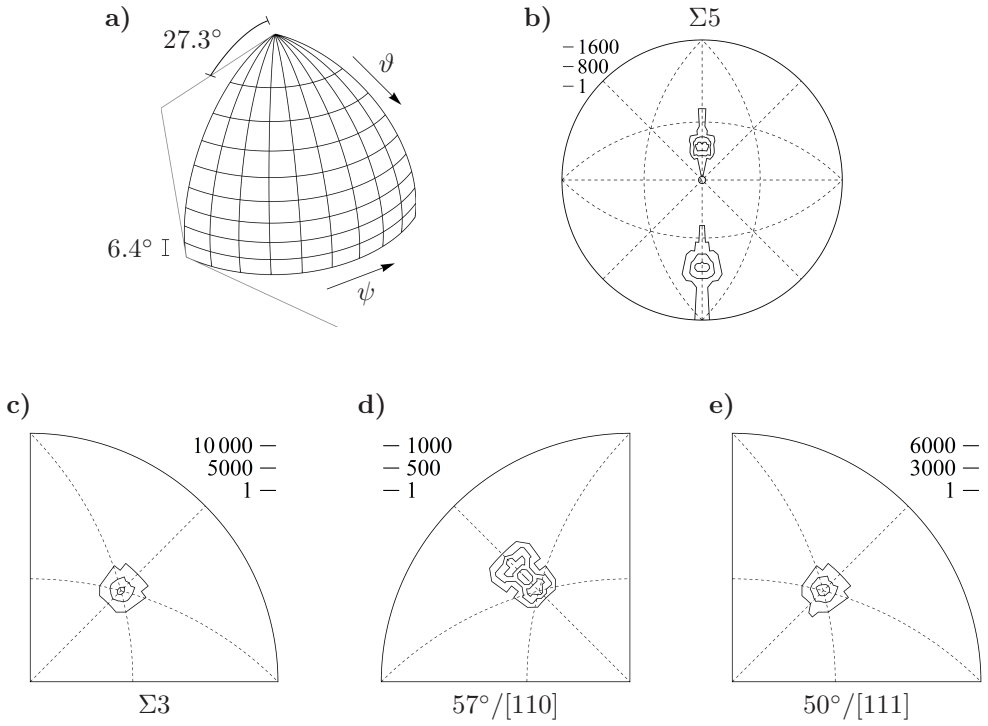

Figure 2.9: *(a)* Schematic illustration of the angular dimensions of the "10°-bins" in the partition-based method. *(b)* Σ5 section through the test distribution obtained by the partition-based approach with "10°-bins". *(c,d,e)* Essential parts of the sections through the test distribution computed using the partition into "10°-bins" for the misorientations Σ3, 57°/[110] and 50°/[111], respectively.

given.

As was stated previously, only a tool for boundary analysis which does take into account all symmetries will uncover all information on the boundary type. The same is valid for diagrams containing locations of tilt and twist boundaries; cf. Sec 2.3.4. Moreover, without complete diagrams it is not possible to indicate boundaries which can be classified as multiple-tilt boundaries (those lying on the intersections of tilt zones) and those qualified to more than one group simultaneously.

It may also be helpful to identify symmetry axes and mirror lines of the analyzed sections through grain-boundary distributions. With the knowledge of these symmetries, it is easy to indicate peaks and valleys of the distributions corresponding to the same physical configurations at boundaries (Patala and Schuh, 2013, and Appx. B).

2.6.4 Capabilities missing in the existing software

Although a variety of software tools can be found on the market, none of them are capable of a complete geometric characterization of boundaries, e.g., resolving whether a boundary can be classified as twist, tilt, symmetric, etc., or providing numerical values of the deviations of a given boundary from the nearest geometrically characteristic boundaries (like pure-tilt, pure-twist, pure-symmetric et cetera). No software which could identify symmetries of the distributions or locate geometrically characteristic boundaries in the boundary space has been released.

Chapter 3

Objectives of this work

The problems encountered in cataloging of grain boundaries based on their geometry, and in computation and interpretation of grain-boundary distributions have been scrutinized in the last section. The purpose of this work is to develop new methods for recognizing boundary types and for analysis of the distributions which will allow for elimination of the known issues. In parallel to the development of the methods themselves, a dedicated computer program implementing the new approaches has been created. The new tools are tested using six grain boundary data sets acquired from several different materials; these data sets were provided by experimentalists; see Appx. A. The following tasks are fulfilled within this work:

- The advantages and disadvantages of Fortes decomposition are studied in detail. In particular, correlations between the smallest tilt angle λ_F and the distance δ_N to the nearest twist boundary, and between the smallest twist angle ν_F and the distance δ_L to the nearest tilt boundary are examined. The experience gained from these studies leads to definition of completely new parameters which substitute the accurate distances δ_N and δ_L and which are, at the same time, fast to calculate. Then, these considerations are extended to description of closeness of a boundary to a symmetric and a 180°-tilt configurations.

- The approximate distances to tilt, twist, symmetric, and 180°-tilt boundaries are used for estimation of the fractions of boundaries of these types in the microstructures of ferritic steel and Ni-base superalloy IN100 (i.e., in Ferrite and Small IN100 data sets, respectively).

- An alternative approach to computation of the boundary distributions is presented. Suggestions given by Morawiec (2012b) are followed to

adapt the kernel density estimation (KDE) technique and to replace the partition of the boundary space into bins by probing the distributions at selected points and counting boundaries that are not farther from those points than an assumed limiting distance defined in the boundary space. It is shown that this change of the computation method leads to significant improvements in the quality of resulting distributions.

- A scheme of interpretation of grain-boundary distributions is elaborated. It includes ways of evaluation of their reliability (e.g., estimation of statistical errors of distribution values and verification of the numbers of distinct boundaries contributing to maxima), identification of their symmetries, and locating of reference boundaries in these distributions. The diagrams with locations of tilt, twist, symmetric, etc. boundaries for fixed misorientations are obtained using two complementary methods: numerical searches based on the approximate distances to the nearest characteristic boundaries and analytical calculations.

- The KDE-based method is adapted to computation of distributions of boundary planes in both crystallite and laboratory reference frames.

- The new tools for studying populations of grain boundaries as functions of the macroscopic boundary parameters are demonstrated using 3D data sets collected from nickel (i.e., using Nickel (CMU) and (UGent) data sets), Ni-based superalloy IN100 (Small and Big IN100), ferritic steel (Ferrite), and yttria (Yttria).

- A computer program containing implementations of all the new methods and several useful tools which are missing in the existing software is created. Capabilities of this software are described.

Chapter 4

Reconstruction of boundary networks

In order to analyze grain boundary networks, macroscopic parameters of boundaries must be extracted from 3D data sets. Each data set that is studied in this work (see Appx. A) comes as a stack of 2D orientation maps registered alternately with removal of subsequent slices of a material. By the nature of 3D-EBSD experiments, consecutive slices are often misaligned; moreover, the maps usually contain many unindexed, so-called 'bad', pixels. Therefore, raw data need to be aligned and 'cleaned up'. All of the considered 3D data sets were acquired using EBSD systems manufactured by *EDAX-TSL*, hence, they were post-processed in a similar fashion. For this purpose, *DREAM.3D* software was the tool of choice.

Data clean-up

At the beginning, the raw data were arranged to create 3D images from 2D maps. At the same time the layers were shifted in a way that maximizes the number of pairs of voxels with each voxel belonging to different of the two adjacent slices, but having similar orientations (i.e., differing by less than 5°). The only exception was Nickel (UGent) data set which was aligned by H. Pirgazi who used his own algorithm. Moreover, voxels of Confidence Index (CI) or Image Quality (IQ) less than 0.1 and 120, respectively, were classified as bad[9]. Then, the imported images were cropped in order to remove bad pixels at their peripheries and to get rid of unevenness of the image borders resulting from shifting of the layers. Since Yttria data set contained relatively

[9]CI and IQ are standard (in EBSD systems of *EDAX-TSL*) parameters describing reliability of measurements.

large parts of 'noisy' data, it was divided into three subsets, and each of these subsets was cropped in a different way in order not to waste the regions of good quality data.

In the next step, the bad voxels whose orientations deviated from the orientations of its l immediate neighbors by less than 5° became 'good' voxels. This step was repeated for l equal to 6, then 5, then 4. Afterward, for each voxel with CI < 0.2 which had at least m immediate neighbors with different orientations (assuming the tolerance of 5°), and at least m of these neighbors had the same orientations (different from that of the reference voxel), the reference voxel inherited the orientation and CI of the neighbor with the highest CI. This procedure was repeated for m in the range from 6 down to 2.

Grains were constructed from groups of voxels whose orientations were close (again, assuming the tolerance of 5°). Grains composed of too few voxels were removed (all their voxels were marked as bad). Minimum grain sizes (from 5 to 60 voxels) were optimized for each data set based on the corresponding grain-diameter distributions: the artificial peaks at diameters ≈ 0 were cut-off keeping simultaneously as many grains as possible. Furthermore, grains entirely 'immersed' in other grains (i.e., grains having only one neighboring grain) were also removed. After these stages, a single orientation was ascribed to each of the existing grains: the orientation of a given grain was computed as an average over orientations ascribed to voxels building that grain. Finally, the grains were iteratively dilated in order to clear out all remaining bad voxels; depending on the data set, from one to three iterations were performed. All data sets after completed post-processing are presented in Fig. A.1 in the form of 3D inverse pole figure maps. Now, having cleaned-up the raw data, one can reconstruct geometric surfaces of grain boundaries.

Reconstruction of boundary surfaces

The data sets are still composed of cuboid voxels, so if we extracted grain boundaries as they are, they would have stepped structures. Therefore, Marching Cubes algorithm was used for initial reconstruction of boundary surfaces; it gives grain boundary networks represented in the form of meshes of traingular segments. Then, the initial boundary surfaces were smoothed using Laplacian algorithm. The control parameters of the smoothing were carefully selected for each data set. Examples of reconstructed boundaries are visualized in Fig. 4.1.

Now, macroscopic boundary parameters can be easily assigned to each segment. These segments will be the input to further analyses; areas of the seg-

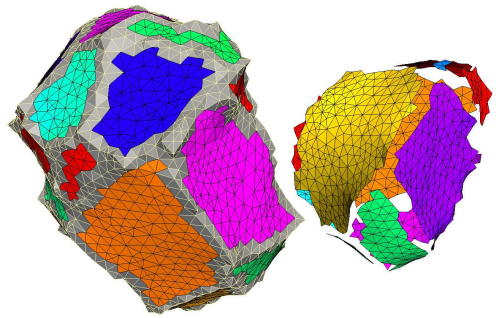

Figure 4.1: Visualization of boundaries of selected grains (from Small IN100 data) reconstructed in the form of triangular meshes; different colors represent distinct boundaries. In the left-hand side grain, the segments neighboring the triple lines (excluded from the analyses) are shaded with grey color.

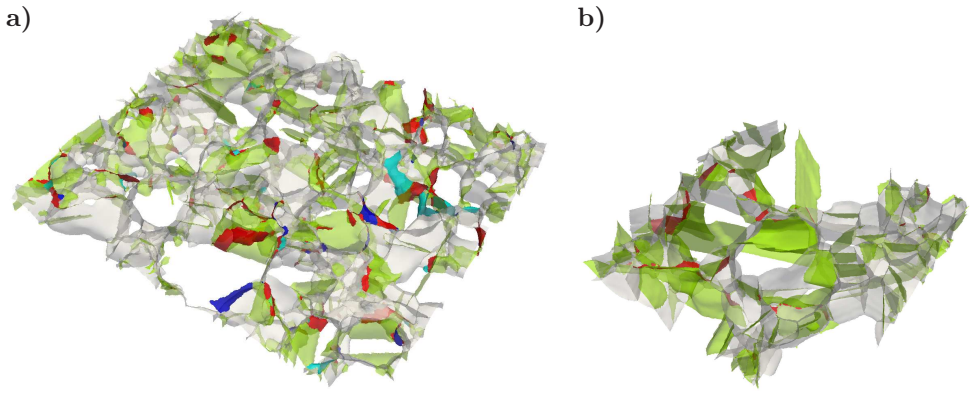

Figure 4.2: Visualizations of grain boundary networks extracted from *(a)* Nickel (CMU), *(b)* Nickel (UGent) data sets; $\Sigma 3$, $\Sigma 9$, $\Sigma 27a$, and $\Sigma 27b$ boundaries are colored with green, red, cyan, and blue, respectively.

Table 4.1: Numbers of distinct grain boundaries and mesh segments constituting boundary networks reconstructed from 3D data sets.

Data set	Number of boundaries	Number of mesh segments
Nickel (CMU)	$3,600$	5.3×10^6
Nickel (UGent)	$1,100$	1.5×10^6
Small IN100	$13,000$	1.3×10^6
Big IN100	$57,000$	1.2×10^6
Ferrite	$8,300$	1.4×10^6
Yttria	$41,000$	7.5×10^6

ments will be treated as weights. The above reconstruction (and smoothing) algorithms, however, tend to leave some non-smooth (stepped) triple lines. Although the mesh segments directly neighboring these lines may constitute up to about 40% of all segments, they were excluded from further analyses because it was noticed that they lead to significant artifacts in the distribution of boundary planes given in the laboratory frame (Sec. 6.3.1). The numbers of distinct grain boundaries and the corresponding numbers of mesh segments for each data set were collected in Tab. 4.1. Fig. 4.2 presents examples of whole boundary networks extracted from the 3D data.

Chapter 5

Methods for quantifying the character of a boundary

In this chapter, various approaches to recognizing the character of boundaries are studied. Applicability of Fortes decomposition is shown to be limited. In particular, the correlations between tilt (twist) angles and distances to the nearest twist (tilt) boundaries are explored. With the knowledge of properties of the tilt and twist components, new parameters quantifying tilt and twist[10] characters of boundaries are defined and proved to be a reliable replacement for the distances. Finally, these considerations are extended to the description of symmetric and 180°-tilt character of boundaries. In order to get acquainted with all the parameters used for describing boundary geometries (and differences between these parameters), they are used for analysis of the characters of boundaries in Small IN100 and Ferrite data sets.

5.1 Tilt and twist characters

5.1.1 Applicability of Fortes decomposition

Let us go back to the example with the FCC coherent twin boundary discussed in Sec. 2.6.1. For the representation given by the $60°/[111]$ misorientation and (111) boundary plane (i.e., $\mathbf{B}_{\text{twin}}$), the twist angle is 60°, while the tilt angle is 0. For the equivalent representation given by the $70.53°/[01\bar{1}]$ misorientation and (111) boundary plane (i.e., $\mathbf{B}_{\text{twin}}C_2^T$), the twist angle is 0, while the tilt angle is 70.53°. Thus, one concludes that this boundary has one representation

[10] Throughout this work, by tilt, twist, and symmetric boundaries one should understand all boundaries satisfying definitions given in Sec. 2.2, including boundaries with high-index misorientation axes and high-index boundary planes.

with vanishing tilt component (minimum tilt angle λ_F is equal to 0), and another one with vanishing twist component (minimum twist angle $\nu_F = 0$), i.e., the boundary has a twist-tilt character. Clearly, the Fortes method reveals the pure-twist and pure-tilt boundaries. Let us verify if the angles ν_F, λ_F may serve as quantitative measures of the twist and tilt contributions to a mixed boundary. The distances δ_L to the nearest pure-tilt take the value of zero for the same boundaries as the angles ν_F of twist components (Figs. 2.1c and 2.3a). Similarly, δ_N and λ_F vanish at the same locations in the boundary space (Figs. 2.1d and 2.3b). Hence, δ_L and δ_N are expected to be correlated to ν_F and λ_F, respectively. This is true only for the distances δ_N and the angles λ_F; the correlation between ν_F and δ_L turns out to be relatively poor (Fig. 5.1). Some roughness of the distribution of the angle ν_F can be easily noticed; see the yellow circle in Fig. 2.1c. To give a numerical example, let us consider the decomposition of the boundary having boundary normal given by

$$\mathbf{m}_1 = [\ \xi \quad 0 \quad \sqrt{1-\xi^2}\ ]^T \tag{5.1}$$

and misorientation being a rotation by 45° about the axis $\mathbf{m}_1$, and let $0 \leq \xi \leq 1$. In the presence of symmetries, the angle ν_F approaches 45° as ξ approaches 0; e.g., $\nu_F \approx 44.97°$ for $\xi = 0.0003$. For $\xi > 0$, this boundary represents explicitly twist boundaries, but when ξ equals 0, the boundary has also pure-tilt character and the angle ν_F of the twist component drops from nearly 45° to zero. This example shows the discontinuity of the components with respect to the macroscopic boundary parameters. With such discontinuities and lack of smoothness, the twist and tilt components cannot be reliably estimated from error-affected experimental data.

It is worth adding that although λ_F and ν_F are just rotation angles, whereas distances δ_N and δ_L involve both rotation angles and angles between boundary normals, still the angles of components are frequently larger than the corresponding distances. The maximal values of the considered parameters are

$$\max(\nu_F) \approx 45°,\ \max(\lambda_F) \approx 54.7° \text{ and } \max(\delta_L) \approx 7.4°,\ \max(\delta_N) \approx 28.3°; \tag{5.2}$$

the data for δ_N and δ_L are cited after Morawiec (2009b), the largest ν_F corresponds to the case described above by Eq.(5.1), and the largest λ_F is obtained by decomposition of the 40.2°/[011] misorientation with respect to $\mathbf{m}_1 = [\ 1 \quad 0 \quad 0\ ]^T$.

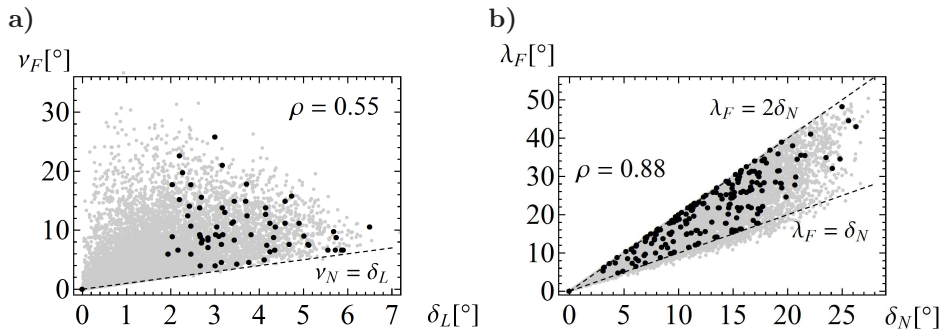

Figure 5.1: The angles of Fortes decomposition and distances to the nearest tilt or twist boundaries for 10^4 randomly generated boundaries (gray points). Black points represent boundaries for low-Σ ($\Sigma 3$ – $\Sigma 9$) misorientations and low-index (absolute value ≤ 4) planes. Figures illustrate the pairs ν_F and δ_L (a), λ_F and δ_N (b). The symbol ρ denotes the Spearman's rank correlation coefficient for the random data.

5.1.2 Extreme values of the TTC parameter

The $|\mathbf{u} \cdot \mathbf{m}_1|$ parameter is also affected by crystal symmetries: although it is not influenced by the grain exchange nor by the choice of the sense of $\mathbf{m}_1$, it still takes a number of values. Again, with TTC parameters computed for boundary representatives with disorientations, only partial information about the boundary character is revealed. Similarly as in Fortes decomposition, one may eliminate the ambiguity by choosing the axes leading to either minimal or maximal values of $|\mathbf{m}_1 \cdot \mathbf{u}|$ or α. Such parameters have not been used before. Although interpretation of the extremal values $\alpha_N = \min(\alpha)$ and $\alpha_L = 90° - \max(\alpha)$ of α differs from that of the distances δ_N and δ_L, these pairs turn out to be close. Numerical tests for the cubic case indicate that $\alpha_N \geq \delta_N$ and $\alpha_L \geq \delta_L$. Moreover, α_L and α_N are not larger than about 10° and 29°, respectively; cf. Eq.(5.2). The distributions of α_L and α_N resemble those of δ_L and δ_N (Fig. 5.2). More generally, the parameters α_L and α_N are strongly correlated to δ_L and δ_N, respectively. These correlations are demonstrated in Fig. 5.3.

Based on the closeness of the pairs (α_L, α_N) and (δ_L, δ_N), statistical results obtained from experimental data using α_L and α_N are expected to be similar to corresponding results based on δ_L and δ_N. Indeed, PDFs (obtained for random boundaries) for α_L and α_N are similar to those for δ_L and δ_N, respectively (Fig. 5.4). On the other hand, the former are easier to compute than the latter: the code is simpler, and the running time was about 10^3 times shorter.

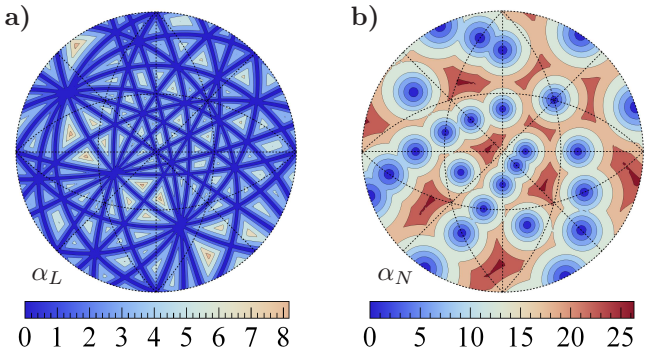

Figure 5.2: Distributions of the parameters α_L *(a)* and α_N *(b)* as functions of boundary planes for the Σ7 misorientation (for the cubic symmetry). Contours are given in degrees and are displayed in stereographic projection.

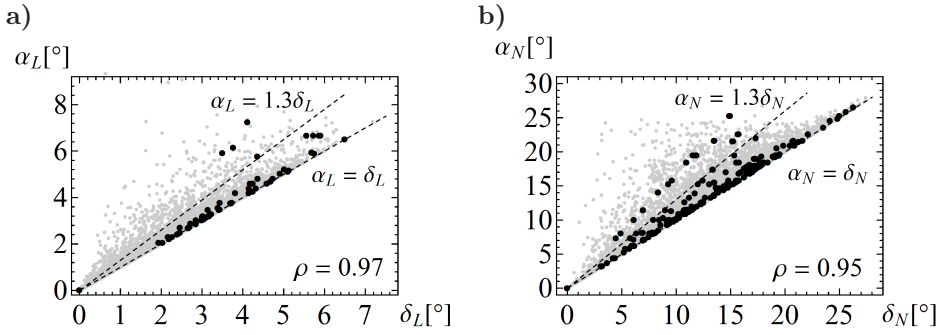

Figure 5.3: The angles α_L versus δ_L (a), and α_N versus δ_N for 10^4 randomly generated boundaries (gray points). Black points represent boundaries for low-Σ (Σ3 – Σ9) misorientations and low-index (absolute value ≤ 4) planes. In (a), boundaries between the continuous lines with $\delta_L \leq \alpha_L \leq 1.3\ \delta_L$ constitute 91.2% of all boundaries. In (b), boundaries between the continuous lines with $\delta_N \leq \alpha_N \leq 1.3\ \delta_N$ constitute 92.3% of all boundaries. As above, ρ is the Spearman's rank correlation coefficient for the random data.

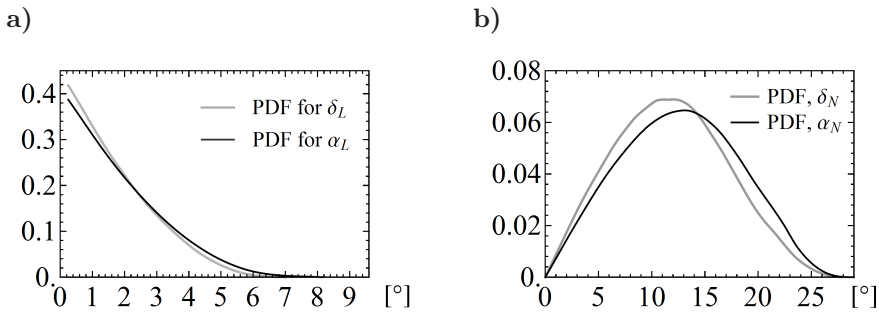

Figure 5.4: Probability density functions for *(a)* δ_L and α_L and *(b)* δ_L and α_L for random boundaries for the cubic O_h crystal symmetry.

5.1.3 Example: tilt and twist boundaries in Small IN100

The simplest way to evaluate the frequencies of occurrence of near-tilt and near-twist boundaries is to calculate the distributions of the distances δ_N and δ_L, parameters α_N and α_L, or angle λ_F. Potential peaks at zero would indicate the elevated amount of the boundaries of a given type. Such distributions were computed for Small IN100 grain boundary data set. The distributions were strongly affected by the high frequency of twins. In order to examine this impact, separate distributions were also calculated for boundaries differing from $\Sigma 3$ by more than 2°. Besides that, to speed up data processing, the boundary mesh extracted from Small IN100 data was simplified using *QSlim* program (Garland and Heckbert, 1997): the same boundary surfaces were approximated using larger mesh segments; thus, the number of segments was reduced from 1.6×10^6 to 3.5×10^5.

To illustrate the convention used for representation of the distributions, let us start with the familiar distribution of disorientation angles (the most basic one-dimensional projection of a grain-boundary distribution). It is presented in two forms: the conventional one, and the second one, expressed in terms of multiples of the random distribution (Fig. 5.5); all remaining distributions are shown only as multiples of corresponding random distributions. (The latter were obtained numerically by generating at least 10^6 random boundaries.) The disorientation-angle distribution has a very strong peak at 60°. This result is consistent with the presence of twins. Because of experimental errors and data processing methods, only points at the high-end ($7^\circ \leq \omega \leq 15^\circ$) of small-angle boundaries are reliable, and the boundaries in this range are over-represented. Besides that, the distribution is relatively flat. When the

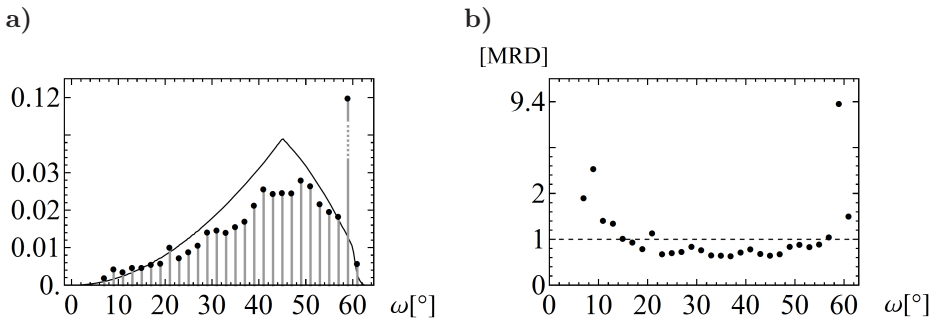

Figure 5.5: (*a*) Conventional form of the distribution of the disorientation angle for the analyzed Ni-based alloy. Continuous line represents Mackenzie (random) distribution. (*b*) The same distribution as in (*a*), but shown as multiples of the random distribution. Because of data processing, only the points on the right-hand side of the dashed line are reliable. In this and the remaining figures, the bin size is equal to the inverse of density of displayed points.

distribution is expressed as MRDs, it can be directly read which disorientation angles occur more and less frequently compared to random data (i.e., whether the distribution value is greater or less than unity, respectively).

The distributions of the distance to the nearest pure-twist boundary δ_N, the minimal TTC parameter α_N, and the smallest tilt angle λ_F are shown in Figs. 5.6a, b, and c, respectively. As one could expect, there is not much difference in shapes of these functions (as these parameters are strongly correlated). Let us focus on the graph for α_N. Elevated values near $\alpha_N = 0°$ indicate that twist boundaries are over-represented. This is also true for the data without $\Sigma 3$ boundaries, but the values are lower than in the case of the complete data set. The width of the peak at $\alpha_N = 0°$ is relatively large; it spreads beyond $\alpha_N \approx 10°$. Then, for $\alpha_N \geq 11°$, the values of the distribution are below 1 MRD. These low values are attributed to the balance requirement: if some data (near $\alpha_N = 0°$) are above 1 MRD, there must be data below 1 MRD. This is confirmed by the fact that the minimum becomes shallow when $\Sigma 3$ boundaries are removed and the maximum at $\alpha_N = 0°$ diminishes. The results at the far end of the abscissa are affected by large errors because of low probability of occurrence of such boundaries.

It remains to consider the population of near-tilt boundaries. The parameter ν_F, as not stable with respect to perturbations of input data, must be excluded. The distributions of δ_L and α_L are shown in Figs. 5.6d and e, respectively. Their reliability is low because of low resolution of the investigated

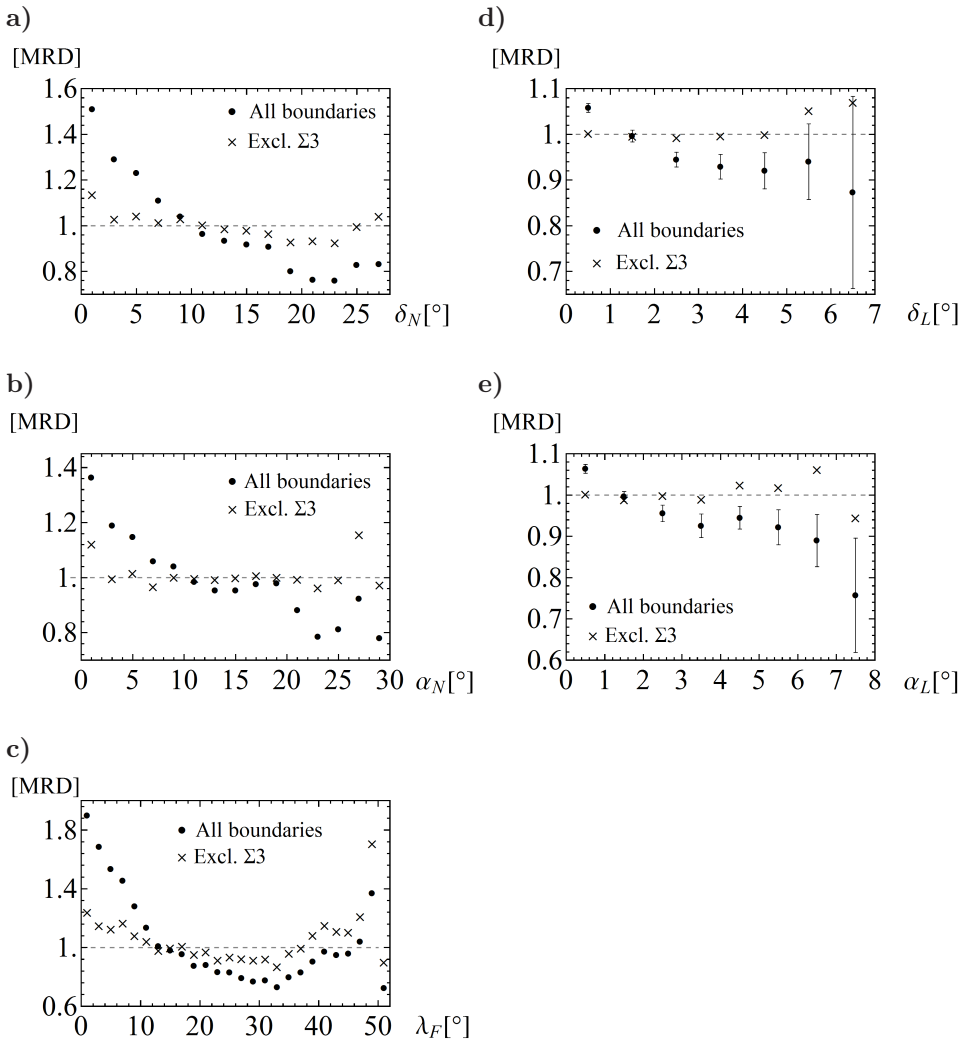

Figure 5.6: Distributions of the parameters describing closeness to twist (left-hand side column) and tilt (right-hand side column) boundaries for Small IN100: *(a)* distribution of the distance δ_N to the nearest pure-twist boundary, *(b)* and distribution of α_N *(c)* distribution of the smallest angle of tilt component λ_F, *(d)* distribution of the distance δ_L to the nearest pure-tilt boundary, and *(e)* distribution of α_L. Disks represent results obtained from the complete data set, and crosses correspond to the data without Σ3 boundaries. Because of the shape of the random distribution, the larger value on the abscissa the larger errors of the presented results. This is illustrated in *(d)* and *(e)* by the error bars. Relative lengths of the bars represent only statistical errors linked to the number of counts. They do not include the errors in measuring boundary inclinations and misorientations, which are the main cause of the flattening of the distribution.

data. Moreover, as the probability of occurrence of boundaries strongly decreases with growing δ_L and α_L (Morawiec, 2009b), so does the reliability of the distributions. For the complete data set, the values of the distributions at the most reliable points near $\delta_L = 0^\circ = \alpha_L$ slightly exceed 1. This means that the tilt boundaries are over-represented. The elevation is attributed to the twin boundaries. For the set without $\Sigma 3$ boundaries, the distributions at zero are practically the same as in the random case.

5.2 Symmetric and 180°-tilt characters

Analogously to boundaries of tilt and twist geometries, symmetric and 180°-tilt boundaries correspond to certain points in the boundary space. The distances δ_S and δ_I from a given boundary to the nearest symmetric and 180°-tilt boundaries, respectively, can be computed in a similar manner via numerical minimization as in the case of tilt and twist boundaries. This simple extension of the metric-based quantification of boundary characters has obviously the same drawbacks, namely, it is computationally inefficient. Since symmetric and 180°-tilt boundaries are specific twist and tilt boundaries, respectively, the question now arises how to modify the parameters α_N and α_L to obtain new parameters which could replace the distances δ_S and δ_I, respectively.

5.2.1 Parameters α_S and α_I as substitutes of the distances

Let us define $\alpha_S = \min\{[\alpha^2+(180^\circ-\omega)^2]^{1/2}\}$ and $\alpha_I = \min\{[(90^\circ-\alpha)^2+(180^\circ-\omega)^2]^{1/2}\}$; as in the case of α_N and α_L, the minimization is over all boundary representations. These parameters combine the terms allowing for recognizing near-twist and near-tilt characters of boundary representations, respectively, and the terms describing how big are the differences of the misorientation angles from 180°. Similarly to α_N and α_L, α_S and α_I are affected by neither inversion nor grain exchange symmetries.

To confirm that α_S and α_I can replace the distances δ_S and δ_I providing similar results, pairs $\{\delta_S, \alpha_S\}$ and $\{\delta_I, \alpha_I\}$ have been computed for 10^6 random grain boundaries for the cubic symmetry case. The correlations between α_S and δ_S, and between α_I and δ_I are very strong; they are illustrated in Fig. 5.7. Based on numerical experiments, the maximum relative difference between α_S and δ_S (α_I and δ_I) is 0.4% (33.3%), while the average deviation is 0.08% (5.7%). It is observed that α_I are generally slightly lower than δ_I. The corresponding PDFs for α_S and α_I are compared with the analogous functions for δ_S and δ_I

in Fig. 5.8. The distribution for α_S is practically identical to that for δ_S. In the case of α_I and δ_I, the widths of the PDFs are similar, whereas the mean value of α_I (12.9°) is slightly shifted toward lower values compared to the mean of δ_I (13.6°). According to the above results, the distances to the nearest symmetric and 180°-tilt boundaries can be approximated by α_S and α_I, respectively, and a given boundary will be classified as symmetric (180°-tilt) if α_S (α_I) is below an assumed limit.

5.2.2 Example: symmetric and 180°-tilt boundaries in Small IN100

The above random distribution functions will be used as a point of reference in analysis of Small IN100 data. These results complete those of the previous section with the analysis of symmetric and 180°-tilt characters of boundaries in that data set; this time, however, no mesh simplifications were performed.

In the studied material, a significant fraction of all boundaries are Σ3 coherent twin boundaries with (111) boundary planes. The twin boundaries are simultaneously symmetric and 180°-tilt, hence, in the experimental distributions, elevated values (compared to those for random boundaries) are expected for α_S and α_I close to zero.

As earlier, to make it easier to determine whether boundaries of small α_S are over- or under-represented in the alloy, the experimental distribution of α_S is also expressed as multiples of the random distribution, see Fig. 5.9a. Analogous distribution for α_I is shown in Fig. 5.9b. Indeed, the plots indicate that near-symmetric and near-180°-tilt boundaries are overrepresented: the values at $\alpha_S \approx 0$ and $\alpha_I \approx 0$ are 48 and 10.5 MRD, respectively. Since twin boundaries dominate in this microstructure, analogous distributions (Fig. 5.9) are computed for the subset of the data consisting only of boundaries whose misorientations deviate by more than 5° from the Σ3 misorientation (28.4% of all boundaries). With such a threshold, all near-twin boundaries are effectively removed. This allows for determination of the contribution of near-symmetric and near-180°-tilt boundaries other than those close to the twin boundary. The anisotropy observed in the data with Σ3 boundaries excluded is weaker than that in the complete data: the values at $\alpha_S \approx 0$ and $\alpha_I \approx 0$ are 1.5 and 1.6 MRD, respectively.

In the distributions of grain boundaries obtained for the investigated alloy (Fig. 2.4), apart from a very strong maximum at Σ3/(111) related to coherent twins, smaller peaks were observed at the Σ7/(111) and Σ9/(1$\bar{1}$4) boundaries, which both are 180°-tilt, and the latter is also symmetric. This makes it

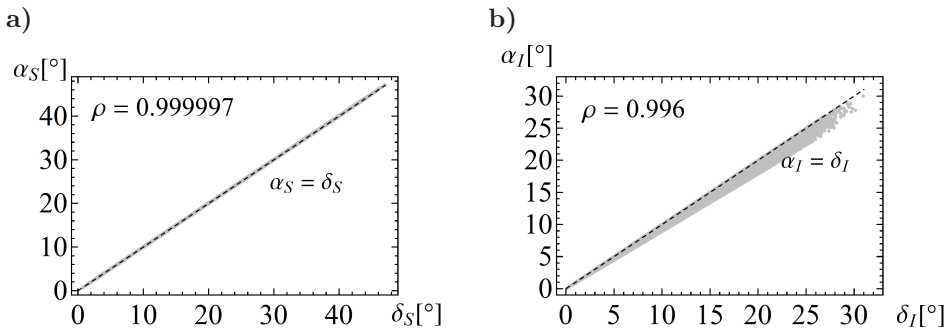

Figure 5.7: (a) Parameters α_S and distances δ_S to the nearest symmetric boundaries. (b) Parameters α_I and distances δ_I to the nearest 180°-tilt boundaries. Displayed data correspond to the cubic O_h symmetry case and were computed for 10^4 random boundaries. Symbols ρ denote the corresponding Spearman's rank correlation coefficients.

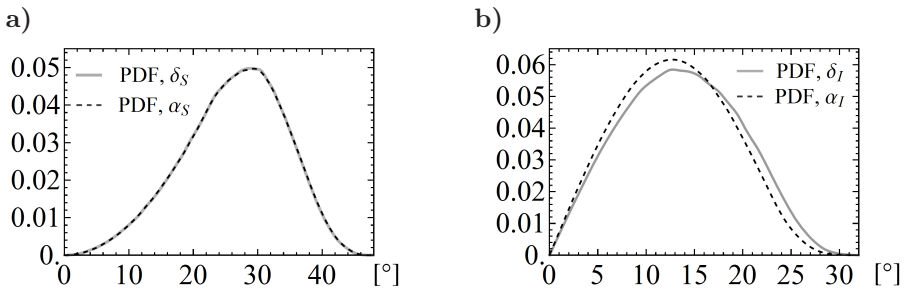

Figure 5.8: Probability density functions for *(a)* δ_S and α_S and *(b)* δ_I and α_I for the case of cubic O_h crystal symmetry.

sensible to ask about the percentage of high-coincidence boundaries among all symmetric and 180°-tilt boundaries. Therefore, the distributions of α_S and α_I were also computed for a subset which does not contain (assuming the threshold of 5°) low-Σ ($3 \leq \Sigma \leq 11$) and $\Sigma 27a$[11] CSL boundaries (32.1% of all boundaries). Clearly, the deviations of these distributions from the random data are decreased compared to the first subset: the values at $\alpha_S \approx 0$ and $\alpha_I \approx 0$ are 1.2 and 1.4 MRD, respectively (Fig. 5.9). It can be seen that near-symmetric and near-180°-tilt boundaries other than those with the low-Σ and $\Sigma 27a$ CSL misorientations are present in the boundary network.

The fractions of symmetric and 180°-tilt boundaries can be obtained by integrating PDFs, or can be read from the corresponding CDFs (not shown here). Assuming the limit for α_S and α_I of, say 8°[12], the fractions of symmetric and 180°-tilt boundaries among random grain boundaries are 1.4% and 21.9%, respectively (Fig. 5.8). In the Ni-based alloy, they are, respectively, 13.5% and 44.6% for the complete data set, 1.7% and 25.2% for the subset without $\Sigma 3$ boundaries, and 1.6% and 24.8% for the data with low-Σ and $\Sigma 27a$ CSL boundaries removed.

Besides the maxima at $\alpha_S \approx 0 \approx \alpha_I$, the distributions are relatively flat with values below 1 MRD for $\alpha_S > 15°$ and $\alpha_I > 7°$, respectively. These broad minima result from the normalization of probability: data above 1 MRD must be balanced by data below 1 MRD; if the peak height is decreased (like in the distributions for the subset without $\Sigma 3$ boundaries), then the minimum becomes shallow.

It is worth noting that with the parallel implementation, calculation of α_S and α_I for all 1.3×10^6 segments took about 3 minutes on a 4-core personal computer, whereas the calculation time for the distances δ_S and δ_I is about 52 hours.

5.2.3 Example: characteristic boundaries in Ferrite

The parameters α_S and α_I have also been used for studying boundary characters in Ferrite data set. As in the case of Small IN100 data, a segment was classified as a twist, symmetric, or 180°-tilt boundary if the approximate dis-

[11] $\Sigma 27a$ boundaries are excluded as they tend to occur at triple junctions where $\Sigma 3$ boundaries intersect $\Sigma 9$ boundaries.

[12] Since the resolution for grain misorientations is about 1°, this choice for the used metric is based mainly on the resolution for boundary plane parameters, e.g., Saylor et al. (2003a) estimated it to be "no better than 7.5°".

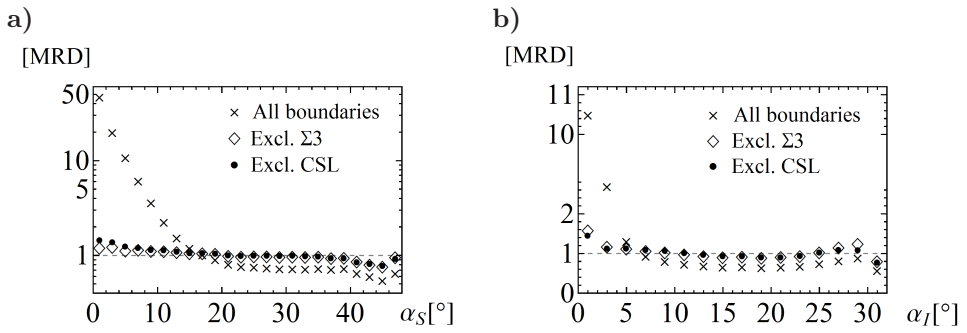

Figure 5.9: Distributions of α_S *(a)* and α_I *(b)* for Small IN100 data expressed as multiples of random distributions. The crosses correspond to the complete data set, disks to the data with $\Sigma 3$ boundaries excluded, and diamonds to the subset without low-Σ and $\Sigma 27a$ CSL boundaries. For computation of the experimental distributions, 2°-bins were used.

tances to the nearest twist, symmetric, and 180°-tilt boundary, respectively, calculated for that segment were below 8°. This limit reflects the experimental capabilities. We already know that with such resolution, tilt boundaries in materials with cubic O_h crystal symmetry are indistinguishable. The fractions of other special boundaries obtained for ferrite are compared to those calculated for random boundaries in Tab. 5.1. Only the percentages for symmetric boundaries and 180°-tilt boundaries differ significantly from those corresponding to the random data. From the distributions (Fig. 5.10) of the approximate distances α_S and α_I to the nearest symmetric boundaries and 180°-tilt boundaries, respectively, it follows that, indeed, near-symmetric boundaries (i.e., those with α_S close to zero) and near-180°-tilt boundaries (those with small α_I) are over-represented. It was reported by Beladi and Rohrer (2013b) that in the investigated steel, there is a high population of the $\Sigma 3/(\bar{2}11)$ – simultaneously symmetric and 180°-tilt – boundaries. Therefore, it is interesting to identify the largest subgroups of all symmetric boundaries and 180°-tilt boundaries. This is done based on the distributions of α_S and α_I, respectively, obtained for the complete data set and its subsets (Fig. 5.10). It is inferred that the contributions of near-$\Sigma 3$ boundaries to both symmetric and 180°-tilt boundaries are minor, while the dominant inputs are those of small-angle boundaries.

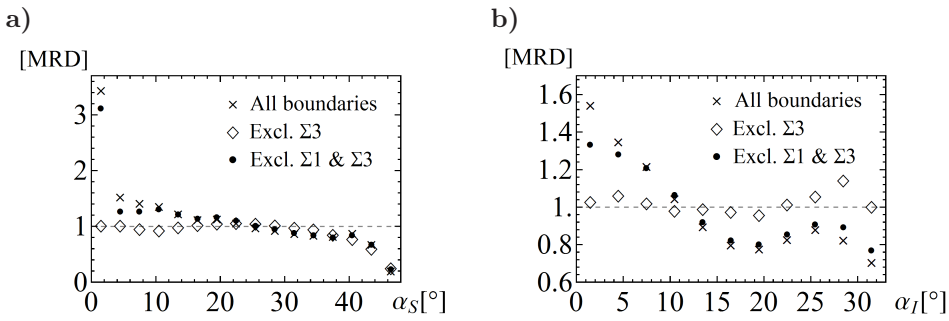

Figure 5.10: Distributions (in MRDs) of the approximate distances α_S and α_I to the nearest symmetric and 180°-tilt boundaries, respectively, computed for the data set of ferrite and its subsets. In the first subset, Σ3 boundaries (according to Brandon criterion) are excluded. The second subset does not contain Σ1 and Σ3 boundaries. (Σ1 boundaries have misorientation angles less than 15° and – due to data clean-up – greater than 5°.) The removed boundaries constitute 7.5% and 29.4% of the complete data, respectively.

Table 5.1: Area-weighted fractions (assuming the tolerance of 8°) of geometrically special boundaries in ferritic steel. Values in parentheses correspond to 10^7 random boundaries.

Twist	180°-tilt	Symmetric	180°-tilt & symmetric
21.2% (22.0%)	29.3% (21.9%)	2.2% (1.4%)	1.5% (0.7%)

5.3 Locations of characteristic points in the boundary space

Another issue related to boundaries of characteristic types is locating points in the boundary space which correspond to boundaries of these types. These points can be cataloged using two-dimensional diagrams containing stereographic projections of boundary plane normals corresponding to all tilt, twist, symmetric, and 180°-tilt boundaries with a given misorientation; cf. Sec. 2.3.4. The diagrams in this form can be directly linked to sections through functions of the five macroscopic boundary parameters for fixed misorientations and varying boundary planes (such sections are commonly used for representing these functions). Therefore, the diagrams may serve as patterns helpful in interpretation of the functions. Below, two complementary methods for obtaining the diagrams are described: analytical and numerical. The first approach allows for immediate determination of exact locations of boundaries of characteristic geometry. However, in practice, experimental errors need to be taken into account. The second method provides all boundaries that satisfy type-defining conditions with assumed tolerance thresholds; it is analogous to that used by Morawiec (2011), but computationally expensive distances to the nearest characteristic boundaries are replaced by their easy-to-calculate approximations that were defined in the previous sections. Morawiec (2011) considered only tilt and twist boundaries. Here, symmetric and 180°-tilt boundaries are also included in the catalogs.

5.3.1 Analytical method

The simplest algorithm for finding all boundaries of characteristic geometry is based on analytical derivations. First, one applies symmetry transformations C_1 and C_2 to a fixed misorientation M to get its equivalent representations M'. Then, based on the type definitions, all planes of characteristic boundaries can be determined from the corresponding misorientation axes. Finally, by transforming the indices of these planes to the initial reference frame using inverse transformations C_1^{-1} and C_2^{-1} one obtains the boundary normals to be included in a diagram. These operations are conveniently carried out using the matrix-vector formalism; M, M' denote the adequate misorientation matrices, the inverse transformations to the proper rotations C_1 and C_2 are represented by the transposed matrices C_1^T and C_2^T, respectively; cf. Sec 2.1.2.

For instance, application of the transformations

$$C_1 = \begin{bmatrix} -1 & 0 & 0 \\ 0 & 0 & -1 \\ 0 & -1 & 0 \end{bmatrix} \tag{5.3}$$

representing the rotation by 180° about the $[01\bar{1}]$ axis and C_2 equal to identity to the 38.9°/[111] ($\Sigma 7$) misorientation matrix

$$M = \frac{1}{7}\begin{bmatrix} 6 & -2 & 3 \\ 3 & 6 & -2 \\ -2 & 3 & 6 \end{bmatrix} \tag{5.4}$$

gives

$$M' = \frac{1}{7}\begin{bmatrix} -6 & 2 & -3 \\ 2 & -3 & -6 \\ -3 & -6 & 2 \end{bmatrix} \tag{5.5}$$

representing the rotation by 180° about $/[12\bar{3}]$. For this equivalent misorientation, boundaries with the planes $(12\bar{3})$ and $(\bar{1}\bar{2}3)$ have explicit twist characters and there is a zone of planes parallel to the misorientation axis, i.e., corresponding explicitly to tilts. Since the equivalent misorientation is a half-turn, these twist and tilt boundaries are also symmetric and 180°-tilt boundaries, respectively. The indices of these planes need to be transformed to the initial reference frame, e.g., the $(\bar{1}\bar{2}3)$ plane is represented by the unit vector $\mathbf{m}'_1 = 1/\sqrt{14}\,[\ -1\quad -2\quad 3\ ]^T$; its components in the initial reference frame are given by $\mathbf{m}_1 = C_1^T\mathbf{m}'_1 = 1/\sqrt{14}\,[\ 1\quad -3\quad 2\ ]^T$. Hence, indices of the plane in the initial frame are $(1\bar{3}2)$. Proceeding in an analogous manner with all possible transformations C_1 and C_2 (and thus, with all misorientation representations) one finds all boundaries of characteristic geometry.

5.3.2 Numerical searches

Measured boundary parameters are affected by experimental errors. Hence, it is difficult to match the measured parameters to the definitions of characteristic boundary types. Therefore, relying on patterns containing only exact locations of the boundaries of characteristic geometry (without any tolerance) may be, in some cases, insufficient for interpretation of the boundary distributions.

With error-affected data, it is more suitable to identify boundary types using metric functions defined in the boundary space. The distributions of these

distances for fixed misorientations and varying boundary planes (displayed as two-dimensional contour graphs like those in Sec. 2.2 and 5.1.2) may also serve as similar patterns useful in analyses of grain-boundary distributions. The patterns of this kind have the advantage in taking into account experimental uncertainties: the zero values clearly correspond to pure-twist, pure-tilt or pure-symmetric boundaries, and the isolines corresponding to assumed tolerance thresholds surround all near-twist, near-tilt or near-symmetric boundaries of given misorientations.

To obtain detailed diagrams for fixed misorientations, the values of the distances need to be probed at densely distributed boundary normals. Since calculation of the distances involves complex numerical algorithms, the distances are substituted by the parameters α_N, α_L, α_S, and α_I. The times needed for computing the approximated maps are about three orders of magnitude shorter than those for the maps with the accurate distances.

5.3.3 Example: CSL misorientations for the O_h symmetry

Most of the grain-boundary distributions obtained so far for materials of the cubic O_h symmetry were presented in the form of sections for CSL misorientations. Since only a few distributions were computed for non-cubic symmetries, having a catalog of charcteristic boundaries for a range of CSL misorientations would allow for interpretation of the majority of boundary distributions which can be found in the literature. Such an atlas with diagrams containing tilt, twist, symmetric, and 180°-tilt boundaries for CSL misorintations with $3 \geq \Sigma \geq 31$, and $\Sigma 39a$ can be found in Appx. B. In these maps, twist boundaries and zones of tilt boundaries are represented by, respectively, points and lines. Symmetric boundaries being particular twist boundaries have less degrees of freedom, and in consequence, they occur less frequently than twists; similarly, 180°-tilts are less frequent than tilts (cf. Glowinski, 2013). E.g., for the $\Sigma 7$ misorientation (see Fig. B.2), among eight distinct twist boundaries and the eight corresponding tilt zones, there is only one distinct symmetric boundary and three 180°-tilt zones.

Using the diagrams, one can identify boundaries with 'the most characteristic' geometries. By this we mean boundaries lying at the intersections of multiple tilt zones, e.g., $\Sigma 5/(512)$ boundaries (see also Fig. 6.6b), $\Sigma 9/(\bar{1}15)$ boundaries (Fig. 6.2c), and boundaries classified to more than one type at the same time, e.g., $\Sigma 11/(1\bar{1}3)$ (Fig. 6.4c). Boundaries being simultaneously of more than one type or being two-dimensionally periodic multiple tilts may

also have special physical properties. The diagrams shown in Fig. B.2 will be directly used to characterize the extrema occurring in the experimental distributions of boundaries appearing in the next chapter.

Depending on the misorientation, the diagrams may exhibit some symmetries (Morawiec, 1998; Patala and Schuh, 2013), and not all of the identified characteristic boundaries correspond to macroscopically different configurations. There are groups of twist and tilt boundaries whose planes belong to the same plane families. The symmetries in the boundary-plane distributions for a given misorientation follow from analysis of equivalent boundary representations; see Sec. 2.3.5.

5.3.4 Example: WC/WC boundaries in WC-Co composites

Differently than in the cubic case, for the hexagonal D_{6h} symmetry, the diagrams depend on lattice parameters. Example charts computed using the numerical approach, that is, the distributions of the approximate distances to the nearest characteristic boundaries for $c/a = \sqrt{20/21}$ and for the $90°/[10\bar{1}0]$ and $30°/[0001]$ misorientations are plotted in Figs. 5.11 and 5.12. For a given tolerance threshold, near-twist and near-tilt boundaries are represented by spots and bands, respectively. The figures are compared to the sections through experimental distribution of WC/WC grain boundaries in WC-Co composites presented by Kim et al. (2008).

To demonstrate a possible scheme of interpretation of grain-boundary distributions using numerically obtained patterns, the peaks of the distribution of WC/WC boundaries in WC-Co composites will be characterized. Let us consider each of the three sections through the distribution shown by Kim et al. (2008).

- The section for the $90°/[10\bar{1}0]$ misorientation (see Fig. 5.11) contains two strong peaks at the $(10\bar{1}0)$ and $(\bar{1}010)$ poles. These are directly related to pure-twist boundaries. With our maps, these two configurations are also recognized as double 180°-tilts. The distances of the peaks to symmetric boundaries are very large.

- In the case of the $30°/[0001]$ misorientation (see Fig. 5.12), there is a maximum for the (0001) plane. These are twist boundaries. The (0001) plane is also located at the intersection of six 180°-tilt zones. Elevated values of the distribution occurred also at the prismatic positions $(10\bar{1}0)$,

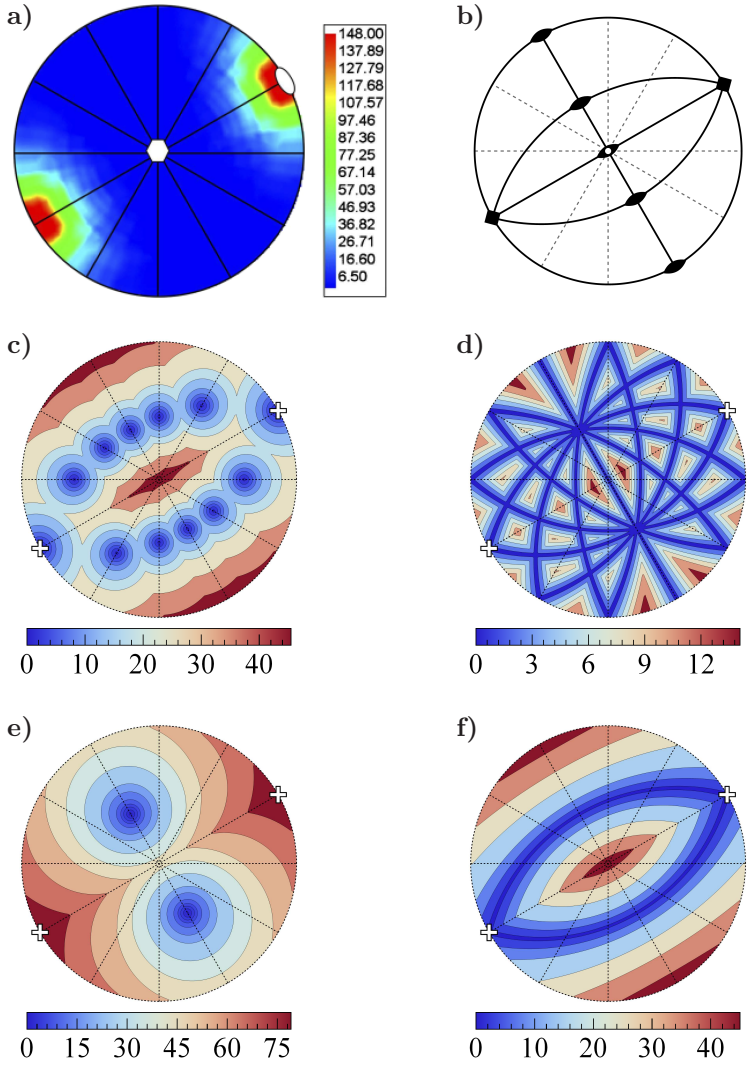

Figure 5.11: Experimental distribution of planes of WC/WC boundaries for the $90°/[10\bar{1}0]$ misorientation *(a)* reprinted from Kim et al. (2008), with permission from John Wiley & Sons; its symmetries are shown in *(b)*. The corresponding distributions (for $c/a = \sqrt{20/21}$) of the approximate distances (in degrees) to the nearest twist *(c)*, tilt *(d)*, symmetric *(e)*, and 180°-tilt *(f)* boundaries. The distributions are given as functions of boundary plane normals and plotted on stereographic projections. Locations of the peaks visible in *(a)* are marked in *(c-f)* with crosses.

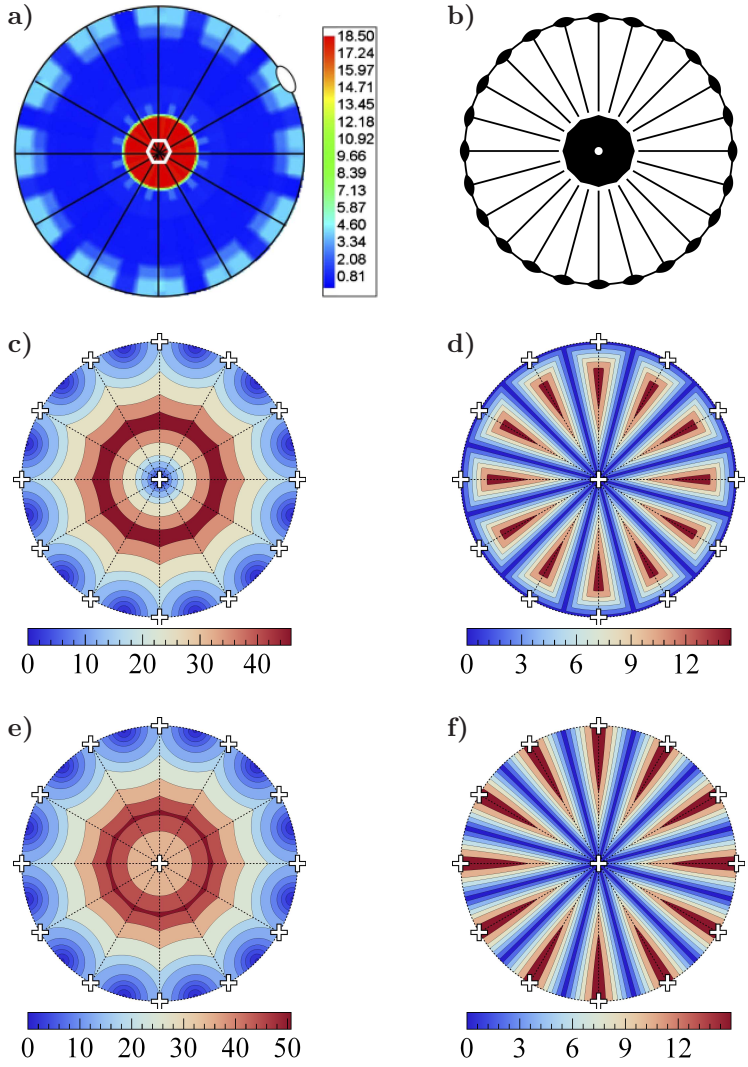

Figure 5.12: Section through the experimental distribution of WC/WC boundaries for the 30°/[0001] misorientation *(a)* reprinted from Kim et al. (2008), with permission from John Wiley & Sons; its symmetries are shown in *(b)*. The related distributions (for $c/a = \sqrt{20/21}$) of the approximate distances (in degrees) to the nearest twist *(c)*, tilt *(d)*, symmetric *(e)* and 180°-tilt *(f)* boundaries. The distributions are given as functions of boundary planes and are displayed on stereographic projections. Locations of the peaks visible in *(a)* are marked in *(c-f)* with crosses.

Table 5.2: Characterization of the peaks in the distribution of WC/WC boundaries in a WC-Co composite. The parameters and heights of the peaks (expressed as multiples of random distribution) are cited after Kim et al. (2008). Peaks identified as corresponding to a given boundary type are marked by the symbol "•". For peaks located at the intersections of tilt zones, the numbers of zones are added in parentheses.

misorientation	plane	MRDs	twist	tilt	symmetric	180°-tilt
90°/[10$\bar{1}$0]	(10$\bar{1}$0)	148	•	•(2)	–	•(2)
30°/[0001]	(0001)	18	•	•(6)	–	•(6)
	(10$\bar{1}$0), (11$\bar{2}$0)	5	–	•	–	–
90°/[$\bar{2}$110]	(0001)	8	–	•	–	–
	(1$\bar{1}$00)	8	–	•(2)	–	–

(11$\bar{2}$0). These are tilts, but they are neither twist nor symmetric nor 180°-tilt boundaries.

- In the distribution of boundary planes for the 90°/[$\bar{2}$110] misorientation, there are peaks at the (0001), (1$\bar{1}$00) and ($\bar{1}$100) poles. The distributions of the distances corresponding to this misorientation are almost identical to those for the 90°/[10$\bar{1}$0] misorientation with the only difference that they are rotated clockwise by 30° (therefore, only the latter are shown). The peak for the (0001) plane corresponds to a boundary with a single tilt axis. The other two maxima lie on the intersections of two tilt zones.

All of these over-represented boundaries have at least one tilt axis. Interestingly none of them can be classified as symmetric. The two highest peaks are interpreted as twist boundaries located at the intersections of 180°-tilt zones. The interpretations of all the maxima are collected in Table 5.2.

Chapter 6

New approach to computation of boundary distributions

In this chapter, an alternative method for computing grain boundary distributions with respect to the five macroscopic parameters is presented. It is shown that abandoning bins in favor of kernel density estimation leads to significant improvement of the quality of resulting distributions. The new method also allows for a direct estimation of the reliability of the distributions. Diverse examples of practical applications of the new solution are provided. KDE is also adapted to calculation of boundary plane distributions independent of misorientations in both crystallite and laboratory reference frames.

6.1 Use of kernel density estimation

To avoid artifacts caused by the currently used computation method, it is proposed to utilize the kernel density estimation technique and to replace the partition of the boundary space into bins by probing the distributions at selected points and summing areas of boundaries that fall within specified distances from these points. Formally, the boundary space is a Cartesian product of misorientation and boundary plane subspaces. For calculation of distributions of boundary planes for fixed misorientations, it is convenient to consider distances in these subspaces separately. Having separate limiting radii for misorientations (ρ_m) and for boundary planes (ρ_p) allows for adjusting the bin shapes to actual experimental resolutions of measured boundary parameters. This option would not be available if a single distance defined in the complete boundary space was used.

To obtain a section through a distribution for a fixed misorientation, all

boundary segments whose distances δ_m from that misorientation are smaller than ρ_m (i.e., segments that fall into the 'ball' of radius ρ_m centered at the fixed misorientation) are first identified. Then, the distribution is calculated at evenly dispersed directions. Areas of the identified segments whose normals are located at distances δ_p not larger than ρ_p from a given direction (i.e., that fall into the ball of radius ρ_p in the boundary-plane subspace) are accumulated. The idea of probing the distribution is illustrated schematically in Fig. 6.1a. In the end, values ascribed to the bins are expressed as multiples of the random distribution: the values obtained from experimental data and normalized with respect to the total area of boundaries are divided by the corresponding normalized values obtained from large sets of random boundaries. These sets were generated assuming that probabilities of occurrence of all misorientations are equal, and that for each misorientation, all boundary inclinations are also equally probable. In other words, the normalization coefficient is an inverse of volume of the ball restricted by given ρ_m and ρ_p obtained via Monte Carlo integration[13]. Clearly, with the new approach, the averaging over bins is eliminated, and the regions determined by ρ_m and ρ_p are 'spherical' (with respect to the used metrics) in the subspaces of misorientation and boundary planes. Thus, a ball in the boundary space is a Cartesian product of balls given in the misorientation and boundary-plane subspaces. Shapes of the product-balls are also quite regular in the complete space if ρ_p and ρ_m are similar.

The benefits of using the metric-based approach are demonstrated for the same test distribution containing $\Sigma5/(012)$ and $\Sigma3/(111)$ boundaries as considered in Sec. 2.6.2. The volume of 10°-bins of the partition is close to that of the distance-based bins when $\rho_m = 5^\circ = \rho_p$. With these radii, peaks in the $\Sigma3$ and $\Sigma5$ sections of the test distribution are contained in disks with radii equal to the assumed ρ_p (Fig. 6.1b). There is no spread along the [010] direction in the $\Sigma5$ section of the resulting distributions. The sections for the $50^\circ/[111]$ and $57^\circ/[110]$ misorientations are flat with the value of 0 at all poles.

The chosen limiting radii ρ_m and ρ_p, and hence, volume v of an individual bin, affect the uncertainties of the values of the distribution function. With f being a value of the distribution at a given point, the minimal number of measurements, N, required for the relative error defined as (standard deviation of f) / f to be smaller than certain ε is given by $N \approx c/(\varepsilon^2 v f)$, where c is a coefficient accommodating correlations in the data (van den Boogaart, 2002).

[13] One could consider normalization of distributions using texture-influenced data. However, at this stage, we would prefer to avoid additional complications.

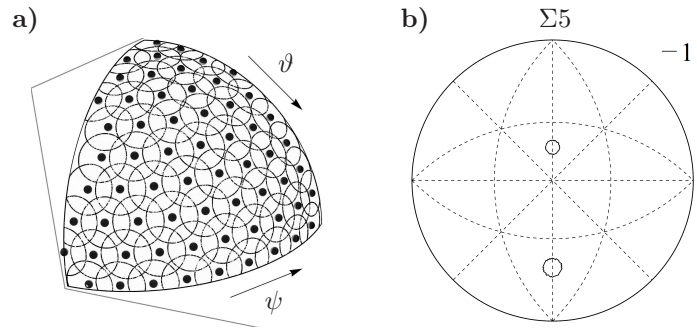

Figure 6.1: *(a)* Schematic presenting (two-dimensional) 'balls' centered at sampling points (in the subspace of boundary plane normals); each ball has the radii $\rho_p = 7°$. Here, only about 60 points, and corresponding balls, are visible. In practice, the points are much denser; all distributions in this work were sampled at about 4000 points on the hemisphere. *(b)* Σ5 section calculated using the KDE-based method with $\rho_m = 5° = \rho_p$ for the test distribution; to be compared with Fig. 2.9b.

With N being the number of distinct grain boundaries (*not* the number of segments in a reconstructed mesh), the data are only weakly correlated, and hence, $c \approx 1$ can be assumed. With this assumption, the above formula allows for a rough estimation of the relative error:

$$\varepsilon \approx (Nvf)^{-1/2}. \tag{6.1}$$

This simple equation will be used for evaluation of the distribution errors in further analyses.

As the first test, the KDE-based method was applied to Small IN100 data. Selection of optimal parameters ρ_m and ρ_p (so-called bandwidth) for the kernel density estimation technique is non-trivial. A number of values have been tested. The choice has an impact on the peak height and the errors. To keep the errors at bay, ρ_m and ρ_p must be sufficiently large. Since grain reconstruction process decreases the resolution for misorientations, it is reasonable to set the radius ρ_m at 3°. The resolution in the boundary-plane subspace was estimated using coherent twin boundaries; as the standard deviation of the Gaussian function approximating the shape of the (111) peak in the Σ3 section of the experimental distribution is close to 7°. This value was used as the limiting distance ρ_p. With such radii, the peaks are not excessively spread, while the errors stay at acceptable levels. Let us compare the sections for the Σ3, Σ7 and Σ9 misorientations calculated using the new approach (Fig. 6.2) to analogous sections obtained using the partition into 10°-bins (Fig. 2.4). The

large differences in nominal heights of the peaks obtained by the two methods come partly form the difference in volumes of the 10°-bins and the bins limited by $\rho_m = 3°$ and $\rho_p = 7°$. (The former are about 2 times larger than the latter.) Despite the smaller volume, the distribution obtained by the new approach appears to be smoother.

The distributions computed using both methods are also compared using one-dimensional sections of the distributions. Fig. 6.3a presents the distribution values at the (111) pole for misorientations about [111] axis versus the misorientation angle. The curve corresponding to the metric-based approach reveals more details than the piecewise flat graph obtained by the partition-based method. Fig. 6.3b shows the profiles of the distribution function along $[1\bar{1}0]$ direction for the $\Sigma 9$ misorientation. Both methods give a relatively strong peak at the $(1\bar{1}4)$ symmetric boundary (cf. Fig. B.2). The partition into 10°-bins leads to an artificial peak near the $(\bar{2}21)$ pole, which disappears when larger k is used; see, e.g., the green line in Fig. 6.3b. The maxima in the vicinity of the $(\bar{1}15)$ and $(1\bar{1}1)$ poles, clearly visible in the distribution obtained with the new approach are barely discernible in the distribution obtained by the partition-based method. It is worth noting that $(\bar{1}15)$ and $(1\bar{1}1)$ poles correspond to tilt boundaries having multiple tilt axes, and the $(\bar{1}15)$ and $(1\bar{1}1)$ planes expressed in the second grain are $(1\bar{1}\bar{1})$ and $(\bar{1}1\bar{5})$, respectively.

6.2 Five-parameter distributions for selected materials

6.2.1 Nickel (CMU)

Although Nickel (CMU) is a relatively small data set, it is a good proving ground for learning how to evaluate reliability of the obtained distributions. Moreover, Li et al. (2009) computed populations of boundaries for this sample using the partition-based method with "8.2°-bins" (i.e., with $k = 11 = k'$) and presented sections through the distribution for four misorientations: $\Sigma 3$, $\Sigma 5$, $\Sigma 7$, and $\Sigma 9$. This gives us another opportunity for comparing the hitherto used method with the new approach. For computing the distribution by KDE, the limiting radii were set to $\rho_m = 3°$ and $\rho_p = 7°$ as in the test with Small IN100 data. The same values for these radii will also be used for Nickel (UGent) and Big IN100 in order to allow for direct comparison of the distributions obtained for several nickel-based FCC metals. The sections through the distribution computed for Nickel (CMU) data set for CSL misorientations corresponding to Σ-values equal to 3, 5, 9, 11, and 27 are shown in Fig. 6.4. The corresponding

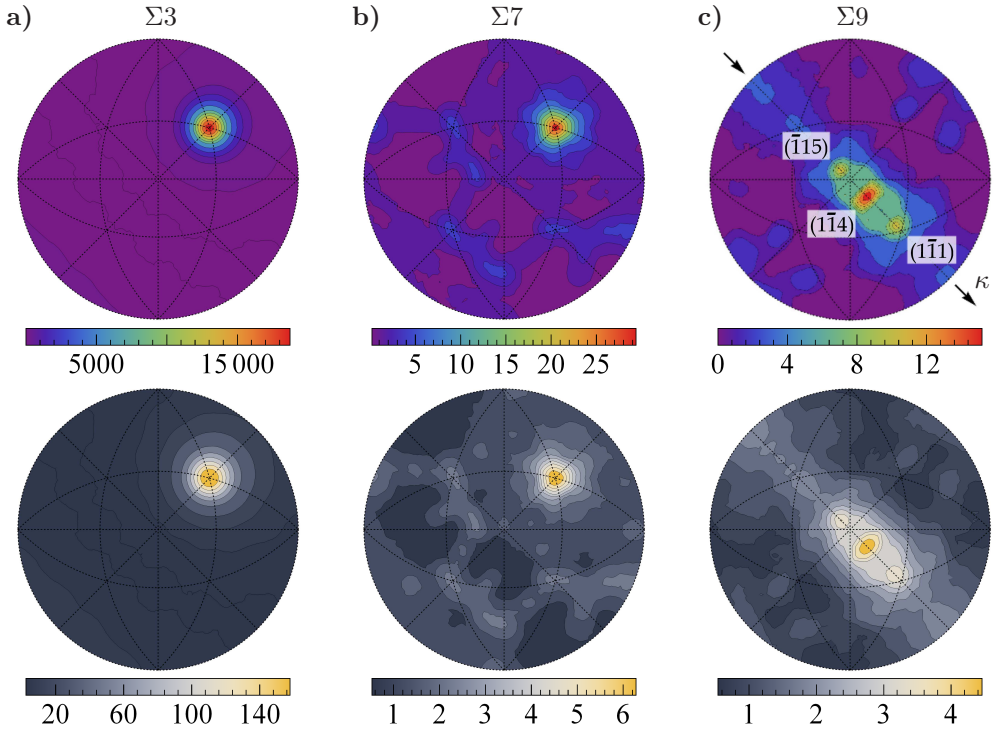

Figure 6.2: Σ3 *(a)*, Σ7 *(b)*, and Σ9 *(c)* sections through the distribution (given in MRDs) of grain boundaries computed for Small IN100 data using the KDE-based approach with $\rho_m = 3°$ and $\rho_p = 7°$. In each pair, the upper plot is the distribution, while the lower function represents the errors. To be compared with Fig. 2.4.

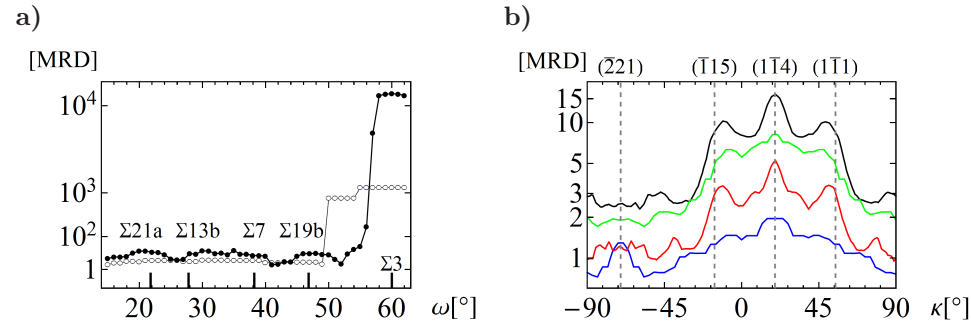

Figure 6.3: One-dimensional sections through distributions of grain boundaries for Small IN100. *(a)* Distribution values at the (111) pole for $\omega/[111]$ misorientations computed using the metric-based (disks) and partition-based (circles) methods. *(b)* Profiles along the $[1\bar{1}0]$ zone (marked by arrows in Fig. 6.2) for the Σ9 misorientation; cf. Fig. 7 of **?**. Black and red lines correspond to the metric-based approach with $\rho_m = 3°$, $\rho_p = 7°$ and $\rho_m = 5° = \rho_p$, respectively. Blue and green lines were obtained by the partition-based method using, respectively, $k = 9 = k'$ (i.e., 10°-bins) and additionally $k = 15$, $k' = 7$; in the latter case, volumes of the bins are close to those determined by $\rho_m = 3°$, $\rho_p = 7°$.

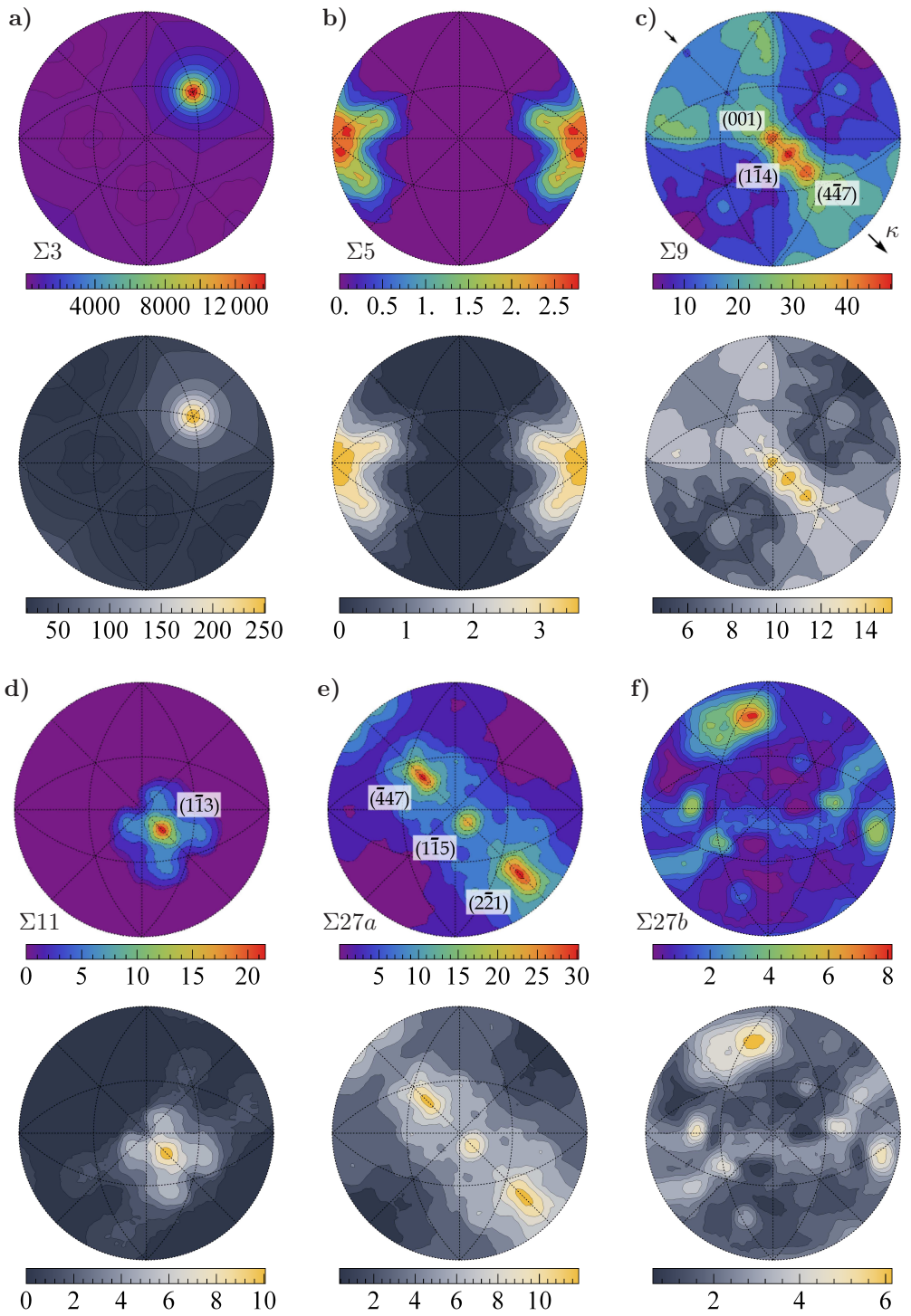

Figure 6.4: Sections for the *(a)* Σ3, *(b)* Σ5, *(c)* Σ9, *(d)* Σ11, *(e)* Σ27*a*, and *(f)* Σ27*b* misorientations through the distribution of grain boundaries computed for Nickel (CMU) data using the KDE-based approach with $\rho_m = 3°$ and $\rho_p = 7°$. In each pair, the upper plot is the distribution, while the bottom plot is the corresponding statistical error. Contours are given in MRDs.

statistical errors given by Eq.(6.1) are also presented.

The considered nickel sample contains a large fraction of coherent twin boundaries; 11.3% of boundaries are Σ3 boundaries (according to Brandon criterion) having their planes deviated by less than 10° from the (111) plane. This is confirmed by a strong maximum (13670 ± 250 MRD) at the (111) pole in the Σ3 section (Fig. 6.4a). A similar peak was observed by Li et al. (2009), though its nominal height (about 4500 MRD) was smaller than of that obtained using KDE. As explained before, due to different approaches to computation of the distribution functions, the large difference is not surprising.

The values of the distribution in the Σ5 and Σ7 sections obtained by Li et al. (2009) were in the ranges of 0.3 to 0.9 MRD and 0.57 to 0.81 MRD, respectively, which indicates that both Σ5 and Σ7 boundaries occur less frequently than it would be expected in the random case. The Σ5 section (Fig. 6.4b) and Σ7 section (not shown here) computed using KDE have visibly different shapes than those presented by Li et al. (2009). E.g., Li et al. (2009) did not see peaks at the (100) and $(\bar{1}00)$ poles in the Σ5 section which are apparent in the function obtained by KDE. However, the accompanying errors in the Σ5 and Σ7 sections exceed 100%. Therefore, there is no ground for drawing any conclusions on Σ5 and Σ7 boundaries in this nickel sample.

It is known (see, e.g., Gertsman, 2001, and references therein) that if two Σ3 boundaries intersect at the triple junction, then the third of the boundaries at this junction must be a Σ9 boundary. Similarly, if a Σ3 boundary intersects a Σ9 boundary, the third boundary is a Σ27 boundary. Large fraction of Σ3 boundaries – 37.2% according to Brandon criterion – may imply significant fractions of Σ9 and Σ27 boundaries; Σ3, Σ9, Σ27*a*, and Σ27*b* boundaries in Nickel (CMU) data are visualized in Fig. 4.2a. Populations of Σ9, Σ27*a*, and Σ27*b* boundaries as 2D functions of boundary planes are displayed in Fig. 6.4c, e, and f, respectively. To avoid overlap of the functions for the Σ9 and Σ27*a* misorientations (due to their closeness in the misorientation space), sufficiently small ρ_m for KDE must be chosen. With ρ_m at 3°, Σ9 and Σ27*a* boundaries are separated well enough. (This would not be possible using the 10°-bins (see Glowinski and Morawiec, 2015); with the 8.2°-bins, the overlap would be reduced, but the distribution would still be distorted by averaging over equivalent bins.) Like for Small IN100, in the Σ9 section, there occurs a peak at the $(1\bar{1}4)$ pole coinciding with symmetric configuration. Its height is 48 ± 15 MRD. Moreover, there are maxima for the (001) and $(4\bar{4}7)$ planes; they are 44 ± 14 MRD high. From the analysis of symmetries of boundary

distributions (Fig. B.1), it turns out that these two maxima are related to the same physical tilt boundaries: Σ9 boundaries which have the (001) and $(4\bar{4}7)$ planes in the first grain, have the $(4\bar{4}\bar{7})$ and $(00\bar{1})$ planes in the second grain, respectively. Interestingly, two similar peaks were also observed in the case of Small IN100 data, but those peaks were shifted toward the $(\bar{1}15)$ and $(1\bar{1}1)$ poles, respectively. In the Σ27*a* section, there is a maximum for the $(1\bar{1}5)$ plane with the height of 23 ± 10 MRD; Σ27*a* boundary with this plane is a symmetric boundary. Besides this maximum, there are two symmetrically equivalent peaks at the $(2\bar{2}1)$ and $(\bar{4}47)$ poles; the heights of these peaks are 29 ± 12 MRD. Furthermore, these poles coincide with intersections of three tilt zones.

There appears only one maximum in the Σ27*b* section. Its height (8 MRD) is relatively small and only slightly greater than the error (±6 MRD). Moreover, the maximum is significantly spread which makes it is difficult to determine the pole at which this peak is actually located. Finally, there is a peak with the height of 21 ± 10 MRD at the $(1\bar{1}3)$ in the Σ11 section (Fig. 6.4d). This is the position of boundaries of symmetric geometry.

6.2.2 Nickel (UGent)

Nickel (UGent) is the smallest of the data sets studied in this work. Such a poor statistics makes the data quite difficult to analyze. Nevertheless, we still may gain some knowledge from the corresponding boundary distribution. In particular, Nickel (CMU) and Nickel (UGent) data sets were both acquired from recrystallized nickel samples; since these samples were processed using different routes and in effect their average grain sizes differ by two orders of magnitude. Besides that, Nickel (UGent) has a bimodal grain size distribution. It is interesting to see if this difference has an impact on distributions of grain boundaries. Due to the small number of boundaries collected in Nickel (UGent) set, vast parts of the corresponding boundary distribution will have very large uncertainties. A few sections through this distribution containing the highest maxima with errors at reasonable levels are plotted in Fig. 6.5; these sections were obtained using the KDE-based method.

Similarly to Nickel (CMU), also in Nickel (UGent) data, there is a strong peak at the (111) plane in the Σ3 section (i.e., at the coherent twin boundary). Its height, 4276 ± 248 MRD, is however, smaller than that of the maximum occurring for Nickel (CMU) (Fig. 6.5a). This reflects the fraction of coherent twin boundaries: in Nickel (UGent) set, only 4.1% of boundaries have the Σ3

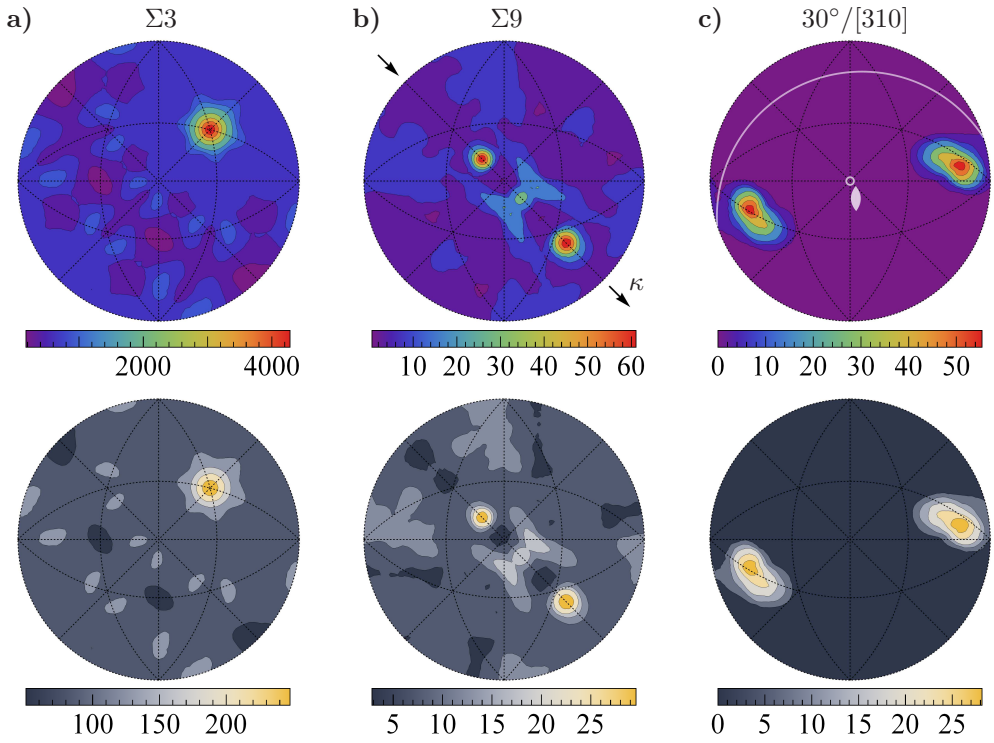

Figure 6.5: Sections for the *(a)* Σ3, *(b)* Σ9, and *(c)* 30°/[310] misorientations through the distribution of grain boundaries computed for Nickel (UGent) data set by means of kernel density estimation with ρ_m and ρ_p at 3° and 7°, respectively. In each pair, the upper plot is the distribution, while the bottom plot is the corresponding statistical error. Values of the functions are expressed in MRDs.

misorientation (according to Brandon criterion) and (111) plane (with the tolerance of 10°) which is significantly less than in Nickel (CMU), though there are more (46.8%) general Σ3 boundaries (of arbitrary planes) in Nickel (UGent).

As in the cases of Small IN100 and Nickel (CMU) data, three peaks appear in the Σ9 section obtained for Nickel (UGent) (Fig. 6.5b). There is a maximum at the symmetric $\Sigma 9/(1\bar{1}4)$ boundary; its height is 26 ± 19 MRD. Besides it, two equivalent peaks with the heights of 61 ± 29 MRD lie on the [110] zone. These two peaks are located close to the $(\bar{1}15)$ and $(1\bar{1}1)$ poles, but their positions do not match exactly the analogous peaks visible for Small IN100 and Nickel (CMU). When analyzing small data sets, it is essential to verify whether multiple boundaries contribute to a given maximum or if a peak reflects one, large enough, boundary. From visualization shown in Fig. 4.2b, it is clear that the features in the Σ9 section have their origins in multiple boundaries. On the

other hand, a peak appearing in the section for the 30°/[310] misorientation whose height is close to the peaks in the Σ9 section (Fig. 6.5c) comes from a single boundary of a relatively big area.

Such visualization may also be useful for answering the question addressed by Li et al. (2009) if Σ9 boundaries have low energies and are, therefore, over-represented (in nickel), or if they occur that frequently because of large fraction of intersecting Σ3 boundaries. It can be seen that, in the Small CMU and Nickel (UGent) boundary networks (Fig. 4.2), there are no Σ9 boundaries isolated from Σ3 boundaries. The same applies to Small and Big IN100 data sets.

6.2.3 Big IN100

The next data set, Big IN100, is the largest one. Since these data were acquired from the same material as Small IN100, and in both samples, the fractions of near-twin boundaries have been checked to be almost identical, we expect consistent heights of the peaks at Σ3/(111) for both data sets. Indeed, the heights of this peak are 18620 ± 80 MRD and 18690 ± 160 MRD for Big IN100 and Small IN100, respectively.

Differently than for the previous data sets, owing to large statistics of Big IN100, it is possible to analyze the populations of Σ5 boundaries (Fig. 6.6a). There are elevated values in the vicinity of the (512) pole (and symmetrically equivalent locations, see Fig. B.1); the distribution value at (512) is 3.6 ± 1.0 MRD. Besides that, about 20 distinct boundaries contribute to this maximum and Σ5/(512) boundaries are categorized as multiple-tilt boundaries (see Fig. B.2).

In the section for the Σ9 misorientation, there are two peaks in the vicinities of $(1\bar{1}1)$ and $(\bar{1}15)$; the same peaks were observed for Small IN100, though their heights for Big IN100 (5.6 ± 1.4 MRD) are smaller. Analogously to all Ni-based samples, elevated values (6.4 ± 1.4 MRD) are observed around $(1\bar{1}4)$. This time, however, the maximum does not look like a single peak, but rather like a sum of three overlapping peaks. Besides that, elevated values at the level of about 3 ± 1 MRD are observed along the whole [110] zone. This was not observed for the previous data. Comparison of one-dimensional profiles along this zone $[1\bar{1}0]$ for four data sets are presented in Fig. 6.7a.

In the Σ11 section, similarly to Nickel (CMU), there is a maximum with the height of 31 ± 3 MRD located at the $(1\bar{1}3)$ pole, i.e., at the symmetric multiple-tilt boundary.

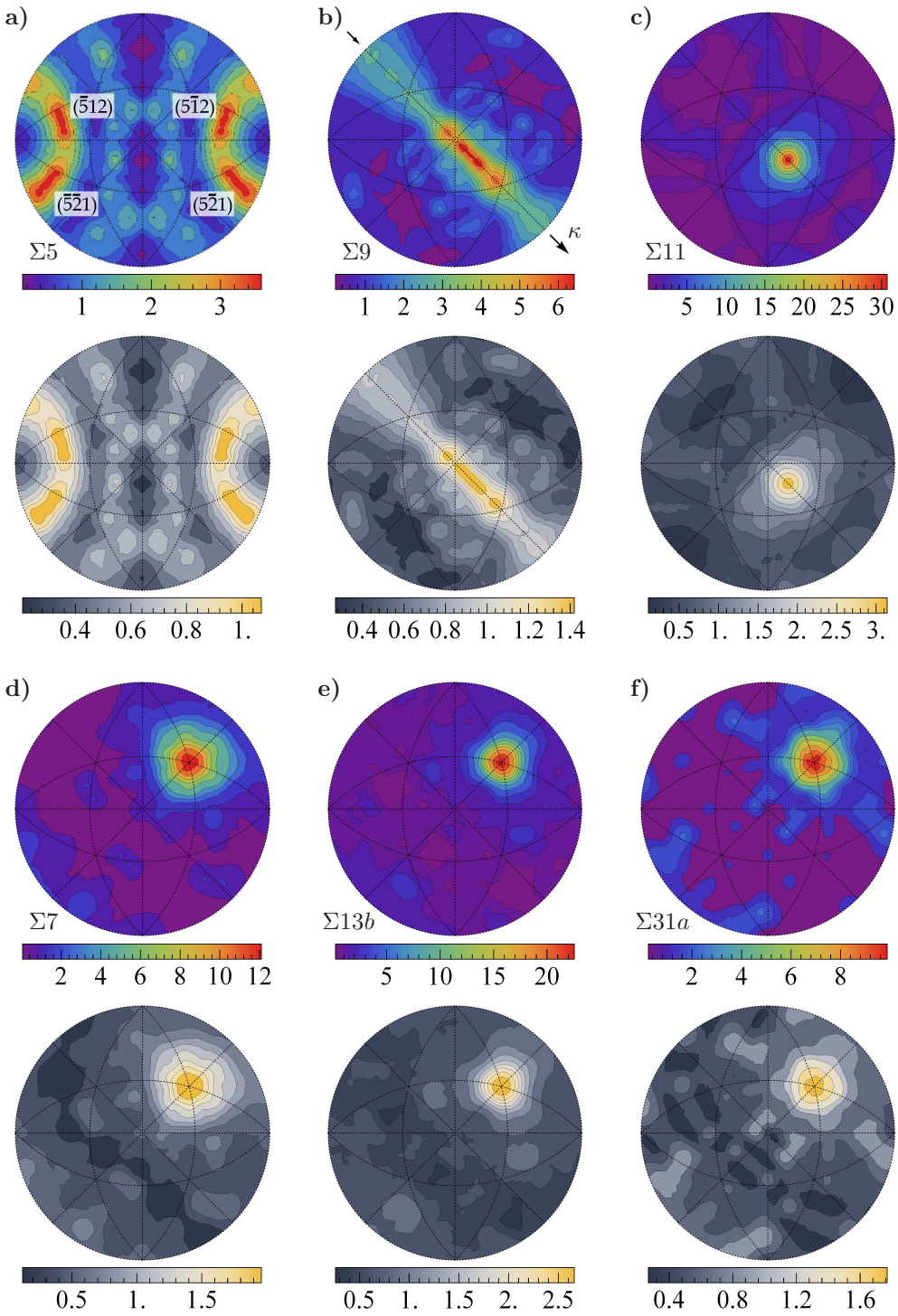

Figure 6.6: Sections for the *(a)* Σ5, *(b)* Σ9, *(c)* Σ11, *(d)* Σ7, *(e)* Σ13*b*, and *(f)* Σ31*a* misorientations through the distribution of grain boundaries computed for Big IN100 data using KDE with $\rho_m = 3°$ and $\rho_p = 7°$. In each pair, the upper plot is the distribution, while the bottom plot is the error. Contours are given as MRDs.

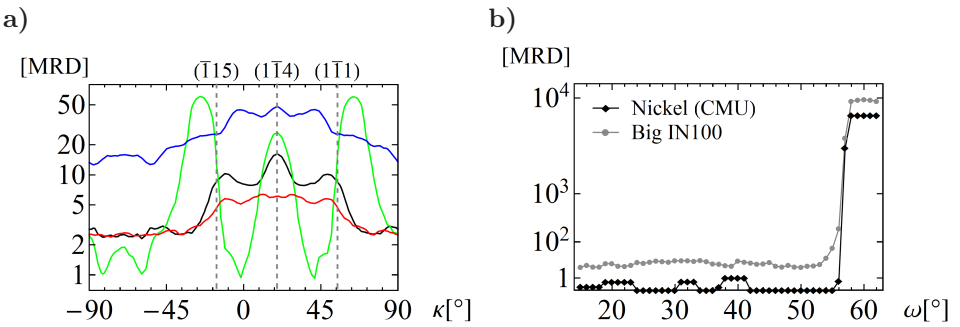

Figure 6.7: *(a)* Profiles along the $[1\bar{1}0]$ zone (marked by arrows in Fig. 6.2c, 6.4c, 6.5b, and 6.6b) for the $\Sigma 9$ misorientation for four Ni-based metals: Nickel (CMU) (blue), Nickel (UGent) (green), Small IN100 (black), and Big IN100 (red). *(b)* Distributions at the (111) pole for $\omega/[111]$ misorientations computed for Big IN100 (gray) and Nickel (CMU) (black).

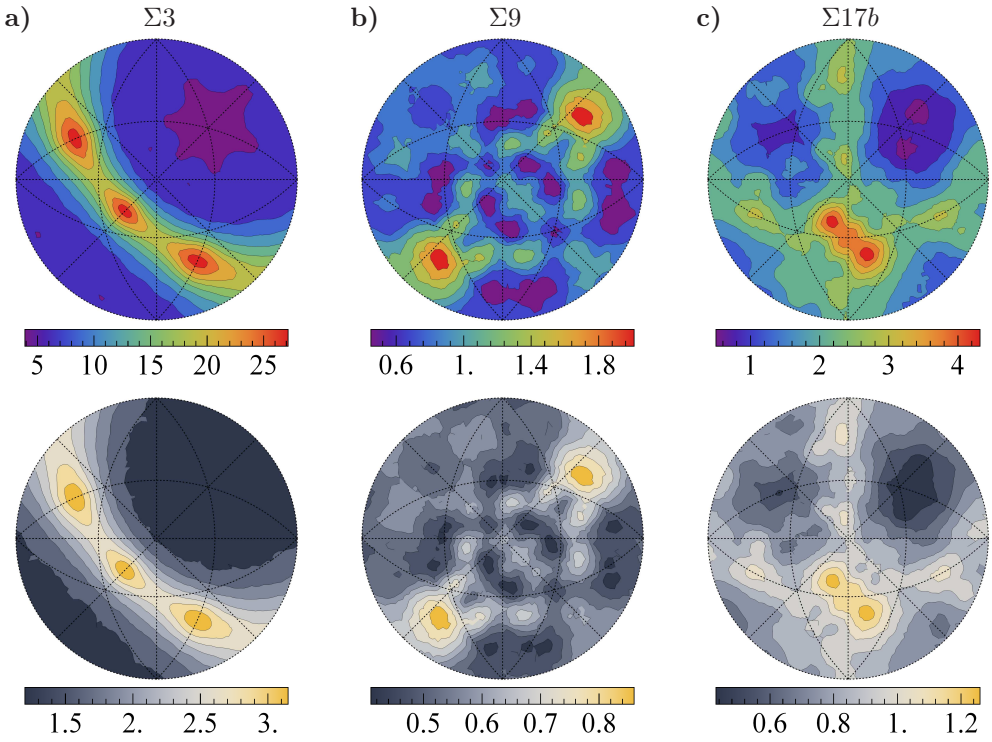

Figure 6.8: Sections for the *(a)* $\Sigma 3$, *(b)* $\Sigma 9$, and *(c)* $\Sigma 17b$ misorientations through the distribution of grain boundaries computed for Ferrite using the KDE-based approach with $\rho_m = 5°$ and $\rho_p = 8°$. In each pair, the upper plot is the distribution, while the bottom plot is the corresponding statistical error. Contours are given in multiples of random distributions.

In the $\Sigma 7$ section, there is a peak for the (111) plane, similar to that in the case of Small IN100 data; however, its height (12 ± 2 MRD) is different. There are also peaks for other misorientations about the [111] axis, e.g., for the $\Sigma 13b$ (23 ± 3 MRD), $\Sigma 21a$ (11 ± 2 MRD), and $\Sigma 31a$ (10 ± 2 MRD) misorientations. Elevated values at these points were also seen also for Small IN100, see Fig. 6.3a. The heights of the peaks at the (111) for Big IN100 are compared with those for Nickel (CMU) in Fig. 6.7b.

6.2.4 Ferrite

Grain boundary distributions for Ferrite were studied by Beladi and Rohrer (2013b). The distribution was computed using partition into 10°-bins and sections through that distribution for various CSL misorientations with the [100], [110], and [111] misorientation axes were studied. This, again, gives us reference results which can be confronted with results obtained by the KDE-based method. Maxima in the boundary distribution for BCC ferrite appear to be much weaker than those occurring for FCC metals. Therefore, to keep the errors at a low level, the limiting radii ρ_m and ρ_p were set to 5° and 8°, respectively.

In the $\Sigma 3$ section, there are three equivalent maxima located at the $(\bar{2}11)$, $(\bar{1}\bar{1}2)$, and $(1\bar{2}1)$ poles. They correspond to boundaries being symmetric and 180°-tilt boundaries at the same time. The general shape of the distribution function is consistent with that obtained using the partition into bins, though, again, heights of the peaks are different. Interestingly, for KDE, the peaks are higher (27 ± 3 compared to 13 MRD) although the volume of the balls determined by $\rho_m = 5°$ $\rho_p = 8°$ is about 2.5 times larger than that of the 10°-bins. This shows how the averaging of the distibution over equivalent bins in the partition-based method flattens the features of distributions.

In the $\Sigma 9$ section, Beladi and Rohrer (2013b) observed relatively low (about 2.1 MRD) maxima in the neighborhoods of the (110) and $(\bar{1}\bar{1}0)$ poles. However, they also observed that "the energy distribution did not have an obvious inverse correlation with the populations for the $\Sigma 9$ boundary". In the $\Sigma 9$ section computed using KDE, indeed, there are some elevated values, though they are quite far from the (110) and $(\bar{1}\bar{1}0)$ poles. Moreover, the corresponding error is very large, so it is difficult to judge if these are true peaks or artifacts.

Elevated values are observed also in the $\Sigma 17b$ section in the neighborhood of the $(0\bar{1}1)$ pole with values up to 4.3 ± 1.2 MRD and in the [011] and [100] zones with values up to 3.4 ± 1.0 MRD.

6.3 Boundary-plane distributions

The kernel density estimation technique can be easily adapted to computation of distributions of boundary planes independent of misorientations. Such distributions can be computed from the viewpoint of the crystallite and laboratory reference frames; the latter has not been considered before. To compute a boundary plane distribution, all mesh segments represented by unit vectors (and vectors equivalent to these vectors) are processed; again, the distribution is probed at evenly distributed sampling directions and areas of mesh segments with normals deviated by less than a limiting radius ρ_p from a given direction are summed. Depending on the reference frame, different sets of equivalent representations are considered and the distribution is probed in different regions:

- To obtain a distribution in the crystallite frame, it is enough to probe the distribution at directions located in the standard stereographic triangle. Since we have to deal with grain-interchange symmetry, each segment is represented by normals $\mathbf{m}_1$ and $\mathbf{m}_2$ given in the first and second grains, respectively. Moreover, all their equivalent representations are given as $\pm C_1\mathbf{m}_1$ and $\pm C_2\mathbf{m}_2$. Assuming that n_s is the number of symmetry rotations, each segment is represented by up to $4 \times n_s$ vectors and all of them contribute to the distribution.

- To compute a distribution in the laboratory frame, one of the axes of the coordinate frame is chosen as a reference direction. When the reference axis is parallel or perpendicular to the direction of serial sectioning, we will refer to the corresponding distributions as *top* and *side* views, respectively. The distribution is computed in the Cartesian coordinate frame in which the z axis is aligned with the reference direction. The distribution is probed at the directions from the upper hemisphere. A vector $\mathbf{m}_{\mathrm{lab}}$ normal to a segment (representing that segment in the laboratory frame) is equivalent to $-\mathbf{m}_{\mathrm{lab}}$. Only boundaries of grains which are entirely contained in the considered 3D orientation map are taken into account.

After accumulation of mesh segments into the bins, the distribution is normalized with respect to the total area of all segments. Then the distribution is divided by the volumes of 'balls' determined by ρ_p[14]. In the case of five-

[14] In this case, the balls are actually spherical caps and the volumes are their areas.

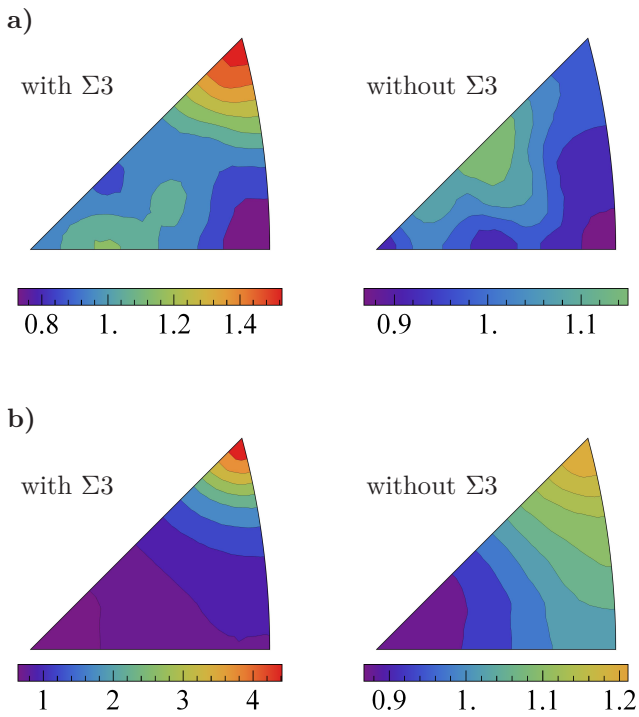

Figure 6.9: Distribution of boundary planes (in the crystallite frame) for *(a)* Nickel (UGent) and *(b)* Small IN100 data sets computed using kernel density estimation. In each pair, the left-hand side plot corresponds to complete data set, and the right-hand side plot was obtained for a subset of the data with Σ3 boundaries excluded. Contours are given in MRDs.

parameter boundary distributions, the ball volumes are computed numerically, but for two-parameter boundary-plane distributions, the volumes can be calculated analytically: let $V_p = (1 - \cos \rho_p)/2$ be the volume of a ball restricted by ρ_p. The volume occupied by a given mesh segment is V_p multiplied by the number of equivalent boundary-plane normals, so for the distributions given in the grain reference frame and laboratory reference frame, the normalized distributions are divided by $4 \times n_s \times V_p$ and $4 \times V_p$, respectively.

6.3.1 Examples

Boundaries with (111) planes in pure nickel and its alloy

Kernel density estimation was utilized for computation of the frequencies of occurrence of boundary planes (given in the crystallite reference frame) in Nickel (UGent) and Small IN100 data, i.e., in pure nickel and nickel-base su-

peralloy, respectively. For both samples, a peak appears at the (111) plane. For Nickel (UGent), its height is 1.5 MRD, while for Small IN100, it is 4.4 MRD (Fig. 6.9). This is not surprising as both materials contain significant (but obviously different) fractions of (coherent twin) $\Sigma 3/(111)$ boundaries. A boundary-plane distribution (in the grain frame) for Small IN100 was also obtained by Rohrer et al. (2010) using a variant of the partition-based method. General shape of that distribution was similar to the one shown in Fig. 6.9b; however, the height of the peak for the (111) plane was 2.6 MRD. As we already know this difference may originate from the spread caused by the averaging over the bins; moreover, since coherent twin boundaries are usually seen as flat surfaces, the result may be sensitive to the way of reconstruction (and smoothing) of boundaries.

As a cross-check, a boundary plane distribution was also computed for a subset of Small IN100 from which all $\Sigma 3$ boundaries were removed. For this subset, some maximum at the (111) plane should be still visible because of the presence of boundaries with misorientations about the [111] axis having the (111) planes; cf. Figs. 6.6d–f and Fig. 6.7b. Indeed, the (111) peak is still seen (Fig. 6.9b), though it is significantly lower (1.2 MRD) than that for the complete data. From analysis of an analogous subset of Nickel (UGent) with $\Sigma 3$ boundaries excluded, it can be inferred that, in the pure Ni sample, the amount of boundaries with the close-packed (111) planes different than $\Sigma 3$ coherent twin boundaries is the same as for the random boundaries because the maximum for the (111) plane is not visible anymore (Fig. 6.9a).

Its worth mentioning that the conclusions reached for Nickel (UGent) and Small IN100 data sets remain valid for Nickel (CMU) and Big IN100 data, respectively. Another comment concerns the errors of the boundary plane distributions; using formula from Eq.(6.1), for $\rho_p = 7^\circ$ the uncertainty is small even for small numbers of grains, e.g., at the (111) peak in the boundary plane distribution for Nickel (UGent), the relative error is $\varepsilon \approx 10\%$; for larger numbers of grain boundaries it becomes negligible.

Boundary planes seen from the laboratory

Distributions of boundary planes computed in the laboratory reference frame obtained for Ferrite, Small IN100, Big IN100, and Yttria are presented in Fig. 6.10. For each sample, the distributions are presented for two reference directions, i.e., as top and side views. The hot-rolled ferritic steel has a significant fraction of boundaries parallel (or near-parallel) to the rolling direction (i.e., perpendic-

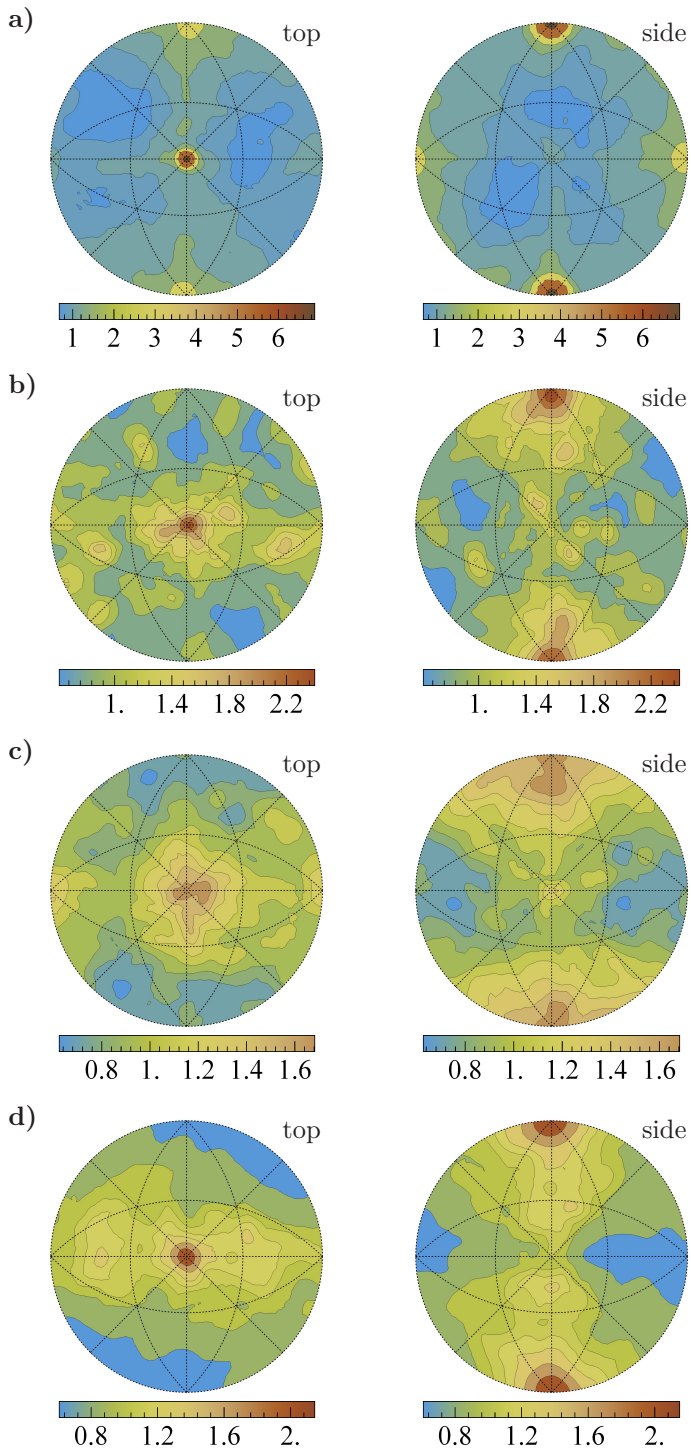

Figure 6.10: Distributions of boundary planes (in the laboratory frame) for *(a)* Ferrite, *(b)* Small IN100, *(c)* Big IN100, and *(d)* Yttria (these data do not include mesh segments adjacent to triple lines). In each pair the top and side views are shown.

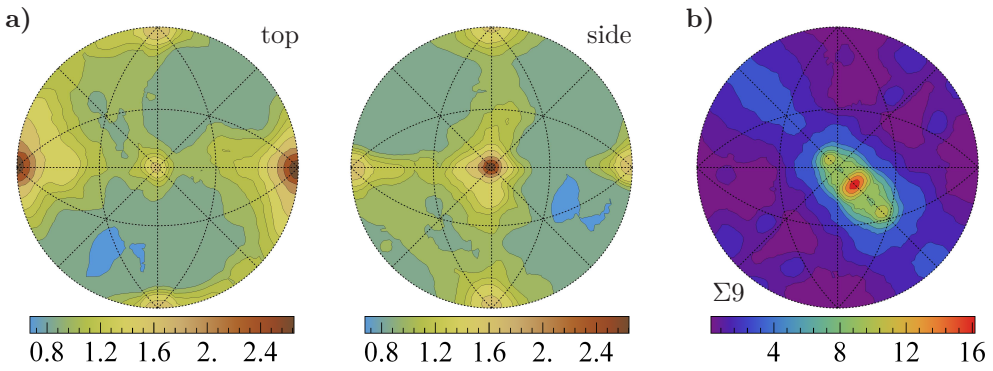

Figure 6.11: Distribution for data with mesh segments adjacent to triple lines included. *(a)* Distribution of boundary planes in the sample reference frame obtained for Yttria; to be compared with 6.10d. *(b)* Σ9 section through the distribution of grain boundaries obtained for Small IN100; to be compared with Fig. 6.2b.

ular to the direction of serial sectioning), and this is reflected by a strong peak with the intensity of about 7 MRD (Fig. 6.10a). Besides this peak, elevated distribution values (up to about 1.7 MRD) occur for planes perpendicular to the rolling direction. Interestingly, in the boundary-inclination distributions obtained for other data sets, boundaries perpendicular to the serial sectioning axis are also over-represented. The heights of corresponding peaks vary from 1.7 to 2.3 MRD. In the case of Ferrite data set, these deviations from the random distribution could be explained by the processing history of that steel. However, for all other materials having equiaxed grains, especially for sintered ceramics, we would rather expect distributions close to a uniform distribution at the level of 1 MRD. (Some possible fluctuations could be acceptable for sets with small numbers of boundaries.) Hence, it was suspected that these maxima are artifacts.

Therefore, the computational method was cross-checked using computer-generated microstructures; they were constructed as Voronoi tessellations with seeds being points randomly dispersed in certain volumes; also random orientations were ascribed to the (polyhedral) grains. Such data were obtained in two ways: exact tessellations were obtained using QHull (Barber et al., 1996) package whereas their voxelized approximations were generated using a dedicated in-house code. From the comparison of the distributions obtained for both types of artificial data, we learned that algorithms for smoothing grain boundary surfaces tend to leave stepped triple lines, especially if the voxels are not cubes, like in Yttria, where the in-plane resolution and the spacing between

slices differ by a factor of 4. This is the reason why these segments were ignored in the analyses presented in this work (cf. Chap. 4), although mesh segments directly neighboring triple lines constitute even 40% of all segments in some boundary networks. By removing these segments, the artifacts in the distributions of boundary planes in the laboratory frame were significantly reduced; compare Fig. 6.11a to Fig. 6.10d. However, even for the most isotropic material, Yttria, maxima for boundary planes parallel to the surfaces of the sample still remain (Fig. 6.10). Excess of such planes must be a result of the data acquisition method which results in voxelized data. On the other hand, it is observed that the larger the number of boundaries, the smaller the anisotropy in the distributions, so these distributions may also be sensitive to sizes of data sets.

The question then arose how the removal of the segments adjacent to triple lines affects grain boundary distributions given in the crystallite frame. It turned out that, for the distributions considered in this work, the influence was minor. Example of the distribution computed for a mesh with segments neighboring triple lines included is presented in Fig. 6.11b. The heights of the peaks are slightly larger compared to those in the analogous distribution obtained for the mesh without these segments; the removal of segments lying directly next to triple lines can be thought of as reduction of background and does not change general conclusions.

Chapter 7

GBToolbox

All approaches to characterization of boundaries discussed in the preceding chapters have been implemented in a package of computer programs called *GBToolbox*. The software has been written in the Java programming language, therefore, it is expected to run on all platforms equipped with Java Runtime Environment. The source code consists of about 40,000 lines. *GBToolbox* uses several external libraries: Commons Math 3.4.1, HDF-Java 2.9, JAMA 1.0.3, JavaML 0.1.5 (Abeel et al., 2009), VectorGraphics2D 0.9, JMathPlot, and JFontChooser 0.1. The package has been tested on Windows (XP, 7, and 8) and Linux operating systems. It is distributed with a user-friendly graphical interface. In what follows, the modules of the package are briefly described. Most of the features of *GBToolbox* work for data representing materials of the cubic O_h, hexagonal D_{6h}, tetragonal D_{4h}, and orthorombic D_{2h} holohedral symmetries.

Characterization of a bi-crystal

The historically first module of *GBToolbox* provides a user with a set of tools for a comprehensive geometric characterization of an individual boundary. For a user-specified boundary, the module calculates the distances from that boundary to the nearest tilt, twist, symmetric, and 180°-tilt boundaries[15]. Moreover, it returns macroscopic parameters of the nearest characteristic boundaries and the corresponding equivalent representations of the user's boundary for which these distances are minimal: it provides the symmetry transformations C_1 and

[15]By the distances, we also understand their approximations. Besides those, it is possible to compute Fortes tilt and twist angles; in some other modules, also the disorientation-based parameters can be determined. It is, however, passed over for brevity.

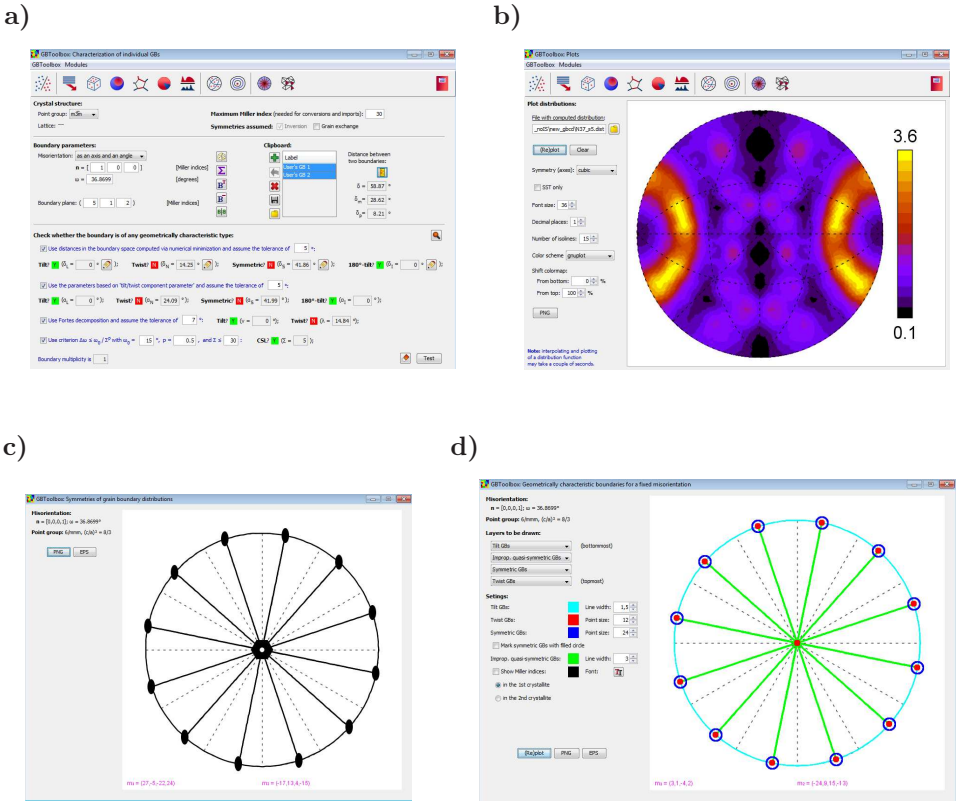

Figure 7.1: Screenshots taken from *GBToolbox*: *(a)* the module for characterization of bi-crystals, *(b)* the tool for previewing distributions saved in `dist`-files, and the windows showing diagrams with *(c)* symmetries of distributions and *(d)* locations of characteristic boundaries.

C_2 needed for obtaining those representations from the initial one and information whether inversion or grain-exchange symmetries must be applied. The misorientation of the boundary which is to be characterized can be input as rotation axis and angle, Euler angles, a rotation matrix, a quaternion, or Rodrigues parameters. Conversions between these parameterizations are possible. The boundary plane is determined by its Miller indices. The user's boundary representation can be transformed to the representation with the smallest-angle misorientation. For completeness, the module also calculates the distance δ_m in the misorientation subspace to the closest coincidence site lattice boundary. Furthermore, a simple tool for comparing two boundaries is included; it is possible to calculate the distances δ, δ_m, and δ_p for two arbitrary boundaries. The boundary characterization can be performed with distinction of the grains or with grain-interchange symmetry allowed.

Preparing data sets for analysis

In order to investigate of boundary data sets, parameters of boundaries need to be extracted from the experimentally collected 3D orientation maps. *GBToolbox* was *not* designed for this purpose, but it is capable of importing boundary networks already reconstructed using *DREAM.3D* program and reading its output files. The reconstructed boundaries are modeled by meshes of triangular segments with local boundary parameters ascribed to each of those segments (cf. Chap. 4). The imported meshes are stored in `gbdat` files. Each line of such a file contains a list of values characterizing one segment: Euler angles (in total, six) corresponding to (average) orientations of the adjacent grains, two spherical angles describing the boundary normal (expressed in the laboratory reference frame), area of the segment, and a number which tells us how many segments constitute a given boundary. Additional import options can be selected. A user can exclude boundaries belonging to surface grains (i.e., those which are cut and not fully contained within the analyzed map). One can also exclude borders of each boundary (narrow strips built of mesh segments directly neighboring triple lines); cf. Chap. 4. Furthermore, *QSlim* program (Garland and Heckbert, 1997) may be run in batch and utilized for mesh simplification: boundary surfaces can be approximated by other meshes which consist of smaller numbers of segments. The `gbdat` files are the input files for further analyses.

The created input files can be supplemented with the distances to the nearest tilt, twist, symmetric, and 180°-tilt boundaries. The distances are calcu-

lated for each mesh segment and they are appended to the corresponding lines of `gbdat` files. Such a processing of the input files is essential, e.g., for estimation of the fractions of geometrically characteristic boundaries in the considered set(s).

We have also seen that, in some cases, it is interesting (or even essential) to analyze different subsets of the data. *GBToolbox* allows for excluding boundaries of specified parameters (within assumed tolerances) from existing `gbdat` files.

Data sets filled with random boundaries are often used as reference data sets corresponding to the data with no anisotropy. *GBToolbox* allows for creating `gbdat` files containing random boundaries generated according to the model of uniformity determined by the distance function δ.

Analysis of boundary data sets

Another module of *GBToolbox* allows for analysis of the boundary networks saved in `gbdat` files; multiple files can be opened if a data set was split into several files. If the `gbdat` files have been previously processed so that they contain the distances to the nearest tilt, twist, symmetric, or 180°-tilt boundaries, then the fractions of boundaries which are classified to these (one or multiple) groups can be easily estimated; e.g., Tab. 5.1. *GBToolbox* includes the first implementation of the new approach for computation of grain-boundary distributions based on kernel density estimation[16]. If predefined limiting radii ρ_m and ρ_p are used, the distributions will be normalized (and expressed in multiples of random distribution) automatically. Other limiting radii can be specified, but in that case, the distributions need to be normalized manually using a provided tool. The computed distribution will be saved in a text file with the extension `dist`. These files consist of five columns. The first two numbers are coordinates corresponding to stereographic projection of boundary normal, the next two are zenith and azimuth angles representing that normal (in the crystallite reference frame), and the last value is the value of the distribution. During the normalization procedure an additional `dist` file is created. It contains the errors of the distribution.

To help in exploration of boundary distributions, a module for identification of symmetries of sections through the distributions for a given misorientation

[16] For cross-check purposes, the distributions of boundary populations can also be computed using the partition-based method. The same applies to boundary-plane distributions averaged over misorientations.

has been added. It displays the corresponding symmetry axes and mirror lines; cf. Fig. B.1. Similar module which instantly locates all tilt, twist, symmetric, and 180°-tilt boundaries for a fixed misorientation (using the analytical method) is provided; see Fig. B.2. As was already explained, the locations of (near-)characteristic boundaries can also be read from the distributions of the distances to the nearest geometrically characteristic boundaries. The capability of obtaining such distributions has also been added to *GBToolbox*. The program computes the distances for boundaries with a fixed misorientation and boundary normals forming a dense grid of directions; the results are saved to `dist`-format files. Eventually, a module for rough location of the maxima in the distributions is provided for testing; see Sec. 8.2.

Also the distributions of boundary planes can be computed with *GBToolbox* using a method adapting the kernel density estimation technique. Populations (given in MRD) of particular boundary planes can be considered from different viewpoints. One can consider boundary planes averaged over misorientations in both crystallite and laboratory reference frames (as in Sec. 6.3). There is also the idea of analyzing the distributions of boundary normals expressed in the second crystallite assuming a fixed normal in the first grain. In other words, we consider functions of four macroscopic parameters averaged over the fifth degree of freedom. Although *GBToolbox* allows for computing the distributions of the latter type, they are not discussed in this dissertation.

Visualization tools

GBToolbox has also been equipped with a simple plotting tool that displays contour graphs based on data stored in `dist` files. Depending on its type, a distribution can be plotted on a hemisphere or can be restricted to the standard stereographic triangle. Also, some other basic tools are provided: a user can set the density of isolines, choose colors representing function values, adjust legend font size, and export the obtained plots to `png` graphic files. With *GBToolbox* it is also possible to prepare `vtk` files containing mesh segments of boundaries with user-specified parameters. Such files can be displayed using, e.g., *ParaView* package (Henderson et al., 2004); see Fig. 4.2.

Chapter 8

Final remarks

Many important issues concerning grain boundary analysis have been already discussed in the examples presented in the previous chapters. There are still a couple of problems which are worth commenting on. The remarks are divided into two parts, each corresponding to one of the core chapters of the dissertation.

8.1 Comments on determination of the boundary character

Parameters α_L, α_N, α_S, and α_I for non-cubic symmetries

It has been shown that the parameters α_L, α_N, α_S, and α_I are correlated to δ_L, δ_N, δ_S, and δ_I, respectively, in the case of the cubic O_h crystal symmetry. In Sec. 5.3.4, the new parameters were used for obtaining diagrams containing locations of geometrically characteristic boundaries for the case of the hexagonal D_{6h} symmetry. This was justified because the correlations between the parameters α_L, α_N, α_S, and α_I and the corresponding distances δ_L, δ_N, δ_S, δ_I, respectively, have also been analyzed for the hexagonal D_{6h}, tetragonal D_{4h}, and orthorombic D_{2h} holohedries. These correlations are at the same levels as those in the cubic case. Thus, α_L, α_N, α_S, and α_I are also applicable to investigations of boundary networks in materials of these non-cubic symmetries. The corresponding reference PDFs for α_L, α_N, α_S, and α_I are presented in Fig. 8.1; 5×10^6 random boundaries for each of the three symmetries were generated to obtain these curves. As it was pointed out by Glowinski (2013), the lower the symmetry, the smaller the fractions of boundaries with special geometry (assuming the same limiting distance). For lower symmetries, the numbers of equivalent boundary representations are smaller, and therefore, the chances that a given boundary has a representation satisfying conditions

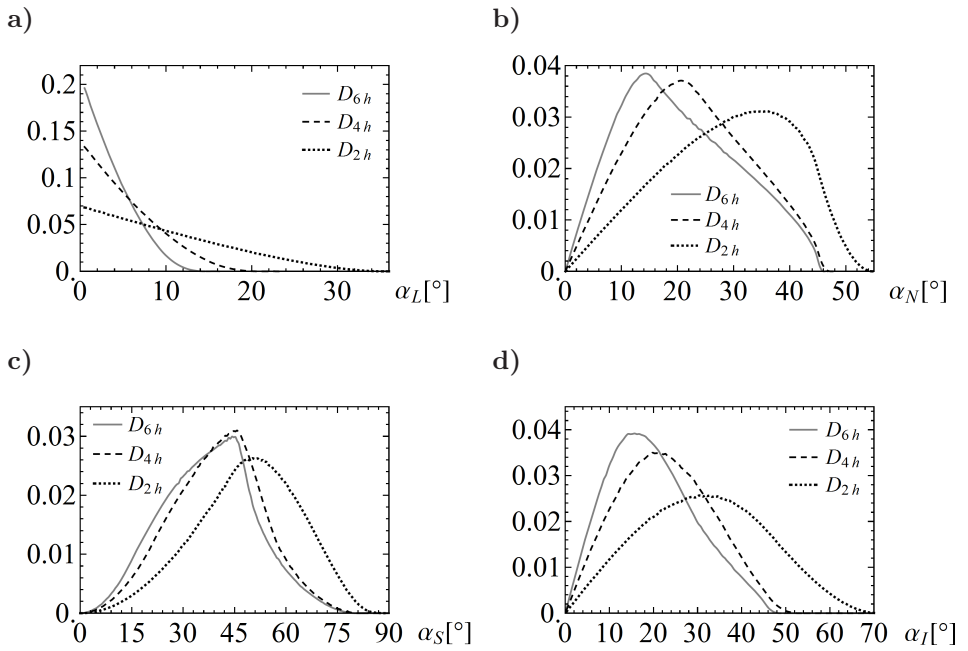

Figure 8.1: Probability density functions for the parameters α_L *(a)*, α_N *(b)*, α_S *(c)*, and α_I *(d)* for hexagonal (D_{6h}), tetragonal (D_{4h}), and orthorombic (D_{2h}) holohedral symmetries plotted using gray solid, black dashed and black dotted lines, respectively.

of being geometrically special are lower.

Peaks in PDFs for the distances to the nearest special boundaries

In all probability density functions for the distances (both accurate and approximate) to the nearest tilt, twist, symmetric, and 180°-tilt boundaries obtained in Chap. 5 for Small IN100 and Ferrite data sets, (reliable) elevated values happen to occur only for values close to zero and no maxima occur for larger values. However, it is not a general rule. For instance, from the analysis of the distributions of WC/WC boundaries in the WC-Co composites (Sec. 5.3.4), it turned out that the two most frequent boundary types are far from the nearest symmetric boundaries, namely with α_S at 30° and 79.4°; since the fractions of boundaries of these types are significant, peaks in the corresponding distribution for α_S will appear at those values.

Discrimination of tilt boundaries in the cubic case

The small maxima of the parameters δ_L and α_L as well as Figs. 2.2a and 2.3a indicate that deviations from pure-tilt boundaries are generally small compared to remaining parameters. It is worth adding that in the random case, the mean value of δ_L is only 1.6°, and about 84% of boundaries deviate from pure-tilt by $\delta_L \leq 3°$ (Morawiec, 2009b). These numbers suggest that with cubic O_h crystal symmetry, for boundaries to be reliably classified as near-tilt, a relatively high experimental accuracy (1° or better) would be needed.

As the maximal distance to the nearest pure-twist boundary is quite large, and mean distance is 11.8° (Morawiec, 2009b), the accuracy required for classification of near-twist boundaries is considerably lower. The latter applies also to symmetric and 180°-tilt boundaries as the maximum and mean values for the distances to symmetric and 180°-tilt boundaries are significantly larger than those for the distances to tilt boundaries (see Fig. 5.8).

On mesh simplification

Another way of reducing the time of processing of data of boundary networks is simplification of the reconstructed meshes by merging co-planar segments (e.g., Dillard et al., 2007; Garland and Heckbert, 1997). This way was employed to speed up the calculations described in Sec. 5.1. However, for the purpose of estimation of the percentages of tilt, twist, symmetric, and 180°-tilt boundaries in a given microstructure, it is much easier to take advantage of the new parameters α_L, α_N, α_S, and α_I and use them instead of the accurate distances.

8.2 Understanding boundary distribution

Distributions of grain boundaries with respect to their five macroscopic parameters are one of the most basic tools for investigating three-dimensional microstructure data. Therefore, it is extraordinarily important to understand these distributions in every detail. Key aspects of analyzing the distributions are summarized below.

Errors and statistics

Distributions of boundaries for a variety of materials can be found in many papers; however, their reliability has been evaluated only superficially. For

instance, accuracy of the distribution obtained by Dillon and Rohrer (2009) for Yttria was estimated using a test distribution computed for randomly generated boundaries (the number of random boundaries should be equal to the number of boundaries in experimental data). The maximum peak in the test distribution had the height of 1.6 MRD. Hence, Dillon and Rohrer (2009) assumed that only "peaks larger than this may be interpreted as real features of the distribution". In many works – even very recent, like those by Beladi et al. (2014) or Ratanaphan et al. (2014) – no uncertainties of the distributions are assessed. With the formula given by Eq.(6.1), it is possible to calculate directly the error of a distribution at any point.

Although the quantitative error estimation helps in resolving many doubts, there are more issues one should be aware of. For instance, Small IN100 and Big IN100 data sets were collected from two specimens of the same alloy, and thus, it is expected for the corresponding boundary distributions to be consistent. However, some discrepancies are easily seen. E.g., the heights of the peaks at the $\Sigma 7/(111)$ boundary are 29 ± 6 and 12 ± 2 MRD for Small IN100 and Big IN100, respectively. For the $\Sigma 9/(1\bar{1}4)$ boundary, they are 15 ± 4 and 6.4 ± 1.4 MRD, respectively. The differences in peak heights between the data sets are mainly the result of different numbers of boundaries in both samples. Such large fluctuations should diminish if the sizes of these sets were large enough.

It is also worth noting that the errors given by Eq.(6.1), and therefore, all errors plotted in Chap. 6, correspond to one standard deviation. To prove that boundaries of given parameters are over-represented in a microstructure, the lower limit for the height of the corresponding peak should exceed 1 MRD. The lower limit is obtained by subtracting a standard deviation times some factor from the nominal peak height. To assure oneself, it may be insufficient to subtract only one standard deviation. Some clear criteria would be needed, e.g., we could follow elementary particle physicists and say that there is an 'evidence' or a 'discovery' if the lower limit obtained by subtracting three and five standard deviations, respectively, is greater than 1 MRD.

The number of boundaries contributing to a peak

In some cases, mainly when data sets are small or when maxima in the distributions are small, the intensities of the peaks may exceed the corresponding errors, thus, it may be helpful to visualize boundaries of these particular parameters and verify how many distinct boundaries actually contributes to a

given peak. In some cases, like for Nickel (UGent), a relatively large maximum in the section for the 30°/[310] misorientation was the result of one large-area boundary. On the other hand, quite a weak maximum at Σ5/(512) boundary for Big IN100 data, was verified as coming from many boundaries of small area.

Symmetries and characteristic boundaries

Besides assuring ourselves which peaks can be interpreted as true features of distributions, it is also important to identify symmetries of the distributions and to know which peaks correspond to the boundaries having the same physical attributes.

E.g., in the Σ27a sections obtained for Nickel (CMU), there are peaks at $(2\bar{2}1)$ and $(\bar{4}47)$. If we determine indices of the boundary plane in the second grain, they are $(\bar{4}4\bar{7})$ and $(2\bar{2}\bar{1})$, respectively. Thus, we immediately see that these boundaries are crystallographically equivalent. Matching symmetrically equivalent peaks is particularly easy with the diagrams containing symmetry elements collected in Appx. B.

Having selected peaks of interest corresponding to distinct boundaries, it is interesting to verify whether these peaks correspond to tilt, twist, symmetric, 180°-tilt, tilt-twist, multiple-tilt, etc. boundaries. Again, such classification can be easily carried out using diagrams with the positions of all characteristic boundaries marked for given misorientations (Appx. B).

Comparison of boundary distributions to computed boundary energies

Since high populations of boundaries are correlated with their low energies (see Rohrer, 2011a, and references therein), comparison of the experimentally obtained distributions of boundary populations to computed distributions of boundary energies is another way of cross-checking the boundary distributions or facilitating their interpretation.

In a number of papers containing grain boundary distributions (e.g., Beladi and Rohrer, 2013b; Dillon and Rohrer, 2009; Li et al., 2009; Rohrer et al., 2010), also distributions of boundary energies computed based on geometry of triple junctions are presented. Because of technical reasons, this approach also uses partition of the boundary space into bins. Therefore, shapes of the energy distributions are distorted, e.g., sharp and deep energy minima become shallower. For instance, in the case of pure Ni, (relative) energies of Σ3 coherent twin boundary and the Σ3 boundaries of the highest energy are 0.34 and

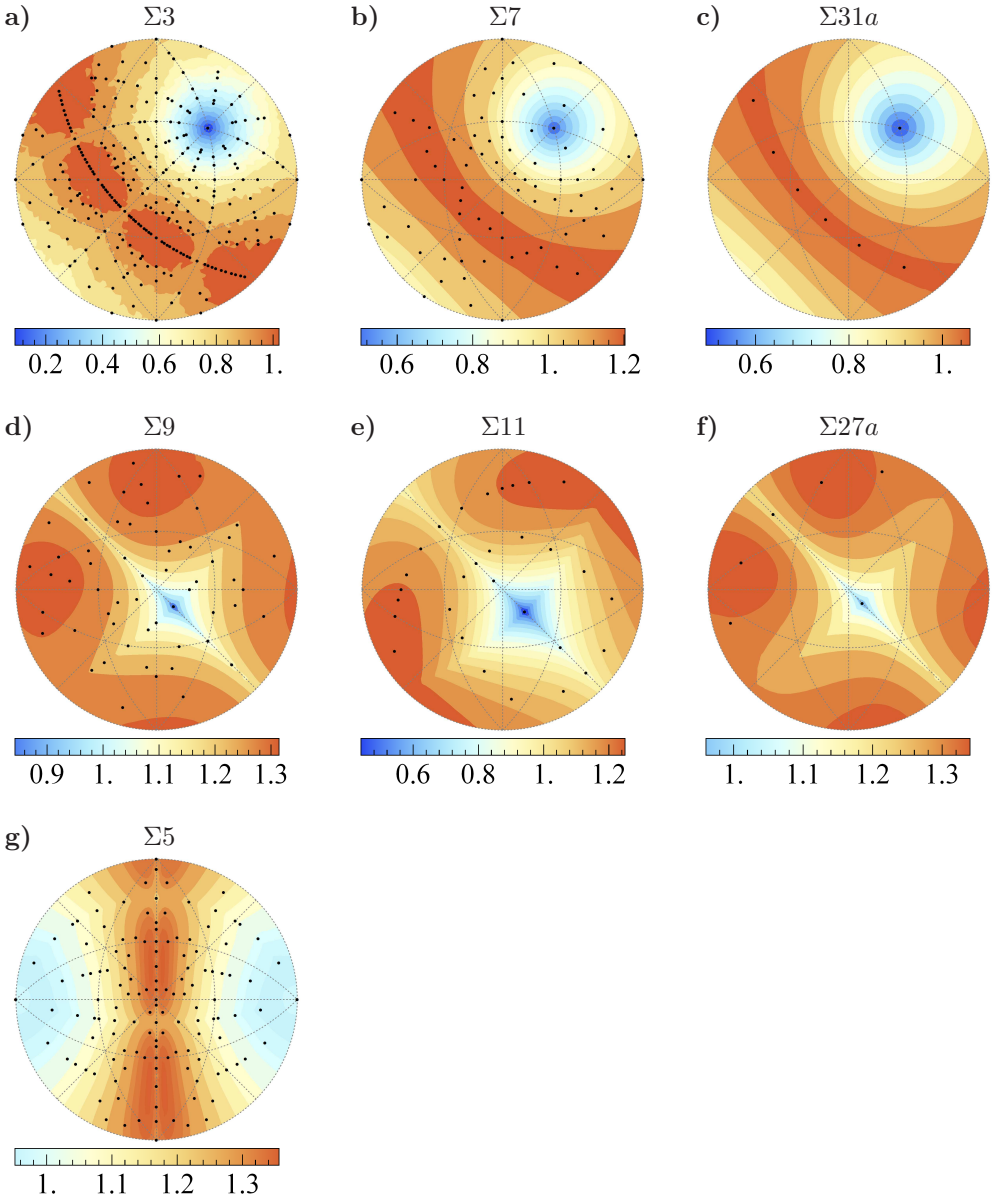

Figure 8.2: Energies of grain boundaries in nickel with the *(a)* Σ3, *(b)* Σ7, *(c)* Σ31*a*, *(d)* Σ9, *(e)* Σ11, *(f)* Σ27*a*, and *(g)* Σ5 misorientations as functions of boundary planes. The values were computed using a program provided by Bulatov et al. (2014) which computes the values of the interpolating function fitted to the energies computed by Olmsted et al. (2009) (black points). Contours are given in J/m^2.

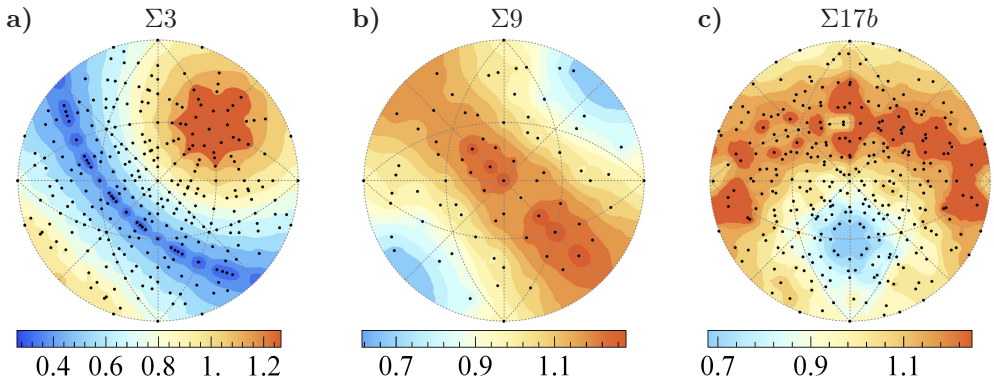

Figure 8.3: Energies of grain boundaries in BCC iron. Black points correspond to values computed via molecular-dynamics simulations. For the Σ3 and Σ9 misorientations (a,b), the data obtained by Ratanaphan et al. (2015) are shown, while for the Σ17b misorientation, the energies computed by Kim et al. (2011) are used. Contours are plotted using a simple inverse-square interpolation. Energies are given in J/m^2.

0.9 a.u., respectively; they differ by a factor of 3 (Fig. 2.8). Olmsted et al. (2009) calculated these energies via molecular-dynamics simulations to be 0.06 and about 1 J/m^2, respectively; the factor is about 16.

Geometry of triple junctions is also affected by experimental errors. In order to use boundary energy distributions for facilitating interpretation of population distributions, the energies should be computed independently from experimental data. At this point, energy databases obtained via molecular-dynamics simulations by Olmsted et al. (2009) (for FCC metals) and by Kim et al. (2011) and Ratanaphan et al. (2015) (for BCC metals) can be used. Energies of boundaries in nickel as functions of boundary planes for several CSL misorientations are presented in Fig. 8.2. To draw those plots, a function proposed by Bulatov et al. (2014) was used; this is an interpolating function fitted to the data computed by Olmsted et al. (2009). Since the shape of the function relating macroscopic boundary parameter with boundary energy seems to be universal (up to a scaling factor) for all FCC metals (Holm et al., 2010), these figures will also be used for discussing distributions for Ni-base alloy IN100. Analogous plots representing grain boundary energies in BCC iron obtained based on calculations performed by Ratanaphan et al. (2015) and Kim et al. (2011) are shown in Fig. 8.3.

The data base for Ni contains energies of only 388 ($\approx 3^5$) which means that the energy landscape depicted by the interpolation of Bulatov et al. (2014) is rather simplified. Nevertheless, some maxima in boundary populations ob-

served experimentally can be matched to local energy minima. For instance, the peaks at the (111) pole in the sections for misorientations about the [111] axis correspond to points with the lowest energies in those sections. The same applies to the $\Sigma 11/(1\bar{1}3)$ boundaries. To some extent also the experimental section for the $\Sigma 5$ misorientation is consistent with the simulations. On the other hand, for the $\Sigma 9$ and $\Sigma 27a$ misorientations, only the peaks at the $\Sigma 9/(1\bar{1}4)$ and $\Sigma 27a/(1\bar{1}5)$ boundaries, respectively, agree with the calculations. In both sections there are peaks (for $\Sigma 9$ at the $(\bar{1}15)|(1\bar{1}\bar{1})$, while for $\Sigma 27a$, it is $(1\bar{2}1)|(\bar{4}4\bar{7})$) which cannot be linked to local energy minima. However, since the energies were computed for such a small number of boundaries, the energy function may be oversimplified; the argument for this is that the peaks in the $\Sigma 9$ section correspond to minima in energy distributions obtained by the approach based on geometry of triple junctions (see Fig. 2.8c).

The data bases for Fe obtained by Ratanaphan et al. (2015) and Kim et al. (2011) contain energies of 408 and 66339 ($\approx 9^5$) boundaries, respectively. Even in the latter case, the points are still not very dense from the point of view of the 5D space. Both data bases lead to similar plots of boundary energies for the $\Sigma 3$, $\Sigma 9$, and $\Sigma 17b$ misorientations. The $\Sigma 3$ and $\Sigma 17b$ sections obtained for Ferrite are consistent with the simulations. It is difficult to judge if the simulations are consistent with the populations of $\Sigma 9$ boundaries, because the boundary distribution has large errors for this section.

Boundary multiplicity and spread of peaks

Another issue that has to be raised here is the influence of boundary multiplicities on shapes of boundary distributions. Assuming that a boundary has a multiplicity of 1, there is a relationship between the value f of a distribution at a given boundary and the fraction p of boundaries falling into the neighborhood of that boundary: $f = p/v$, where v stands for the volume of a region restricted by ρ_m and ρ_p. (It is assumed that boundaries in the neighborhood also have multiplicities of 1.) Since all equivalent boundary representations contribute to the distributions, the question arises about distribution values at – or in vicinities of – boundaries having multiplicities greater than 1.

Let us consider a test distribution computed using KDE for a data set containing only ideal $\Sigma 3/(111)$ boundaries (i.e., p for coherent twins is 100% or just 1). For the radii $\rho_m = 3^\circ$ and $\rho_p = 7^\circ$, v is equal approximately to 1/15600. Thus, f at $\Sigma 3/(111)$ should be equal to about 15600 MRD. Instead, twelve as high intensity at that point is observed. The factor of 12 is equal to the

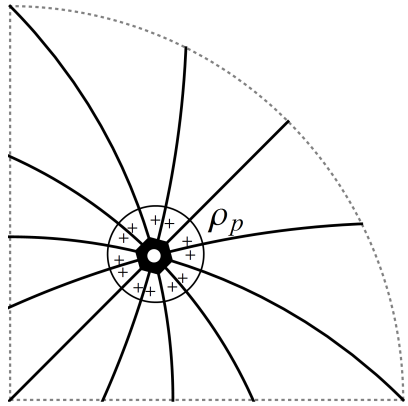

Figure 8.4: Symmetries of (a fragment of) the Σ3 section (cf. Patala and Schuh, 2013). The six-fold symmetry axis is parallel to the [111] direction, thick lines correspond to mirror lines. High-multiplicity boundaries frequently occur at the intersections of mirror lines; in this case, the multiplicity of the Σ3/(111) boundary is 12. Crosses denote equivalent representations of the same Σ3/near-(111) boundary. The circle surrounds all boundaries with planes deviated from (111) by less than the limiting radii ρ_p.

multiplicity of the Σ3/(111) boundaries. (The multiplicity of twin boundaries is relatively high, so its influence is significant.)

Another immediate question is: What are the values at high-multiplicity configurations in a distribution computed for random boundaries (used for normalization of experimental distributions)? It turns out that for large numbers of random boundaries, these values – even for high-multiplicity configurations – converge to 1 MRD (the larger the number of random boundaries, the smaller the fluctuations from unity). Hence, amplifications at high-multiplicity points in the experimental distributions are not compensated during normalization of the distribution functions.

In the distributions, elevated-multiplicity boundaries are located at mirror lines of the sections for fixed misorientations (especially at intersections of these lines), as well as at symmetry axes. A boundary which is slightly deviated from a high-multiplicity boundary (within assumed limiting radii) may also contribute multiple times at sampling points in the vicinity of that high-multiplicity boundary. This occurs if equivalent representations of a boundary are located close enough to one another; see Fig 8.4. (Similar effect would be observed when the partition-based method was used and the equivalent representations were contained in the same bin.)

Another test distribution was calculated for data containing 100% near-Σ3/(111). 'Near' means that random deviations of magnitudes which mimic experimental resolutions (cf. Figs. 5.5 and 6.2) were introduced to parameters of ideal Σ3/(111). This time, the peak at the twin boundary has obviously a smaller height, i.e., 34000 MRD. Since this intensity is larger than 15600 MRD despite the spread of parameters of twin boundaries, the impact of multiplicity is clear. Such simple simulations may be used for estimating true fractions of boundaries corresponding to a given maximum with accounting for both boundary multiplicity and experimental errors. The same technique is applicable to boundaries of multiplicity of 1: although they are not influenced by multiplicity, they are still affected by experimental uncertainties.

How to look for maxima in the boundary distributions?

For majority of the sections through boundary distributions which can be found in the literature, the misorientation was fixed to one of the CSL misorientations. This approach is convenient as the CSL misorientations are 'special' points in the misorientation space. There is physical motivation for considering twin misorientations and their derivatives, e.g., the Σ3, Σ9, and Σ27 misorientations. However, the need for a methodology for looking for maxima in the distributions is immediately seen.

Conceptually, the easiest solution would be to compute the distribution values at points uniformly dispersed in the 5D boundary space, to interpolate the distribution and to apply numerical methods for finding peaks. (In other words, to compute sections for misorientations densely distributed in the misorientation subspace.) However, such an approach would be time consuming.

Saylor et al. (2003a) and Ratanaphan et al. (2014) computed misorientation density function and then computed sections for those misorientations that are over-represented. In MDF, however, we get intensities averaged over boundary planes. This means that a section with one large peak at some pole and zero-value at other points may be seen as less intensive in the MDF than a section with the value slightly greater than zero for all boundary planes. This makes it not reliable to look for the maxima in the 5D boundary distributions based on 3D MDFs.

In this work, besides choosing just CSL misorientations, data bases containing calculated boundary energies were used to find the lowest-energy boundaries, and then, the corresponding sections through boundary population distributions were computed. Using this method, maxima, e.g., in the Σ11 section

for Nickel (CMU) and Big IN100, as well as the peak for the $\Sigma 17b$ misorientation in Ferrite were found. Another way was to use a preliminary version of a piece of software that searches for the maxima. To make it feasible, binning of the boundary space must have been used. However, the binning known from the partition-based method was inappropriate. Instead, sampling points were dispersed uniformly in the grain boundary space and the bins were constructed as a Voronoi tessellation with these points being seeds for Voronoi cells. The bins were filled with mesh segments and the bins containing the largest numbers of boundaries were found. This method indicated, e.g., the maxima in the $30^\circ/[310]$ section for Nickel (UGent).

It is interesting that all significant peaks in the boundary distributions occur for misorientations lying at the border of the asymmetric domain in the misorientation subspace, i.e., for boundaries of elevated multiplicities. The question to be considered in the future is if this is connected with multiple contributions of such boundaries to the distributions or, as suggested by Sutton and Balluffi (1987), high-multiplicity boundaries are energetically favorable.

Chapter 9

Summary

Several new approaches to quantitative characterization of 3D grain boundary networks have been developed. The new methods have been demonstrated using experimental boundary data sets and have been confronted with approaches known earlier. The main outcomes of these demonstrations and comparisons are collected below.

9.1 Conclusions

Ad distinction between tilt, twist, and mixed boundaries

Possible ways of analyzing mixed large-angle boundaries have been scrutinized. In the simplest classification, the considered methods are either based on the boundary decomposition into twist and tilt components or on other measures of deviations from pure-twist or -tilt boundaries. Furthermore, they are either limited to disorientations or take into account all symmetrically equivalent boundary representations.

As was shown in Sec. 2.6.1, the simplistic approaches limited to disorientations and ignoring other symmetrically equivalent boundary representations (with parameters ν, λ and α) provide only partial information about geometry of boundaries. Boundary characterization by these methods is inconsistent with the definitions of twist and tilt boundaries based on the requirement of existence of relationships between misorientation axis and the boundary plane (as the existence cannot be detected without examining all symmetrically equivalent boundary representations). In consequence, the approaches limited to disorientations are not suitable for comprehensive studies of boundary geometry.

Closeness of a boundary to the twist or tilt geometries can be detected

only by taking into account all boundary representations. Three different sets of parameters have been analyzed as possible measures of this closeness:
– the smallest angles (ν_F, λ_F) of boundary components obtained using Fortes decomposition,
– rigorously defined distances to pure-twist or tilt boundaries (δ_L, δ_N), and
– the newly introduced parameters (α_L, α_N) defined as the extreme values of the angle between the misorientation axis and the normal to the boundary plane.

The applicability of the Fortes decomposition and (ν_F, λ_F) parameters to analysis of boundaries is shown to be limited. It can be used for identification of ideal twist or tilt boundaries, but it is not suitable for analysis of error-affected data because of instability of one of the angles (ν_F) to small perturbations of input data.

Consequently, the choice of proper approaches to experimental grain boundary data is confined to the distances to pure-twist or pure-tilt boundaries (δ_L, δ_N) and extreme values of the angle between the misorientation axis and the normal to the boundary plane (α_L, α_N). Detailed analyzes show that the distances (δ_L, δ_N) are strongly correlated with the angles (α_L, α_N) and as such, the pairs are expected to lead to similar conclusions. However, computing the angles is considerably easier than getting the distances. Besides that, numerical costs of obtaining α_L and α_N are far lower compared to those of calculating δ_L and δ_N. This may be important in the case of characterizing large numbers of grain boundaries.

Ad recognizing symmetric and 180°-tilt boundaries

Methods for identification of symmetric and 180°-tilt boundaries have also been studied. One can of course calculate the distances δ_S and δ_I to the nearest symmetric and 180°-tilt boundaries, respectively. However, as in the case of looking for tilts and twists, calculation of the distances has high computational costs. Therefore, the alternative parameters α_S and α_I have been introduced to approximate the distances δ_S and δ_I, respectively. The correlations between the newly defined parameters and the distances have been examined, and since they are very high, the new parameters are a reliable replacement for δ_S and δ_I. Furthermore, α_S and α_I can be calculated in times significantly shorter than those for the distances.

Ad occurrence of characteristic boundaries in real polycrystals

Distributions of the new parameters substituting the distances to the nearest tilt, twist, symmetric, and 180°-tilt boundaries have been calculated for Small IN100 data set. Boundaries of α_L, α_N, α_S, and α_I close to zero were expected to be over-represented (compared to random boundaries) because of the high population of $\Sigma3/(111)$ twin boundaries, and elevated amount of $\Sigma7/(111)$ and $\Sigma9/(1\bar{1}4)$ boundaries; these three types of boundaries are simultaneously twist and 180°-tilt boundaries; besides that, geometries of $\Sigma3/(111)$ and $\Sigma9/(1\bar{1}4)$ are also symmetric. Therefore, two subsets of these data have also been processed: the first with $\Sigma3$ boundaries excluded, and the second one without CSL boundaries of Σ-values equal to 3, 5, 7, 9, 11, and $27a$. It turns out that excess amount of near-tilt boundaries is attributed to coherent twin boundaries. From the distributions corresponding to the subsets of Small IN100, it can also be inferred that the fractions of near-symmetric and near-180°-tilt boundaries different from high-coincidence boundaries are increased compared to the isotropic data. Based on analogous distributions of the parameters α_S and α_I for Ferrite and its subsets, it is concluded that near-symmetric and near-180°-tilt boundaries are over-represented in the studied ferrite sample, but majority of them are small-angle boundaries.

The same conclusions could be reached using the accurate distances, although times needed for the data processing would be longer.

Two complementary methods for obtaining diagrams indicating the reference points in the boundary space (i.e., those coinciding with tilt, twist, symmetric, and 180°-tilt boundaries) have been presented. The first is based on the boundary type-defining conditions and analytical derivations, while the second – numerical – utilizes the parameters α_L, α_N, α_S, and α_I (or adequate distances). Such diagrams have been applied to systematic characterization of the peaks occurring in the distribution of WC/WC boundaries in WC-Co composites (Kim et al., 2008) (WC exhibits the hexagonal D_{6h} symmetry, and c/a ratio is equal to $\sqrt{20/21}$). In this distribution, all the reported maxima happen to correspond to either single- or multiple-tilt boundaries, and their geometries are far from symmetric geometry. The two highest peaks are also identified as special boundaries being twist boundaries located at the intersections of multiple 180°-tilt zones. An atlas containing charts helpful in interpretation of sections through boundary distributions for CSL misorientations for materials with the cubic O_h symmetry are collected in Appx. B.

Ad computation of grain-boundary distributions

The new approach to computation of grain boundary distributions based on the kernel density estimation technique has been developed; it allows for elimination of artifacts affecting the distributions obtained by the conventional partition-based method. Weak maxima are better pronounced and distinguishable in the distributions computed using the new method. The control parameters of the new approach can be easily adjusted to experimental resolution, sizes of data sets and errors of distribution functions. Although the reliability of grain boundary distributions depends mainly on the amount and quality of experimental data, it is also important to analyze the data using tools that do not distort the final results. Moreover, reliability of the distributions should always be double-checked. This includes, e.g., estimation of the statistical errors of distribution values using the proposed formula and verification of the number of distinct grain boundaries contributing to a maximum of a distribution.

Ad grain-boundary distributions for Ni-base metals and ferrite

Grain boundary distributions for four recrystallized FCC metals (two pure nickel samples and two specimens of Ni-based superalloy IN100) have been computed using the KDE-based method. The obtained distribution functions have certain common features. There is always a significant peak at the $\Sigma3/(111)$ coherent twin boundary and a maximum at the $\Sigma9/(1\bar{1}4)$ boundary. For Nickel (CMU) and Big IN100, there are peaks at the $(1\bar{1}3)$ pole for the $\Sigma11$ misorientation. In the case of Small and Big IN100, relatively high peaks are seen for other misorientations about the [111] axis.

Since most artifacts in grain-boundary distributions are reduced if KDE is used instead of the partition-based approach, the new method allows for detailed interpretation of the $\Sigma9$ and $\Sigma27a$ sections as they do not overlap (the overlap occurring in the conventional method with typical "10°-bins" is avoided). In the $\Sigma9$ sections obtained for all four data sets, besides the maximum for the $(1\bar{1}4)$ plane, peaks appear in the neighborhood of the $(\bar{1}15)$ and $(1\bar{1}1)$ poles; however, these maxima are slightly shifted from those poles (in a different way for each data set). In the $\Sigma27a$ section obtained for Nickel (CMU), three maxima occur: for the $(1\bar{1}5)$, $(2\bar{2}1)$, and $(\bar{4}47)$ planes. The last three have not been reported in the previous studies carried out by Li et al. (2009) using the partition-based method.

Peaks in the population distributions tend to occur at the locations of local

energetic minima which are known from molecular-dynamics simulations. We are not able to confirm this statement for the peaks for the $\Sigma 9/(\bar{1}15)|(1\bar{1}\bar{1})$ and $\Sigma 27b/(2\bar{2}1)|(\bar{4}4\bar{7})$ boundaries. This is caused by the fact that energies were computed only for a couple of boundaries with the $\Sigma 9$ and $\Sigma 27a$ misorientations. Hence, for a proper interpretation, data for denser grid of points in the critical regions of the boundary space would be needed. Interestingly, the $\Sigma 9/(\bar{1}15)|(1\bar{1}\bar{1})$ peaks coincide with local energy minimum obtained using the approach for estimating relative boundary energies based on triple junction geometry.

Distributions for Ferrite, which is a BCC material, are significantly different from those for FCC metals. There were significant peaks for the $\Sigma 3$ and $\Sigma 17b$ sections; the latter have not been seen in the previous analyses with the partition-based method (Beladi and Rohrer, 2013b). The position of the most intensive maximum nearly matches the local energy minimum obtained by Kim et al. (2011).

Ad boundary-plane distributions

The kernel density estimation technique has also been utilized for computing the distributions of boundary planes. These distributions have been analyzed in both crystallite and laboratory reference frames.

From the boundary-plane distributions in the crystallite frame obtained for pure nickel and Ni-based alloy IN100, as well as their subsets with $\Sigma 3$ boundaries excluded, one can infer that the maxima in the distributions for the (111) plane are dominated by coherent twin boundaries. In the data without $\Sigma 3$ boundaries, and hence, without the coherent twin boundaries, there is no peak for pure nickel. In the case of the alloy, the peak is still observed, tough it is significantly lower. This result is consistent with the corresponding five-parameter distribution.

Particularly interesting are the distributions of boundary plane inclinations seen in the laboratory frame. It is observed that experimental procedure or reconstruction algorithms result in excess of boundary segments parallel to external surfaces of the samples.

9.2 Closing remarks

Analysis of grain boundary networks based on all five macroscopic parameters has become an important branch of so-called 3D materials science. The number

of laboratories equipped with experimental apparatus for 3D grain-orientation mapping is increasing. Moreover, experimental techniques are being improved in order to make it possible to collect even larger data sets. The hitherto used tools for boundary studies have various deficiencies. In this work, several new methods for more reliable and more efficient geometric characterization of both individual bi-crystals and complex boundary networks have been developed and tested using experimental data. Furthermore, a multi-platform software package called *GBToolbox* has been created. It includes, i.a., implementations of all the new approaches described in this work; this makes it unique among other computer programs related to boundary analysis. *GBToolbox* is freely available; it can be downloaded from `http://imim.pl/personal/adam.morawiec/A_Morawiec_Web_Page/S/K_Glowinski/Downloads.html`. Finally, since an extensive list of issues connected with grain boundary analysis have been thoroughly discussed, this dissertation can be treated as a source of hints for three-dimensional studies of boundary networks in polycrystalline materials.

Acknowledgments

I would like to thank my advisor Prof. Adam Morawiec for his guidance during my graduate studies and for his hints when I was writing this dissertation.

Provision of three-dimensional orientation maps by Prof. Gregory S. Rohrer (Carnegie Mellon University, USA), Dr. Michael A. Groeber (US Airforce Research Laboratories), and Hadi Pirgazi and Prof. Leo A.I. Kestens (Ghent University, Belgium) is gratefully acknowledged.

I am also thankful to Katarzyna Stan-Głowińska and Klaudia Trembecka-Wójciga (Institute of Metallurgy and Materials Science, Cracow), as well as Dawid Dul and Grzegorz Rut (Jagiellonian University in Cracow) for their remarks on the manuscript.

This work was co-financed by the European Union under the European Social Fund within project No. POKL.04.01.00-00-004/10.

The author was a scholar within the project *Doctus – Małopolska scholarship fund for PhD students* co-financed by the European Union under the European Social Fund.

The author received funds for the work on this dissertation from the National Science Center Poland within *ETIUDA* doctoral scholarship based on decision DEC-2014/12/T/ST8/00086.

Appendix A

Data sets

The methods developed in this work have been tested using six 3D microstructure data sets. These data were provided by courtesy of researchers working at Carnegie Mellon University (USA), US Airforce Research Laboratories, and Ghent University (Belgium). Each of the data sets was handed over in the form of a stack of 2D orientation maps acquired using EBSD technique combined with serial sectioning; in the case of Nickel (CMU), Nickel (UGent), and Big IN100 data sets, the samples were sectioned via mechanical polishing, while for Small IN100, Ferrite, and Yttria data, subsequent layers of a material were removed using a focused ion beam. Four of these data sets were either pure nickel (Nickel (CMU), (UGent)) or nickel-based superalloy (Small, Big IN100) samples; these are FCC metals. Besides them, there were a sample of BCC ferritic steel with the composition: C – 0.04%, Mn – 1.52%, Si – 0.2%, Mo – 0.22%, Ti – 0.08%, Al – 0.033% (percentages by weight) and a specimen of undoped yttria with the bixbyite crystal structure. All materials were fully recrystallized: Nickel (CMU) was cold-rolled and then annealed; superalloy IN100 was produced by powder-metallurgy processing, then it was forged and subsolvus heat-treated; Ferrite underwent a multiple-stage thermo-mechanical processing; Yttria was cold-pressed isostatically and then sintered. 3D orientation maps, after the reconstruction and clean-up procedures described in Chap. 4, are visualized in Fig. A.1. (Yttria consists of three subsets which were cut from the complete data; remaining parts were of poor quality; see Chap. 4.) A reader interested in more detailed description of the materials, their processing histories, as well as of technical details of data acquisition is referred to the original papers authored by the researches who actually prepared the samples and acquired the 3D data; see Tab. A.1. Basic characteristics of the data sets, such as volumes of the orientation maps, their resolutions, number of grains

contained in these volumes, and average grain diameters are also collected in Tab. A.1.

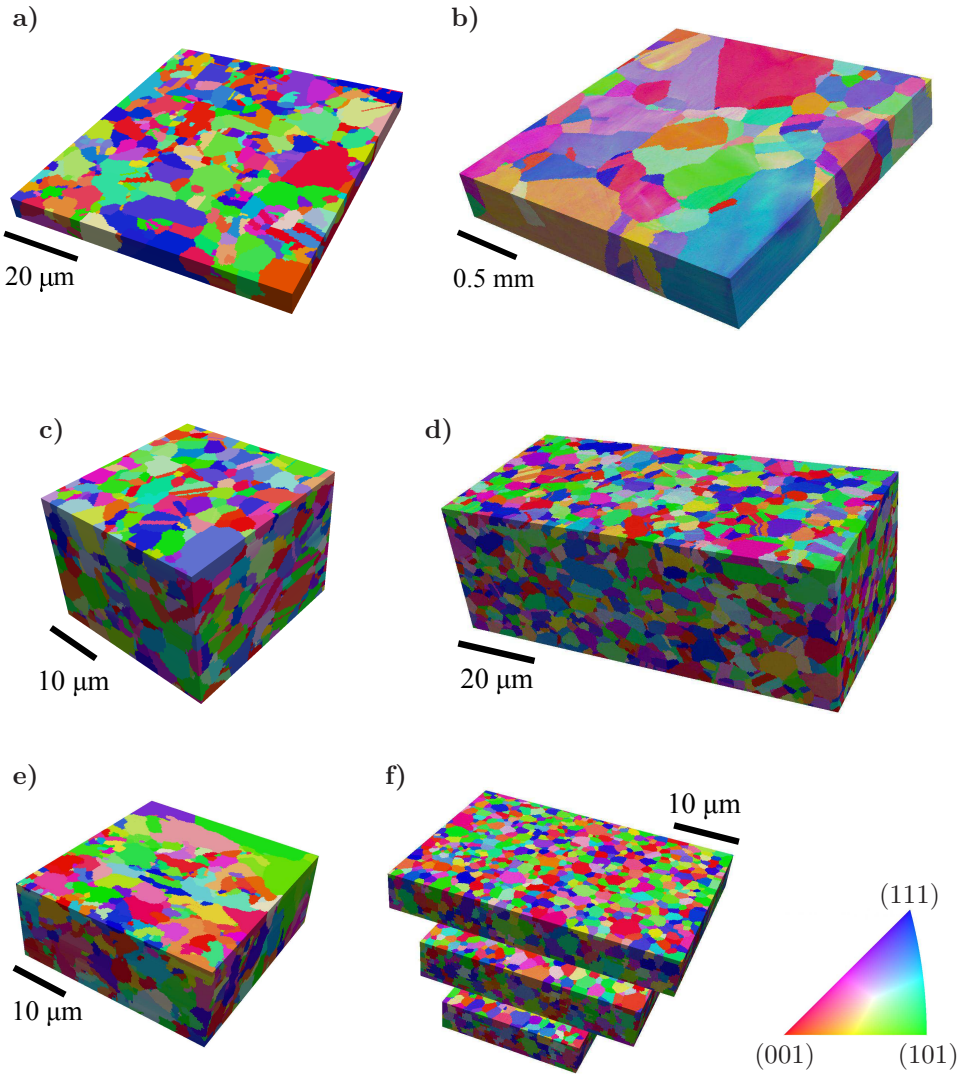

Figure A.1: Visualizations of the data sets used in this work: *(a)* Nickel (CMU), *(b)* Nickel (UGent), *(c)* Small IN100, *(d)* Big IN100, *(e)* Ferrite, and *(f)* Yttria. The data are represented as 3D inverse pole figure maps; grains are colored according to the legend. Dimensions of these maps can be found in Tab. A.1.

Table A.1: Basic characteristics of the 3D data sets used in this work. References to the articles describing both the materials from which these data sets were acquired and the experimental setups for data collection are given in the rightmost column.

Data set	Volume	In-plane resolution	Slice thickness	Number of grains	Average grain diameter	Reference
Nickel (CMU)	$85 \times 75 \times 6$ μm^3	0.2 μm	0.2 μm	840	3.4 μm	Li et al. (2009)
Nickel (UGent)	$2.26 \times 2.21 \times 0.35$ mm^3	6 μm	7 μm	280	0.16 mm	–
Small IN100	$40 \times 30 \times 30$ μm^3	0.25 μm	0.25 μm	2,200	3.1 μm	Groeber et al. (2006)
Big IN100	$96 \times 36 \times 46$ μm^3	0.25 μm	0.25 μm	8,900	3.1 μm	Groeber et al. (2008a,b)
Ferrite	$40 \times 35 \times 14$ μm^3	0.15 μm	0.2 μm	1,600	2.2 μm	Beladi and Rohrer (2013b)
Yttria	$40 \times 29 \times 5.3$ μm^3 + $31 \times 29 \times 5.9$ μm^3 + $21 \times 29 \times 4.8$ μm^3	0.07 μm	0.28 μm	6,800	1.4 μm	Dillon and Rohrer (2009)

Appendix B

Charts for interpreting functions of macroscopic parameters

Figures below show schematics intended to aid interpretation of functions of the five macroscopic boundary parameters (e.g., frequencies of occurrence, energies) in the case of cubic O_h crystal symmetry. Diagrams with symmetries of such functions (cf. Patala and Schuh, 2013) and with locations of geometrically characteristic boundaries (see Chap. 5.3) are presented in Figs. B.1 and B.2, respectively. The functions are most often shown as 2D sections for CSL misorienatations. Therefore, the diagrams are drawn in the form of 2D patterns for misorientations corresponding to subsequent Σ-values ($\Sigma \leq 31$ and $\Sigma = 39a$).

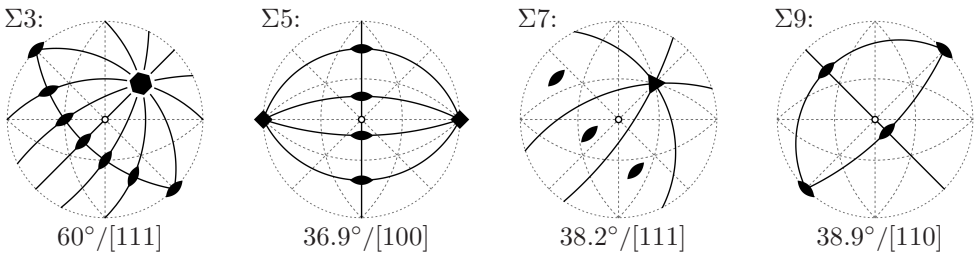

Figure B.1: Symmetries of sections for CSL misorientations for Σ-values ≤ 31 and $\Sigma = 39b$ for cubic symmetry; the corresponding misorientation angles and axes are given. Solid lines represent mirror lines, the symbol "○" stands for the inversion center, while 2-, 3-, 4-, and 6-fold axes are marked by "⬮", "▲", "◆", and "⬢", respectively. The symmetry elements are drawn in stereographic projections. Symmetries for arbitrary misorientations, as well as for other crystal symmetries, can be obtained using *GBToolbox*.

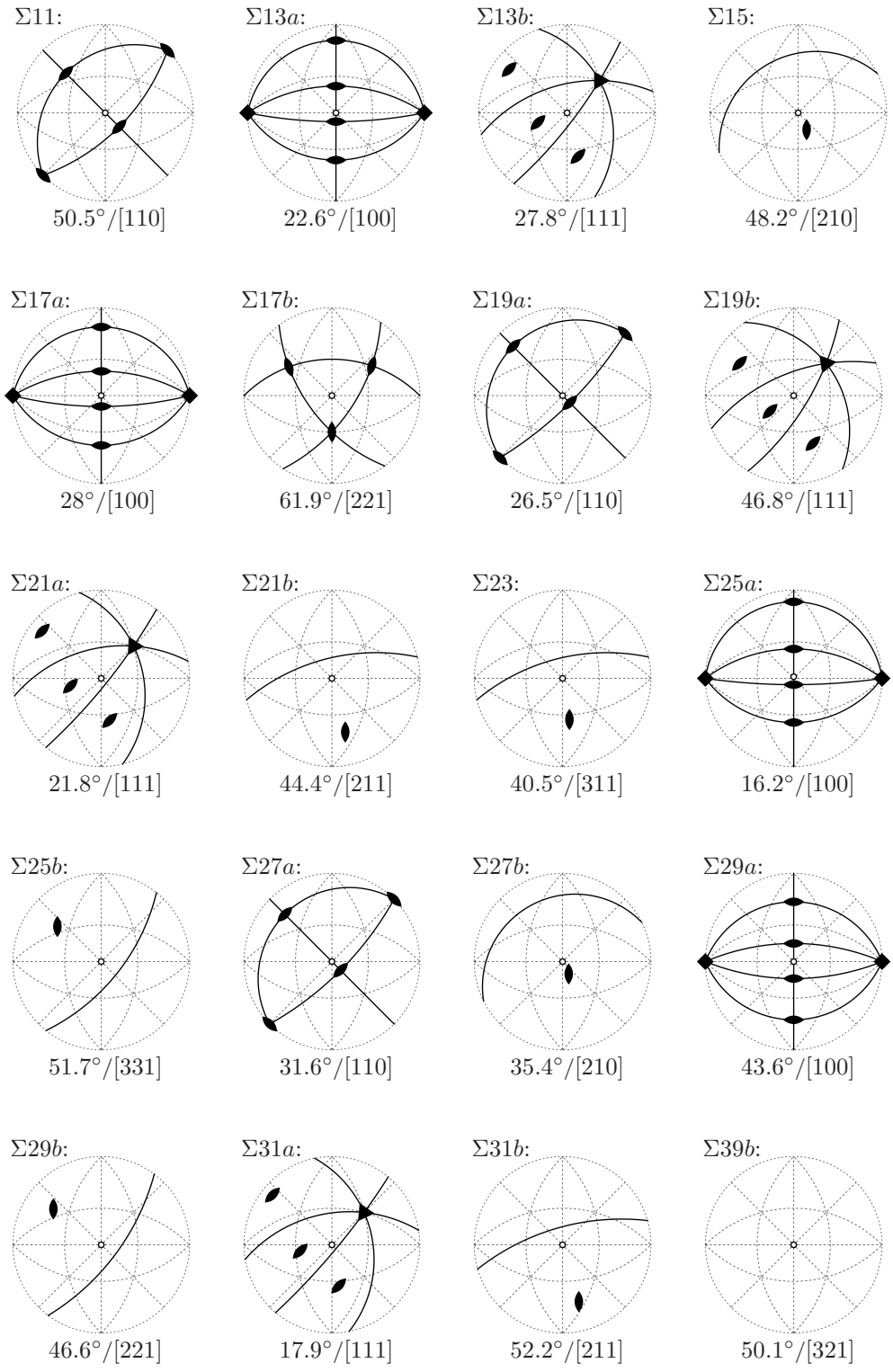

Figure B.1: Continued.

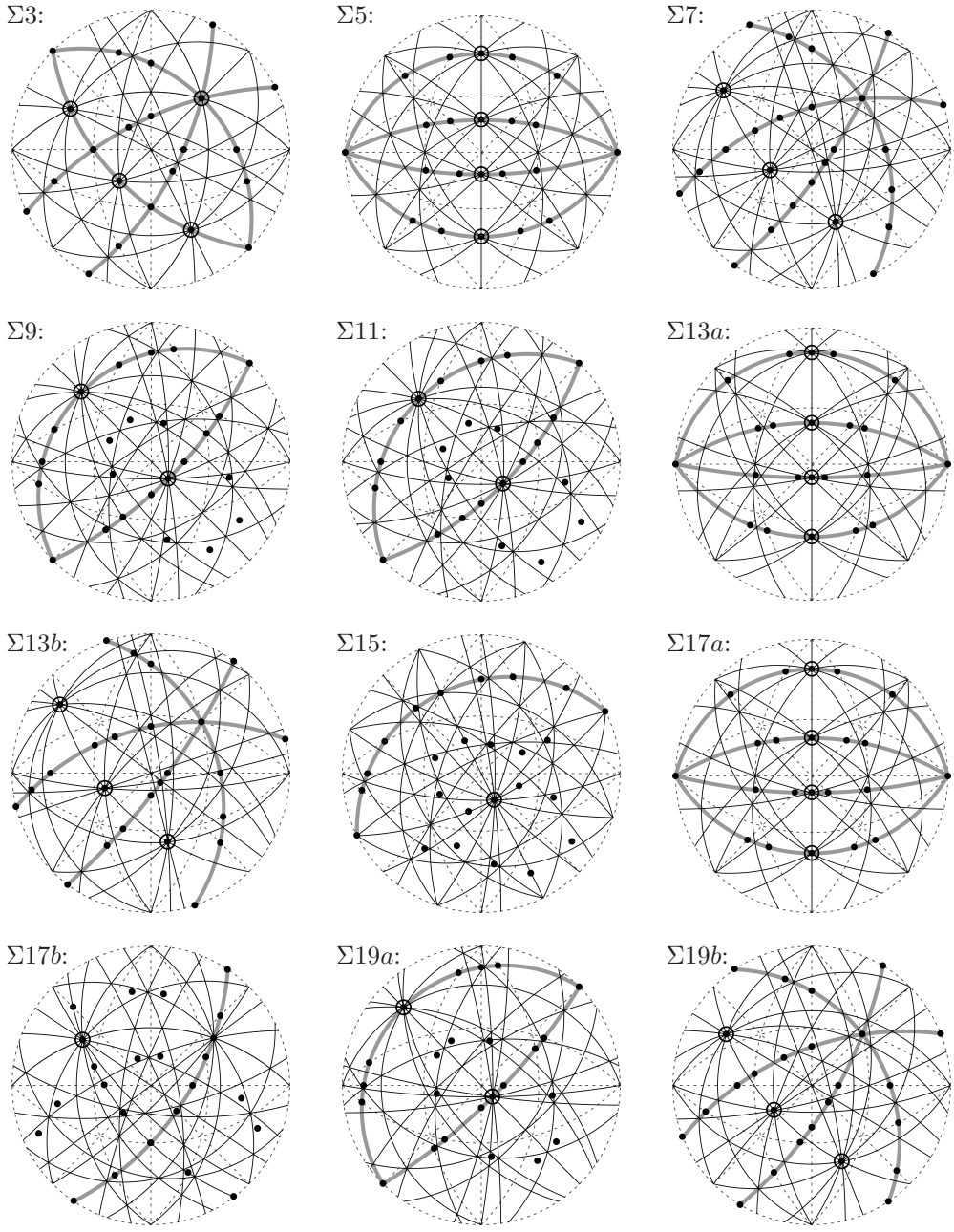

Figure B.2: Locations of geometrically characteristic boundaries for CSL misorientations (for the cubic crystal symmetry). Tilt, twist, symmetric, and 180°-tilt boundaries are represented by black lines, thick gray lines, points, and circles, respectively. Locations of characteristic boundaries for other misorientation (and for other crystal symmetries), as well as indices of the corrseponding boundary planes, can be obtained using *GBToolbox*.

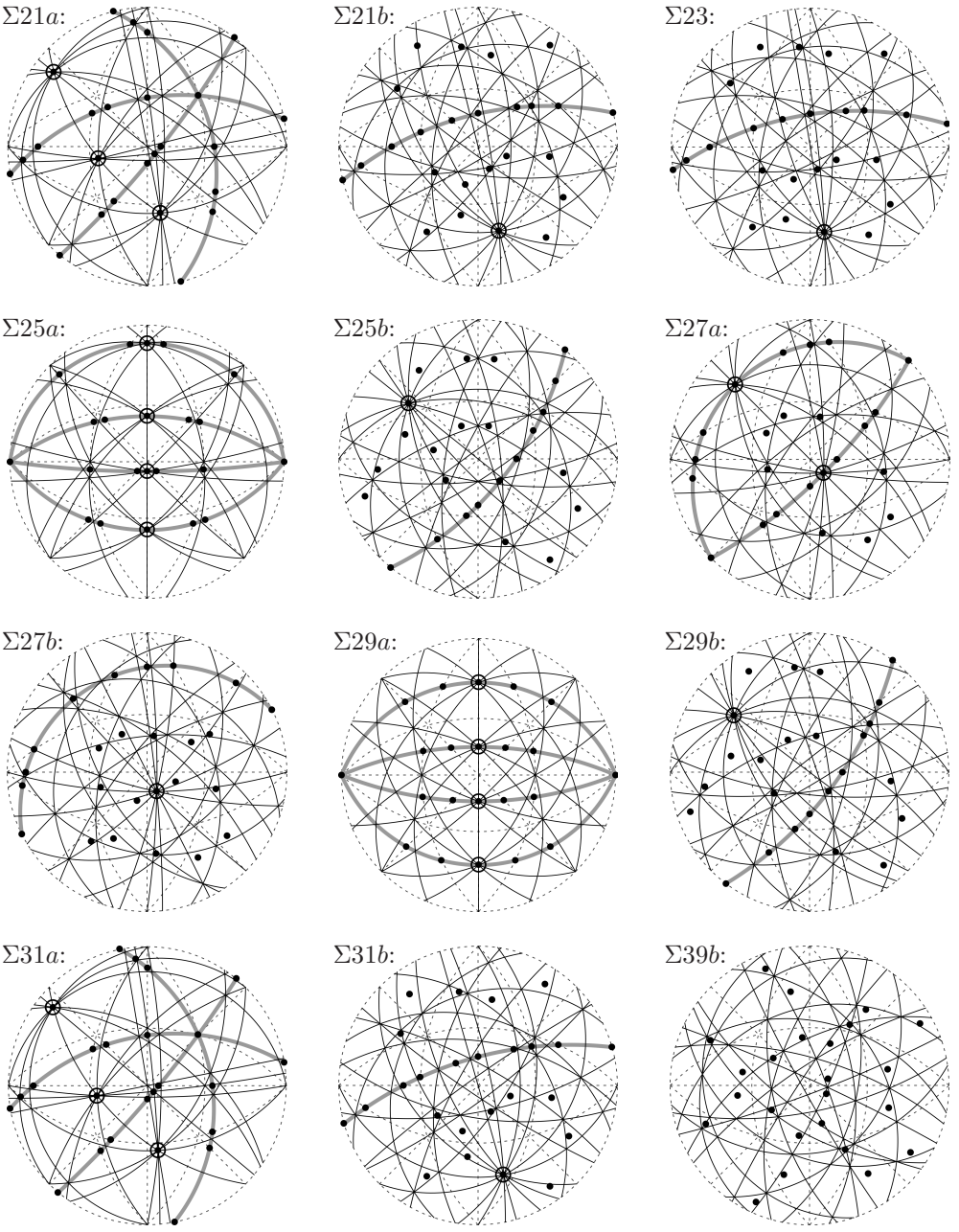

Figure B.2: Continued.

Bibliography

Abeel, T., de Peer, Y. V., and Saeys, Y. (2009). Java-ML: A machine learning library. *J. Mach. Learn. Res.*, 10:931–4.

Ainsley, M. H., Cocks, G. J., and Miller, D. R. (1979). Influence of grain boundary structure on discontinuous precipitation in austenitic steel. *Met. Sci.*, 13:20–4.

Amouyal, Y., Rabkin, E., and Mishin, Y. (2005). Correlation between grain boundary energy and geometry in Ni-rich NiAl. *Acta Mater.*, 53:3795–805.

Ashby, M. F., Spaepen, F., and Williams, S. (1978). The structure of grain boundaries described as a packing of polyhedra. *Acta Metall.*, 26:1647–63.

Bachmann, F., Hielscher, R., and Schaeben, H. (2011). Grain detection from 2D and 3D EBSD data-specification of the MTEX algorithm. *Ultramicroscopy*, 111:1720–33.

Balluffi, R. W. (1982). Grain boundary diffusion mechanisms in metals. *Metall. Trans. B*, 13:527–53.

Barber, C. B., Dobkin, D. P., and Huhdanpaa, H. (1996). The quickhull algorithm for convex hulls. *ACM T. Math. Software*, 22:469–83.

Bechtle, S., Kumar, M., Somerday, B. P., Launey, M. E., and Ritchie, R. O. (2009). Grain-boundary engineering markedly reduces susceptibility to intergranular hydrogen embrittlement in metallic materials. *Acta Mater.*, 57:4148–57.

Beladi, H., Nuhfer, N. T., and Rohrer, G. S. (2014). The five-parameter grain boundary character and energy distributions of a fully austenitic high-manganese steel using three dimensional data. *Acta Mater.*, 70:281–9.

Beladi, H. and Rohrer, G. S. (2013a). The distribution of grain boundary planes in interstitial free steel. *Metall. Mater. Trans. A*, 44:115–24.

Beladi, H. and Rohrer, G. S. (2013b). The relative grain boundary area and energy distributions in a ferritic steel determined from three-dimensional electron backscatter diffraction maps. *Acta Mater.*, 61:1404–12.

Bouchet, D. and Priester, L. (1987). Grain boundary plane and intergranular segregation in nickel-sulfur system. *Scripta Metall.*, 21:475–8.

Brandon, D. G. (1966). The structure of high-angle grain boundaries. *Acta Metall.*, 14:1479–84.

Bulatov, V. V., Reed, B. W., and Kumar, M. (2014). Grain boundary energy function for fcc metals. *Acta Mater.*, 65:161–75.

Bunge, H.-J. (1982). *Texture analysis in materials science: mathematical methods*. Butter-

worths.

Cahn, J. W. and Hoffman, D. W. (1974). A vector thermodynamics for anisotropic surfaces—ii. curved and faceted surfaces. *Acta Metall.*, 22:1205–14.

Cahn, J. W. and Taylor, J. E. (2006). Metrics, measures, and parametrizations for grain boundaries: a dialog. *J. Mater. Sci.*, 41:7669–74.

Chalmers, B. (1949). Some crystal-boundary phenomena in metals. *Proc. Roy. Soc. (London) A*, 196:64–74.

Chen, Y. and Schuh, C. A. (2006). Diffusion on grain boundary networks: Percolation theory and effective medium approximations. *Acta Mater.*, 54:4709–20.

Cheung, C., Erb, U., and Palumbo, G. (1994). Application of grain boundary engineering concepts to alleviate intergranular cracking in alloys 600 and 690. *Mater. Sci. Eng. A*, 185:39–43.

Davies, P. and Randle, V. (2001). Grain boundary engineering and the role of the interfacial plane. *Mater. Sci. Tech. Ser.*, 17:615–26.

Déchamps, M., Baribier, F., and Marrouche, A. (1987). Grain-boundaries: Criteria of specialness and deviation from CSL misorientation. *Acta Metall.*, 35:101–7.

Desai, T. G., Nerikar, P., and Uberuaga, B. P. (2009). The role of grain boundary structure in stress-induced phase transformation in UO_2. *Model. Simul. Mater. Sc.*, 17:064001.

Dillard, S. E., Bingert, J. F., Thoma, D., and Hamann, B. (2007). Construction of simplified boundary surfaces from serial-sectioned metal micrographs. *IEEE T. Vis. Comput. Gr.*, 13:1528–35.

Dillon, S. J. and Rohrer, G. S. (2009). Characterization of the grain-boundary character and energy distributions of yttria using automated serial sectioning and EBSD in the FIB. *J. Am. Ceram. Soc.*, 92:1580–5.

Dunn, C. G. and Lionetti, F. J. (1949). The effect of orientation difference on grain boundary energies. *Trans. Met. Soc. AIME*, 185:125–32.

Echlin, M. P., Mottura, A., Torbet, C. J., and Pollock, T. M. (2012). A new TriBeam system for three-dimensional multimodal materials analysis. *Rev. Sci. Instr.*, 83 : 023701.

Fecht, H. J. and Gleiter, H. (1985). A lock-in model for the atomic structure of interphase boundaries between metals and ionic crystals. *Acta Metall.*, 33:557–62.

Field, D. P. (1995). On the asymmetric domain of cubic misorientations. *Scripta Metall. Mater.*, 32:67–70.

Fortes, M. A. (1973). Tilt and twist boundaries. *Acta Cryst. A*, 29:68–70.

Furuhara, T. and Maki, T. (2005). Grain boundary engineering for superplasticity in steels. *J. Mater. Sci.*, 40:919–26.

Furukawa, M., Horita, Z., and Langdon, T. G. (2005). Processing by equal-channel angular pressing: Applications to grain boundary engineering. *J. Mater. Sci.*, 40:909–17.

Garland, M. and Heckbert, P. S. (1997). Surface simplification using quadric error metrics. In *Proceedings of the 24th Annual Conference on Computer Graphics and Interactive Techniques*, pages 209–16.

Gault, B., Moody, M. P., Cairney, J. M., and Ringer, S. P. (2012). Atom probe crystallogra-

phy. *Mater. Today*, 15:378–86.

Gertsman, V. Y. (2001). Geometrical theory of triple junctions of CSL boundaries. *Acta Cryst. A*, 57:369–377.

Glowinski, K. (2013). On frequencies of occurrence of geometrically characteristic grain boundaries. *Sol. St. Phenom.*, 203–4:427–30.

Glowinski, K. (2014). On identification of symmetric and improperly quasi-symmetric grain boundaries. *J. Appl. Cryst.*, 47:726–31.

Glowinski, K. and Morawiec, A. (2012). A toolbox for geometric grain boundary characterization. In *1st International Conference on 3D Materials Science*, pages 119–24.

Glowinski, K. and Morawiec, A. (2014a). Analysis of experimental grain boundary distributions based on boundary-space metrics. *Metall. Mater. Trans. A*, 45:3189–94.

Glowinski, K. and Morawiec, A. (2014b). Twist, tilt, and symmetric grain boundaries in hexagonal materials. *J. Mater. Sci.*, 49:3936–42.

Glowinski, K. and Morawiec, A. (2015). Towards effective analysis of large grain boundary data sets. *IOP Conf. Ser.: Mater. Sci. Eng.*, to appear.

Goux, C. (1974). Structure des joints de grains: considérations cristallographiques et méthodes de calcul des structures. *Can. Metall. Quart.*, 13:9–31.

Grabski, M. W. (1969). *Struktura granic ziarn w metalach*. Wydawnictwo "Śląsk", Katowice (in Polish).

Graser, S., Hirschfeld, P. J., Kopp, T., Gutser, R., Andersen, B. M., and Mannhart, J. (2010). How grain boundaries limit supercurrents in high-temperature superconductors. *Nat. Phys.*, 6:609–14.

Groeber, M., Ghosh, S., Uchic, M. D., and Dimiduk, D. M. (2008a). A framework for automated analysis and simulation of 3D polycrystalline microstructures.: Part 1: Statistical characterization. *Acta Mater.*, 56:1257–73.

Groeber, M., Ghosh, S., Uchic, M. D., and Dimiduk, D. M. (2008b). A framework for automated analysis and simulation of 3D polycrystalline microstructures.: Part 2: Synthetic structure generation. *Acta Mater.*, 56:1274–87.

Groeber, M. and Jackson, M. (2014). DREAM.3D: A digital representation environment for the analysis of microstructure in 3D. *Integr. Mater. Manuf. Innov.*, 3:5.

Groeber, M. A., Haley, B. K., Uchic, M. D., Dimiduk, D. M., and Ghosh, S. (2006). 3D reconstruction and characterization of polycrystalline microstructures using a FIB-SEM system. *Mater. Charact.*, 57:259–73.

Guo, X. (1995). Physical origin of the intrinsic grain-boundary resistivity of stabilized-zirconia: Role of the space-charge layers. *Solid State Ionics*, 81:235–42.

Gurevich, A. and Pashitskii, E. A. (1998). Current transport through low-angle grain boundaries in high-temperature superconductors. *Phys. Rev. B*, 57:13878–93.

Han, W., Demkowicz, M. J., Mara, N. A., Fu, E., Sinha, S., Rollett, A. D., Wang, Y., Carpenter, J. S., Beyerlein, I. J., and Misra, A. (2013). Design of radiation tolerant materials via interface engineering. *Adv. Mater.*, 25:6975–9.

He, Y. and Jonas, J. J. (2007). Representation of orientation relationships in Rodrigues–Frank space for any two classes of lattice. *J. Appl. Cryst.*, 40:559–69.

Hefferan, C. M., Li, S. F., Lind, J., Lienert, U., Rollett, A. D., Wynblatt, P., and Suter, R. M. (2009). Statistics of high purity nickel microstructure from high energy X-ray diffraction microscopy. *CMC – Comput. Mater. Con.*, 14:209–19.

Heinz, A. and Neumann, P. (1991). Representation of orientation and disorientation data for cubic, hexagonal, tetragonal and orthorhombic crystals. *Acta Cryst. A*, 47:780–9.

Henderson, A., Ahrens, J., and Law, C. (2004). *The ParaView Guide*. Kitware Inc.

Herring, C. (1951). *The Physics of Powder Metallurgy*. MGraw-Hill.

Hilgenkamp, H. and Mannhart, J. (2002). Grain boundaries in high-T_c superconductors. *Rev. Mod. Phys.*, 74:485–549.

Hodgson, B. K. and Mykura, H. (1973). Torque terms and grain-boundary energy measurement. *J. Mater. Sci.*, 8:565–70.

Hoffman, D. W. and Cahn, J. W. (1972). A vector thermodynamics for anisotropic surfaces: I. fundamentals and application to plane surface junctions. *Surf. Sci.*, 31:368–88.

Hofmann, S. and Lejček, P. (1996). Solute segregation at grain boundaries. *Interface Sci.*, 3:241–67.

Holm, E. A., Olmsted, D. L., and Foiles, S. M. (2010). Comparing grain boundary energies in face-centered cubic metals: Al, Au, Cu and Ni. *Scripta Mater.*, 63:905–8.

Ishida, Y. and Mclean, M. (1973). Burgers vectors of boundary dislocations in ordered grain boundaries of cubic metals. *Philos. Mag.*, 27:1125–34.

Jensen, D. J. and Poulsen, H. F. (2012). The three dimensional X-ray diffraction technique. *Mater. Charact.*, 72:1–7.

Kallend, J. S., Morris, P. P., and Davies, G. J. (1976). Texture transformations – the misorientation distribution function. *Acta Metall.*, 24:361–70.

Karthikeyan, T. and Saroja, S. (2013). GBgeom: a computer program for visualizing texture parameters and simulating grain boundary structures in cubic crystals. *J. Appl. Cryst.*, 46:1221–4.

Kim, C.-S., Hu, Y., Rohrer, G. S., and Randle, V. (2005). Five-parameter grain boundary distribution in grain boundary engineered brass. *Scripta Mater.*, 52:633–7.

Kim, C.-S., Massa, T. R., and Rohrer, G. S. (2008). Interface character distributions in WC-Co composites. *J. Am. Ceram. Soc.*, 91:996–1001.

Kim, H.-K., Ko, W.-S., Lee, H.-J., Kim, S. G., and Lee, B.-J. (2011). An identification scheme of grain boundaries and construction of a grain boundary energy database. *Scripta Mater.*, 64:1152–5.

King, A., Reischig, P., Adrien, J., and Ludwig, W. (2013). First laboratory X-ray diffraction contrast tomography for grain mapping of polycrystals. *J. Appl. Cryst.*, 46:1734–40.

Kobayashi, S., Maruyama, T., Saito, S., Tsurekawa, S., and Watanabe, T. (2014). In situ observations of crack propagation and role of grain boundary microstructure in nickel embrittled by sulfur. *J. Mater. Sci.*, 49:4007–17.

Kobayashi, S., Tsurekawa, S., Watanabe, T., and Palumbo, G. (2010). Grain boundary engineering for control of sulfur segregation-induced embrittlement in ultrafine-grained nickel. *Scripta Mater.*, 62:294–7.

Kokawa, H. (2005). Weld decay-resistant austenitic stainless steel by grain boundary engineering. *J. Mater. Sci.*, 40:927–932.

Kokawa, H., Shimada, M., Michiuchi, M., Wang, Z., and Sato, Y. (2007). Arrest of weld-decay in 304 austenitic stainless steel by twin-induced grain boundary engineering. *Acta Mater.*, 55:5401–7.

Krakauer, B. W. and Seidman, D. N. (1998). Subnanometer scale study of segregation at grain boundaries in an Fe(Si) alloy. *Acta Mater.*, 46:6145–61.

Kronberg, M. L. and Wilson, F. H. (1947). Secondary recrystallization in copper. *Trans. Met. Soc. AIME*, 185:501–14.

Krupp, U., Wagenhuber, P. E.-G., Kane, W. M., and McMahon, C. J. (2005). Improving resistance to dynamic embrittlement and intergranular oxidation of nickel based superalloys by grain boundary engineering type processing. *Mater. Sci. Tech.*, 21:1247–54.

Kumar, M., King, W. E., and Schwartz, A. J. (2000). Modifications to the microstructural topology in f.c.c. materials through thermomechanical processing. *Acta Mater.*, 48:2081–91.

Lamzatouar, A., Palais, O., Duparc, O. B. M. H., Thibault, J., and Charai, A. (2005). Relationship between structure, segregation and electrical activity in grain boundaries. *J. Mater. Sci.*, 40:3163–7.

Lange, F. F. (1967). Mathematical characterization of a general bicrystal. *Acta Metall.*, 15:311–18.

Laval, J. Y., Drouet, M., Swiatnicki, W., and Cabanel, C. (1994). Weak attenuation of the supercurrent by high angle boundaries in $YBa_2Cu_3O_{7-x}$ ceramics. *Physica C*, 235–40:2987–8.

Lee, S.-B., Rohrer, G. S., and Rollett, A. D. (2014). Three-dimensional digital approximations of grain boundary networks in polycrystals. *Model. Simul. Mater. Sc.*, 22:025017.

Lehockey, E. M., Limoges, D., Palumbo, G., Sklarchuk, J., Tomantschger, K., and Vincze, A. (1999). On improving the corrosion and growth resistance of positive Pb-acid battery grids by grain boundary engineering. *J. Power Sources*, 78:79–83.

Lehockey, E. M. and Palumbo, G. (1997). On the creep behaviour of grain boundary engineered nickel 1. *Mater. Sci. Eng. A*, 237:168–72.

Lehockey, E. M., Palumbo, G., Brennenstuhl, A., and Lin, P. (1998a). Mitigating intergranular attack and growth in lead-acid battery electrodes for extended cycle and operating life. *Metall. Mater. Trans. A*, 29:387–96.

Lehockey, E. M., Palumbo, G., and Lin, P. (1998b). Improving the weldability and service performance of nickel-and iron-based superalloys by grain boundary engineering. *Metall. Mater. Trans. A*, 29:3069–79.

Lejček, P., Paidar, V., Adámek, J., and Hofmann, S. (1997). Segregation and corrosion behaviour of incommensurate 45°[100] grain boundaries in an Fe-Si alloy: The role of grain boundary plane orientation. *Acta Mater.*, 45:3915–26.

Li, J., Dillon, S. J., and Rohrer, G. S. (2009). Relative grain boundary area and energy distributions in nickel. *Acta Mater.*, 57:4304–11.

Lienert, U., Li, S. F., Hefferan, C. M., Lind, J., Suter, R. M., Bernier, J. V., Barton, N. R.,

Brandes, M. C., Mills, M. J., Miller, M. P., Jakobsen, B., and Pantleon, W. (2011). High-energy diffraction microscopy at the Advanced Photon Source. *JOM*, 63:70–7.

Lin, P., Palumbo, G., Erb, U., and Aust, K. T. (1995). Influence of grain boundary character distribution on sensitization and intergranular corrosion of alloy 600. *Scripta Metall. Mater.*, 33:1387–92.

Liu, H. H., Schmidt, S., Poulsen, H. F., Godfrey, A., Liu, Z. Q., Sharon, J. A., and Huang, X. (2011). Three-dimensional orientation mapping in the transmission electron microscope. *Science*, 332:833–4.

Luo, Y.-K. and Qin, R.-S. (2015). Computation of five-dimensional grain boundary energy. *Acta Metall. Sin.*, pages 1–7.

Mackenzie, J. K. (1958). Second paper on statistics associated with the random disorientation of cubes. *Biometrika*, 45:229–40.

McLean, M. (1973). Grain-boundary energy of copper at 1030°C. *J. Mater. Sci.*, 8:571–6.

Moore, R. H., Rohrer, G. S., and Saigal, S. (2009). Reconstruction and simplification of high-quality multiple-region models from planar sections. *Eng. Comput.*, 25:221–35.

Morawiec, A. (1997). Distributions of misorientation angles and misorientation axes for crystallites with different symmetries. *Acta Cryst. A*, 53:273–85.

Morawiec, A. (1998). Symmetries of grain boundary distributions. In Weiland, H., Adams, B. L., and Rollett, A. D., editors, *Proc. of the Third Int. Conf. on Grain Growth*, pages 509–14.

Morawiec, A. (2000). Method to calculate the grain boundary energy distribution over the space of macroscopic boundary parameters from the geometry of triple junctions. *Acta Mater.*, 48:3525–32.

Morawiec, A. (2004). *Orientations and Rotations*. Springer.

Morawiec, A. (2009a). Models of uniformity for grain boundary distributions. *J. Appl. Cryst.*, 42:783–92.

Morawiec, A. (2009b). On the frequency of occurrence of tilt and twist grain boundaries. *Scripta Mater.*, 61:438–40.

Morawiec, A. (2010). Frequencies of tilt and twist boundaries among random grain boundaries. *Sol. St. Phenom.*, 160:95–9.

Morawiec, A. (2011). Low-Σ twist and tilt grain boundaries in cubic materials. *J. Appl. Cryst.*, 44:1152–6.

Morawiec, A. (2012a). On 'interface-plane scheme' and symmetric grain boundaries. *Z. Kristallogr.*, 227:199–206.

Morawiec, A. (2012b). Statistical analysis of grain boundaries in the space of macroscopic boundary parameters. *Mater. Sci. Forum*, 702–3:697–702.

Morawiec, A. and Field, D. P. (1996). Rodrigues parameterization for orientation and misorientation distributions. *Philos. Mag. A*, 73:1113–30.

Morawiec, A. and Glowinski, K. (2013). On "macroscopic" characterization of mixed grain boundaries. *Acta Mater.*, 61:5756–67.

Mori, T., Miura, H., Tokita, T., Haji, J., and Kato, M. (1988). Determination of the energies

of [001] twist boundaries in Cu with the shape of boundary SiO2 particles. *Phil. Mag. Lett.*, 58:11–15.

Ogawa, H. (2006). GBstudio: A builder software on periodic models of CSL boundaries for molecular simulation. *Mater. Trans.*, 47:2706–10.

Olmsted, D. L. (2009). A new class of metrics for the macroscopic crystallographic space of grain boundaries. *Acta Mater.*, 57:2793–9.

Olmsted, D. L., Foiles, S. M., and Holm, E. A. (2009). Survey of computed grain boundary properties in face-centered cubic metals: I. grain boundary energy. *Acta Mater.*, 57:3694–703.

Otsuki, A. (1996). Variation of energies of aluminum [001] boundaries with misorientation and inclination. *Mat. Sci. Forum.*, 207–9:413–6.

Palumbo, G. and Aust, K. T. (1990). Structure-dependence of intergranular corrosion in high purity nickel. *Acta Metall. Mater.*, 38:2343–52.

Palumbo, G. and Aust, K. T. (1995). Solute effects in grain boundary engineering. *Can. Metall. Quart.*, 34:165–73.

Palumbo, G., Aust, K. T., Lehockey, E. M., Erb, U., and Lin, P. (1998). On a more restrictive geometric criterion for "special" CSL grain boundaries. *Scripta Mater.*, 38:1685–90.

Patala, S. and Schuh, C. A. (2013). Symmetries in the representation of grain boundary-plane distributions. *Philos. Mag.*, 93:524–73.

Peterson, N. L. (1983). Grain-boundary diffusion in metals. *Int. Mater. Rev.*, 28:65–91.

Pospiech, J., Sztwiertnia, K., and Haessner, F. (1986). The misorientation distribution function. *Texture Microstruct.*, 6:201–15.

Poulsen, H. F. (2012). An introduction to three-dimensional X-ray diffraction microscopy. *J. Appl. Cryst.*, 45:1084–97.

Pumphrey, P. H. (1972). A plane matching theory of high angle grain boundary structure. *Scripta Metall.*, 6:107–14.

Rabkin, E. (2005). Effect of grain boundary faceting on kinetics of grain growth and microstructure evolution. *J. Mater. Sci.*, 40:875–9.

Randle, V. (1993). *The measurement of grain boundary geometry.* IOP Publishing.

Randle, V., Rohrer, G. S., Miller, H. M., Coleman, M., and Owen, G. T. (2008). Five-parameter grain boundary distribution of commercially grain boundary engineered nickel and copper. *Acta Mater.*, 56:2363–73.

Ratanaphan, S., Olmsted, D. L., Bulatov, V. V., Holm, E. A., Rollett, A. D., and Rohrer, G. S. (2015). Grain boundary energies in body-centered cubic metals. *Acta Mater.*, 88:346–54.

Ratanaphan, S., Yoon, Y., and Rohrer, G. S. (2014). The five parameter grain boundary character distribution of polycrystalline silicon. *J. Mater. Sci.*, 49:4938–45.

Read, W. T. and Shockley, W. (1950). Dislocation models of crystal grain boundaries. *Phys. Rev.*, 78:275–89.

Rohrer, G. S. (2011a). Grain boundary energy anisotropy: a review. *J. Mater. Sci.*, 46:5881–95.

Rohrer, G. S. (2011b). Measuring and interpreting the structure of grain-boundary networks. *J. Am. Ceram. Soc.*, 94:633–46.

Rohrer, G. S., Li, J., Lee, S., Rollett, A. D., Groeber, M., and Uchic, M. D. (2010). Deriving grain boundary character distributions and relative grain boundary energies from three-dimensional ebsd data. *Mater. Sci. Tech.*, 26:661–9.

Rohrer, G. S., Randle, V., Kim, C.-S., and Hu, Y. (2006). Changes in the five-parameter grain boundary character distribution in α-brass brought about by iterative thermomechanical processing. *Acta Mater.*, 54:4489–502.

Rowenhorst, D. J. and Voorhees, P. W. (2005). Measurements of the grain boundary energy and anisotropy in tin. *Metall. Mater. Trans. A*, 36:2127–35.

Saylor, D. M., Morawiec, A., and Rohrer, G. S. (2003a). Distribution of grain boundaries in magnesia as a function of five macroscopic parameters. *Acta Mater.*, 51:3663–74.

Saylor, D. M., Morawiec, A., and Rohrer, G. S. (2003b). The relative free energies of grain boundaries in magnesia as a function of five macroscopic parameters. *Acta Mater.*, 51:3675–86.

Schwartz, A. J. (1998). The potential engineering of grain boundaries through thermomechanical processing. *JOM*, 50:50–5.

Schwartz, A. J., Kumar, M., Adams, B. L., and Field, D., editors (2009). *Electron Backscatter Diffraction in Materials Science*. Springer, 2$^{\text{nd}}$ edition.

Seidman, D. (1992). *Materials interfaces: atomic-level structure and properties*, chapter 2. Chapman & Hall, London.

Shvindlerman, L. S. and Gottstein, G. (2005). Cornerstones of grain structure evolution and stability: Vacancies, boundaries, triple junctions. *J. Mater. Sci.*, 40:819–39.

Smith, C. S. (1948). Grains, phases, and interfaces: An interpretation of microstructure. *Trans. Met. Soc. AIME*, 175:15–51.

Sutton, A. P. (1991). An analytic model for grain-boundary expansions and cleavage energies. *Philos. Mag. A*, 63:793–818.

Sutton, A. P. and Balluffi, R. W. (1987). On geometric criteria for low interfacial energy. *Acta Metall.*, 35:2177–201.

Sutton, A. P. and Balluffi, R. W. (2007). *Interfaces in Crystalline Materials*. Oxford University Press.

Swiatnicki, W., Lartigue-Korinek, S., and Laval, J. Y. (1995). Grain boundary structure and intergranular segregation in Al_2O_3. *Acta Metall. Mater.*, 43:795–805.

Swiatnicki, W. A., Łojkowski, W., and Grabski, M. W. (1986). Investigation of grain boundary diffusion in polycrystals by means of extrinsic grain boundary dislocations spreading rate. *Acta Metall.*, 34:599–605.

Thaveeprungsriporn, V. and Was, G. S. (1997). The role of coincidence-site-lattice boundaries in creep of Ni-16Cr-9Fe at 360° C. *Metall. Mater. Trans. A*, 28:2101–12.

Tsurekawa, S., Okamoto, K., Kawahara, K., and Watanabe, T. (2005). The control of grain boundary segregation and segregation-induced brittleness in iron by the application of a magnetic field. *J. Mater. Sci.*, 40:895–901.

Uchic, M., Groeber, M., Callahan, P., Shah, M., and Shiveley, A. (2012a). Development

and application of a novel characterization system to quantify grain structures of nickel superalloys in 3D. *Microsc. Microanal.*, 18:518–9.

Uchic, M., Groeber, M., Shah, M., Callahan, P., Shiveley, A., Scott, M., Chapman, M., and Spowart, J. (2012b). *An Automated Multi-Modal Serial Sectioning System for Characterization of Grain-Scale Microstructures in Engineering Materials*, pages 195–202. John Wiley & Sons.

Udler, D. and Seidman, D. N. (1996). Grain boundary and surface energies of fcc metals. *Phys. Rev. B*, 54:R11133–6.

van den Boogaart, K. G. (2002). *Statistics for individual crystallographic orientation measurements*. PhD thesis, Aachen.

Wang, Z.-J., Tsurekawa, S., Ikeda, K., Sekiguchi, T., and Watanabe, T. (1999). Relationship between electrical activity and grain boundary structural configuration in polycrystalline silicon. *Interface Sci.*, 7:197–205.

Watanabe, T. (1984). An approach to grain boundary design for strong and ductile polycrystals. *Res Mech.*, 11:47–84.

Watanabe, T. (2011). Grain boundary engineering: historical perspective and future prospects. *J. Mater. Sci.*, 46:4095–115.

Watanabe, T., Suzuki, Y., Tanii, S., and Oikawa, H. (1990). The effects of magnetic annealing on recrystallization and grain-boundary character distribution (GBCD) in iron-cobalt alloy polycrystals. *Phil. Mag. Lett.*, 62:9–17.

Watanabe, T. and Tsurekawa, S. (1999). The control of brittleness and development of desirable mechanical properties in polycrystalline systems by grain boundary engineering. *Acta Mater.*, 47:4171–85.

Watanabe, T. and Tsurekawa, S. (2004). Toughening of brittle materials by grain boundary engineering. *Mater. Sci. Eng. A*, 387–9:447–55.

Watanabe, T., Tsurekawa, S., Zhao, X., Zuo, L., and Esling, C. (2006). A new challenge: grain boundary engineering for advanced materials by magnetic field application. *J. Mater. Sci.*, 41:7747–59.

Winning, M. and Raabe, D. (2008). Influence of low angle grain boundaries on recrystallization. In *Applications of Texture Analysis*, pages 577–84. John Wiley & Sons, Inc.

Wolf, D. (1989). A Read-Shockley model for high-angle grain boundaries. *Scripta Metall.*, 23:1713–8.

Wolf, D. (1990a). A broken-bond model for grain boundaries in face centered cubic metals. *J. Appl. Phys.*, 68:3221–36.

Wolf, D. (1990b). Structure-energy correlation for grain boundaries in f.c.c. metals – iv. asymmetrical twist (general) boundaries. *Acta Metall. Mater.*, 38:791–8.

Wolf, D. and Lutsko, J. F. (1989). On the geometrical relationship between tilt and twist grain boundaries. *Z. Kristallogr.*, 189:239–62.

Wolf, D. and Yip, S. (1993). *Materials Interfaces: Atomic-level Structure and Properties*. Springer.

Wynblatt, P. and Takashima, M. (2001). Correlation of grain boundary character with wetting behavior. *Interface Sci.*, 9:265–73.

Wyrzykowski, J. W. and Grabski, M. W. (1986). The Hall-Petch relation in aluminium and its dependence on the grain boundary structure. *Philos. Mag. A*, 53:505–20.

Yamamoto, T., Sato, Y., Tanaka, T., Hayashi, K., Ikuhara, Y., and Sakuma, T. (2005). Electron transport behaviors across single grain boundaries in n-type $BaTiO_3$, $SrTiO_3$ and ZnO. *J. Mater. Sci.*, 40:881–7.

Zaefferer, S., Wright, S. I., and Raabe, D. (2008). Three-dimensional orientation microscopy in a focused ion beam–scanning electron microscope: A new dimension of microstructure characterization. *Metall. Mater. Trans. A*, 39:374–89.

Zhang, Y., Vincent, G., Dewobroto, N., Germain, L., Zhao, X., Zuo, L., and Esling, C. (2005). The effects of thermal processing in a magnetic field on grain boundary characters of ferrite in a medium carbon steel. *J. Mater. Sci.*, 40:903–8.

Zhao, J. and Adams, B. L. (1988). Definition of an asymmetric domain for intercrystalline misorientation in cubic materials in the space of Euler angles. *Acta Cryst. A*, 44:326–36.